



HAL
open science

Millimeter wave multi-RAT small cells for heterogeneous mobile services : performance analysis and optimization

Gourab Ghatak

► To cite this version:

Gourab Ghatak. Millimeter wave multi-RAT small cells for heterogeneous mobile services : performance analysis and optimization. Networking and Internet Architecture [cs.NI]. Université Paris Saclay (COmUE), 2019. English. NNT : 2019SACLT010 . tel-02266363

HAL Id: tel-02266363

<https://pastel.hal.science/tel-02266363>

Submitted on 14 Aug 2019

HAL is a multi-disciplinary open access archive for the deposit and dissemination of scientific research documents, whether they are published or not. The documents may come from teaching and research institutions in France or abroad, or from public or private research centers.

L'archive ouverte pluridisciplinaire **HAL**, est destinée au dépôt et à la diffusion de documents scientifiques de niveau recherche, publiés ou non, émanant des établissements d'enseignement et de recherche français ou étrangers, des laboratoires publics ou privés.

Millimeter Wave Multi-RAT Small Cells for Heterogeneous Mobile Services: Performance Analysis and Optimization

Thèse de doctorat de l'Université Paris-Saclay
préparée à CEA-LETI, Grenoble

École doctorale n°580 sciences et technologies de l'information et de
la communication (STIC)

Thèse présentée et soutenue à Grenoble, le 24/01/2019, par

Gourab Ghatak

Composition du Jury :

M. Jean-Marie GORCE Professeur, INSA Lyon	Président
M. Chandra MURTHY Professeur, Indian Institute of Science Bangalore	Rapporteur
M. Francois BACCELLI Professeur, The University of Texas at Austin	Rapporteur
M. Marco DI RENZO Professeur, Paris-Saclay University	Examineur
Mme Mylene PISCHELLA Maître de Conférences, Conservatoire National des Arts et Métiers	Examineur
M. Marceau COUPECHOUX Professeur, Telecom ParisTech	Directeur de thèse
M. Antonio DE DOMENICO Ingénieur de Recherche, CEA Grenoble	Co-Directeur de thèse

Titre : Millimeter Wave Multi-RAT Small Cells pour services mobiles hétérogènes: analyse et optimisation des performances.

Mots clés : Communications par ondes millimétriques, géométrie stochastique, localisation

Résumé : Les futures applications sans fil anticipent une explosion de la pléthore de cas d'utilisation et de services, qui ne peut être soutenue par des améliorations incrémentielles des schémas de communication existants. Pour cela, deux axes de recherche sont particulièrement intéressants: la densification du réseau à l'aide de petites cellules et la communication par ondes millimétriques (ondes millimétriques). Dans cette thèse, nous modélisons et évaluons des réseaux cellulaires constitués de petites cellules à ondes millimétriques utilisant la technique d'accès multi-radio (RAT) déployées au-dessus de la macro-architecture existante. Premièrement, nous modélisons mathématiquement un déploiement homogène de petites cellules multi-RAT et caractérisons les performances de l'utilisateur et du réseau en termes de probabilité de couverture signal sur brouillage plus rapport de bruit (SINR), de débit descendant et de probabilité de surcharge de cellule. Ensuite, nous étudions l'association des utilisateurs à différents niveaux et la sélection optimale de différents RAT, de manière à optimiser ces mesures de performance. En règle générale, les modèles de réseau cellulaire qui supposent des déploiements homogènes de petites cellules ne tiennent pas compte des nuances des caractéristiques de blocage urbain.

Pour résoudre ce problème, nous modélisons les emplacements de petites cellules le long des routes d'une ville, puis nous prenons en compte les blocages de signaux dus à la construction d'immeubles ou au déplacement de véhicules sur les routes. Sur ce réseau, nous supposons que l'opérateur prend en charge trois types de services v.i.z., les communications ultra-fiables à faible temps de latence (URLLC), les communications massives de type machine (mMTC) et le haut débit mobile amélioré (eMBB) avec des besoins différents. En conséquence, nous étudions la sélection optimale de RAT pour ces services avec divers blocages de véhicules.

Enfin, sur la base du modèle de déploiement sur route de petites cellules à ondes millimétriques, nous étudions un réseau conçu pour prendre en charge simultanément des services de positionnement et de données. Nous caractérisons la précision du positionnement en fonction des limites de la localisation, puis étudions des stratégies optimales de partitionnement des ressources et de sélection de la largeur de faisceau afin de répondre à diverses exigences de positionnement et de débit de données.

Title : Millimeter Wave Multi-RAT Small Cells for Heterogeneous Mobile Services: Performance Analysis and Optimization

Keywords : Millimeter wave communications, stochastic geometry, localization

Abstract : Future wireless applications anticipate an explosion in the plethora of use-cases and services, which cannot be sustained by incremental improvements on the existing

To address this, we model the small cell locations along the roads of a city, and subsequently, we take into consideration the signal blockages due to buildings or moving



communication schemes. For this, two research directions are particularly attractive: network densification using small cells and millimeter wave (mm-wave) wave communications. In this thesis, we model and evaluate cellular networks consisting of multi-radio access technique (RAT) mm-wave small cells deployed on top of the legacy macro-architecture. First, we mathematically model a homogeneous deployment of multi-RAT small cells and characterize the user and network performance in terms of signal to interference plus noise ratio (SINR) coverage probability, downlink throughput, and the cell overloading probability. Then, we study users association to different tiers and optimal selection of different RATs, so as to optimize these performance metrics. Generally, cellular network models that assume homogeneous deployments of small cells fail to take into account the nuances of urban blockage characteristics.

vehicles on the roads. In this network, we assume that the operator supports three types of services v.i.z., ultra-reliable low-latency communications (URLLC), massive machine-type communications (mMTC), and enhanced mobile broadband (eMBB) with different requirements. Consequently, we study the optimal RAT selection for these services with varying vehicular blockages.

Finally, based on the on-road deployment model of mm-wave small cells, we study a network designed to support positioning and data services simultaneously. We characterize the positioning accuracy based on the localization bounds and then study optimal resource partitioning and beamwidth selection strategies to address varied positioning and data-rate requirements.





TELECOM PARISTECH
UNIVERSITÉ PARIS SACLAY
DOCTORAL THESIS

**Millimeter Wave Multi-RAT
Small Cells for Heterogeneous
Mobile Services: Performance
Analysis and Optimization**

Author:

Gourab GHATAK

Supervisor:

Dr. Antonio De Domenico

Thesis Director:

Dr. Marceau COUPECHOUX

Abstract

Future wireless applications anticipate an explosion in the plethora of use-cases and services, which cannot be sustained by incremental improvements on the existing communication schemes. For this, two research directions are particularly attractive: network densification using small cells and millimeter wave (mm-wave) wave communications. In this thesis, we model and evaluate cellular networks consisting of multi-radio access technique (RAT) mm-wave small cells deployed on top of the legacy macro-architecture. First, we mathematically model a homogeneous deployment of multi-RAT small cells and characterize the user and network performance in terms of signal to interference plus noise ratio (SINR) coverage probability, downlink throughput, and the cell overloading probability. Then, we study users association to different tiers and optimal selection of different RATs, so as to optimize these performance metrics.

Generally, cellular network models that assume homogeneous deployments of small cells fail to take into account the nuances of urban blockage characteristics. To address this, we model the small cell locations along the roads of a city, and subsequently, we take into consideration the signal blockages due to buildings or moving vehicles on the roads. In this network, we assume that the operator supports three types of services v.i.z., ultra-reliable low-latency communications (URLLC), massive machine-type communications (mMTC), and enhanced mobile broadband (eMBB) with different requirements. Consequently, we study the optimal RAT selection for these services with varying vehicular blockages.

Finally, based on the on-road deployment model of mm-wave small cells, we study a network designed to support positioning and data services simultaneously. We characterize the positioning accuracy based on the localization bounds and then study optimal resource partitioning and beamwidth selection strategies to address varied positioning and data-rate requirements.

Contents

Abstract	iii
1 Introduction	1
1.1 Future of Mobile Networks and fifth generation (5G)	1
1.1.1 Key Requirements of 5G	2
Data Rate	2
Latency	2
Reliability	3
Massive Connectivity	3
Energy Efficiency	3
Flexible and Low-Cost Network Management	3
1.1.2 Key Technologies for 5G	4
1.2 Mm-Wave and Multi-RAT Challenges	5
1.2.1 Mm-wave Communications	5
1.2.2 Multi RAT Association	7
1.3 Stochastic Geometry Based Modeling	8
1.3.1 Key Notions of Stochastic Geometry	9
1.3.2 SINR Coverage in Single-Tier Networks	10
1.4 Bound-Based Characterization of mm-wave Positioning	13
1.5 Contributions and Organization	16
I Modeling and Performance Analysis of Multi-Tier Networks with mm-Wave Multi-RAT Small Cells	23
2 Coverage Analysis and Load Balancing	25
2.1 Introduction	25
2.1.1 Related Work	26
2.1.2 Contributions and Organization	27
2.2 System Model	29
2.2.1 Two-Tier Network Model	29

2.2.2	Blockage Processes	30
2.2.3	Directional Beamforming in mm-wave	30
2.2.4	Path-loss Processes	31
2.2.5	Dynamic Traffic Model	31
2.3	Cell Association Procedure	32
2.3.1	Distribution of the Path-loss Process	32
2.3.2	Tier and RAT Selection Scheme	33
2.3.3	Tier Selection	33
2.3.4	RAT Selection in small cell base station (SBS)	35
2.3.5	Comparison to a One-Step Association Strategy	36
2.3.6	A Simple Strategy to Prioritize mm-wave RAT	37
2.4	Downlink SINR Distribution	38
2.4.1	SINR Coverage Probability	39
2.4.2	A Near-Optimal Strategy for Bias Selection	40
2.5	Cell Load, User Throughput, and Load Balancing	41
2.5.1	Cell Load Characterization	41
2.5.2	Average User Throughput	43
2.5.3	Delay-Throughput Trade-off of the One-Step Association Scheme.	44
2.6	Simulation Results	44
2.6.1	Validation of the Path-loss Exponent Approximation	44
2.6.2	Trends in Cell Association Probabilities	45
2.6.3	Comparison with the One-Step Association Strategy:	47
2.6.4	Trends in SINR Coverage Probabilities	48
2.6.5	Performance of the Near-Optimal Strategy to Select Tier and RAT Biases	50
2.6.6	Analysis of the Bound on Overloading Probabilities	53
2.6.7	Rate Optimal Choice of Tier and RAT Selection Biases	53
2.7	Chapter Conclusion	56
3	Slice-Aware RAT Selection	59
3.1	Introduction	59
3.1.1	Related Work	60
3.1.2	Contributions and Organization	61
3.2	Preliminary Results on Poisson line Cox process (PLCP)	63
3.2.1	PLCP Definition	63
3.2.2	Palm Perspective of the PLCP	64

3.2.3	Probability Generating Functionals of the PLCP	64
3.3	System Model	65
3.3.1	Network Geometry	66
3.3.2	Static Urban Blockage	66
3.3.3	Blockage due to Moving Vehicles	67
3.3.4	Path Gain	68
3.3.5	Tier and RAT Selection Procedure	68
3.4	Vehicular Blockage and mm-wave Interference	69
3.4.1	Characterization of the Vehicular Blockage Probability	69
3.4.2	Interference Characterization in mm-wave	70
3.5	Association Probabilities	72
3.5.1	Tier Selection for a user equipment (UE)	72
3.5.2	RAT Selection for Pedestrian UE	74
3.6	SINR Coverage Probabilities	75
3.7	A Slice-Aware RAT Selection Mechanism	76
3.7.1	Effect of RAT Selection Bias on Blockage, SINR, and Rate	76
Effect of Bias on Blockage	76	
Effect of Bias on SINR and Data Rate	77	
3.7.2	Protocol for Slice-Aware RAT Selection	77
3.8	Numerical Results	78
3.8.1	Validation of the mm-Wave Interference and SINR Model	78
3.8.2	Association and RAT Selection Probabilities	79
3.8.3	SINR Coverage Probabilities	81
3.8.4	Slice-Aware RAT Selection	82
SINR Coverage	84	
Vehicular Blockage	85	
Rate Coverage	85	
Slice-Aware RAT Selection	85	
3.8.5	System Design Insights	86
3.9	Chapter Conclusions	87

II Joint Communication and Localization Service in mm-Wave Networks **89**

4	Positioning Data-Rate Trade-off	91
4.1	Introduction	91

4.1.1	Related Work	92
4.1.2	Contributions and Organization	93
4.2	System Model	93
4.2.1	Network Geometry	94
4.2.2	Path-loss	94
4.2.3	Transmission Policy	94
4.3	Positioning Error, Data Rate Coverage and beam-selection error	95
4.3.1	Distance Estimation Analysis	95
4.3.2	Coverage and Rate Analysis	97
4.3.3	Beam Selection Error	98
4.4	Numerical Results and Discussion	99
4.4.1	SINR Coverage Probability	99
4.4.2	Beam-Selection Error	99
4.4.3	Distance Estimation-Data Rate Trade-off	101
4.4.4	Quality of service (QoS) Aware Network Parameter Setting	101
4.5	Chapter Conclusion	103
5	Throughput Characterization and Beamwidth Selection	105
5.1	Introduction	105
5.2	System Model	106
5.2.1	Network Geometry and base stations (BS) Characteristics	106
5.2.2	Path-loss	107
5.2.3	Received signal model	108
5.2.4	Transmission Policy	108
5.3	Localization Phase	108
5.4	Beam-Selection Error	109
5.5	Data Service Phase	111
5.5.1	Characterization of the Rate Coverage Probability	111
5.5.2	Effective Rate Coverage Probability	113
5.6	Optimal Selection of Beam-Dictionary	113
5.7	Numerical Results and Discussions	113
5.8	Chapter Conclusions	117
6	Conclusions and Future Perspectives	119
6.1	Main Conclusions	119
6.2	Future Work	121
6.2.1	Realistic Characterization of Performance metrics	121

6.2.2	Reliable mm-wave Communications	122
6.2.3	Multi Agent and Cooperative localization in 5G	122
6.2.4	Network Slicing and Orchestration	122
A	Proofs of Chapter 2	125
A.1	Tier Selection Probability	125
A.2	RAT Selection Probability	126
A.3	Proof of Eq. (2.15)	126
A.4	Proof of Proposition 1	128
A.5	Probability of Sub-Optimal Association	128
B	Proofs of Chapter 4	131
B.1	Proof of Lemma 13	131
B.2	Proof of Lemma 14	132
B.3	Proof of Proposition 3	132
B.4	Proof of Lemma 16	133
B.5	Proof of Lemma 17	134
B.6	Proof of Proposition 4	135
B.7	Proof of Proposition 5	135
B.8	Proof of Theorem 1	136
C	Proofs of Chapter 6	137
C.1	Proof of Theorem 2	137
C.2	Proof of Theorem 3	138
D	Accurate Characterization of Dynamic Cell Load	141
D.1	Introduction	141
D.2	System Model	143
D.3	Characterization of the Network Load	144
D.3.1	Static vs Dynamic Load	144
D.3.2	Preliminaries	144
	Average Load of the Typical Cell	145
	Mean Cell Approximation	146
D.3.3	Distribution of the Area of the Typical Cell	146
D.3.4	Distribution of the Load of the Typical Cell	147
D.3.5	Proposed Approximations for the Average Load of the Typical Cell	149
	Exponential Integral (EI) based Approximation	149

Closed-form (CF) Approximation	150
D.4 Simulation Results	151
D.4.1 Cumulative density function (CDF) of the Load and Sta- ble Fraction of the Network	151
D.4.2 Accuracy of the EI Approximation of the Network Load	151
D.4.3 Advantages of the CF Approximation of the Network Load	152
D.5 Appendix Conclusion	153
Bibliography	155

List of Figures

1.1	An illustration of 5G cellular architecture consisting of mm-wave multi-RAT small cells.	8
1.2	SINR coverage probability vs SINR threshold with respect to different transmit powers.	13
1.3	The Bayesian CRLB (BCRLB) with varying deployment densities for two values of transmit power.	16
2.1	Validation of the approximated path-loss exponents with 3GPP parameters.	45
2.2	Tier selection probability	45
2.3	Conditional mm-wave RAT selection probability with 3GPP parameters.	46
2.4	Probability of sub-optimal association for different Q_R and for different $\frac{\lambda_S}{\lambda_M}$. The black curves correspond to $G_0 = 30$ dB and the red curves correspond to $G_0 = 36$ dB;	46
2.5	Delay-throughput trade-off with mm-wave initial access; $G_0 = 36$ dB, $Q_T = 10$ dB, $Q_R = 5$ dB, $\lambda = 100$ [user \cdot km $^{-2}$ s $^{-1}$].	47
2.6	SINR coverage probability vs tier selection bias at a threshold of $\gamma = -10$ dB for $Q_R = -\infty$ dB;	48
2.7	SINR coverage probability vs tier selection bias at a threshold of $\gamma = -10$ dB for $Q_R = \infty$, $d_M = 200$ m, $d_S = 20$ m.	49
2.8	SINR coverage probability with different line of sight (LOS) radii for $Q_R = \infty$, $\lambda_S/\lambda_M = 200$	49
2.9	SINR coverage probability vs RAT selection bias with $Q_T = 0$ dB.	50
2.10	SINR coverage probability as a function of Q_T and Q_R at a threshold of $\gamma = -10$ dB for $d_M = 200$ m, $d_S = 20$ m for $\lambda_S/\lambda_M = 50$	50
2.11	SINR coverage probability as a function of Q_T and Q_R at a threshold of $\gamma = -10$ dB for $d_M = 200$ m, $d_S = 20$ m for $\lambda_S/\lambda_M = 200$	51

2.12	Convergence of gradient descent algorithm for $\lambda_S/\lambda_M = 100$, $d_S = 10$ m and $d_M = 100$ m	51
2.13	Comparison of RAT selection strategies	52
2.14	Tightness of the bound on probability of overloading.	52
2.15	Minimum required deployment density for a given traffic density	53
2.16	Throughput optimal macro base station (MBS) association probabilities.	54
2.17	Optimal downlink user throughput	55
2.18	Optimal association probabilities for different outage probability constraints.	55
2.19	Effective user throughput vs Q_T and Q_R at a traffic density of 100 bits·s ⁻¹ m ⁻² , tolerable outage probability of 0.10, $d_M = 200$ m, $d_S = 20$ m for $\lambda_S/\lambda_M = 50$	55
2.20	Effective user throughput vs Q_T and Q_R at a traffic density of 100 bits·s ⁻¹ m ⁻² , tolerable outage probability of 0.10, $d_M = 200$ m, $d_S = 20$ m for $\lambda_S/\lambda_M = 200$	56
3.1	System model showing on-road deployment of SBSs with pedestrian UEs.	66
3.2	Model for calculating the blockage due to moving vehicles.	69
3.3	(a) Interference to the n-th SBS from the typical SBS, and (b) Simplified interference model for LOS mm-wave SBS.	71
3.4	Validation of the model for users' SINR coverage probability with $\lambda_S = 100$ km ⁻¹	79
3.5	(a) Validation of the model for users' SINR coverage probability with $\lambda_S = 100$ km ⁻¹ , (b) Validation of the dominant interference model, $G_0 = 35$ dBi, $\lambda_S = 100$ km ⁻¹ and (c) Association probabilities of the users with varying SBS density (solid lines correspond to $\lambda_R = 15$ km ⁻¹ , dashed lines correspond to $\lambda_R = 5$ km ⁻¹).	80
3.6	(a) Conditional mm-wave selection probability with RAT selection bias, (b) Comparison of different schemes of RAT selection, $G_0 = 20$ dBi and $\lambda_S = 10$ km ⁻¹	81
3.7	(a) SINR coverage probability of the users for different SBS deployment densities and road densities, (b) SINR coverage probability for the users at $\gamma = -10$ dB with respect to the SBS deployment density ($G_0 = 10$ dBi, $Q_R = 0$ dB).	82

3.8	SINR coverage probabilities for the users with varying RAT selection bias with $G_0 = 10$ dBi for different vehicular blockage densities, (a) $\lambda_S = 50 \text{ km}^{-1}$ and (b) $\lambda_S = 10 \text{ km}^{-1}$. (c) Vehicular blockage probability with respect to RAT selection bias given that the user is served with mm-wave RAT.	83
3.9	(a) Rate coverage probability for the user for different vehicular blockage densities, $\lambda_S = 10 \text{ km}^{-1}$ and (b) Slice-aware RAT selection probabilities for different use-cases, solid lines denote the sub-6GHz association probabilities and the dotted lines denote the mm-wave association probabilities respectively.	84
4.1	Illustration of the beam-selection error.	98
4.2	SNR coverage probabilities for a threshold of $\gamma = -10$ dB vs the fractional power split for different λ	100
4.3	Beam beam-selection error with respect to beamwidth of the transmit antenna.	100
4.4	Distance estimation error vs physical data rate for different power budget.	101
4.5	Power allocation for the two services.	102
5.1	Beam selection error.	110
5.2	Beam-misalignment.	110
5.3	Average Beam Selection Error $\bar{\mathcal{P}}_{BS}$ varied with the beamwidth for different λ_s	114
5.4	SINR Coverage Probability $\mathcal{P}_C(T, N)$ varied with N for different β s	114
5.5	Rate Coverage Probability $\mathcal{P}_R(r_0, \beta, N)$ varied with N for different β s	115
5.6	Rate Coverage Probability $\mathcal{P}_R(r_0, \beta, N)$ varied with $(1 - \beta)$ for different λ_s and N	115
5.7	Average angle of arrival (AoA) estimation error varied with $(1 - \beta)$ for different N	116
D.1	Throughput comparison of mean cell approach with Poisson point process (PPP) distributed users.	145
D.2	Stable fraction of the network.	152
D.3	Analytical approximation accuracy, $G_0 = 36$ dB.	153

List of Abbreviations

4G fourth generation

5G fifth generation

AoA angle of arrival

AoD angle of departure

BCRLB Bayesian CRLB

BS base stations

CDF Cumulative density function

CF Closed-form

CRLB Cramer-Rao lower bound

EI Exponential Integral

eMBB enhanced mobile broadband

FIM Fisher Information Matrix

GPS global positioning system

GNSS global navigation satellite system

HetNets heterogeneous networks

LOS line of sight

MBS macro base station

MIMO Multiple Inputs Multiple Outputs

mm-wave millimeter wave

mMTC massive machine-type communications

MS mobile station

MVUE minimum-variance unbiased estimator

NLOS non line-of-sight

OFDM orthogonal frequency division multiplexing

PDF probability density function

PGF probability generating functional

PLCP Poisson line Cox process

PLT Poisson line tessellation

PLP Poisson line process

PPP Poisson point process

PV Poisson-Voronoi

QoS Quality of service

RAT radio access technique

RSSI received signal-strength indicator

SBS small cell base station

SINR signal to interference plus noise ratio

SNR signal to noise ratio

ULA uniform linear array

UE user equipment

URLLC ultra-reliable low-latency communications

V2V vehicle-to-vehicle

Chapter 1

Introduction

1.1 Future of Mobile Networks and 5G

We are living in an exciting time of wireless research. Not only the technological advances in this field have increased by leaps and bounds, but also the services supported by the wireless technologies have experienced a tremendous boom. The study of wireless networks is not longer a niche subject, but it has integrated itself into a plethora of industries, with use cases like intelligent transport systems, wireless power transfer, cyber-physical systems, and critical control of smart objects. In the context of cellular communication, we are witnessing extensive research efforts, and in parallel, standardization activities towards the 5G mobile systems. This thesis is within the purview of present and next-generation cellular communication systems, and reports findings that aim to equip the mobile operator with guidelines and dimensioning rules for the resource planning and the design of network deployment.

Devising effective solutions for the next generation mobile communications is the need of the hour, since as indicated by the visual network index report released by Cisco [1], the explosion of mobile data traffic will be of such a high order, that it cannot be supported by incremental improvements on the existing communication technologies. To quantify this growth, it is worth to note that the total data handled by the wireless networks has augmented from 3 exabytes in 2010 to about 190 exabytes in 2018, and is envisaged to cross 500 exabytes by 2020 [2].

In addition to this tremendous increase in the volume of data, the number of connected devices and the per-link data rate requirements will continue to grow exponentially. Due to the variety of applications and services planned to be offered in the 5G ecosystem, the number of connected devices is expected to cross tens or even hundreds of billions [3].

In this section, we summarize several key requirements that define the nature of the 5G mobile systems. Then, we present some key technologies proposed by the wireless research community that aim to address the key requirements.

1.1.1 Key Requirements of 5G

Data Rate

Undeniably, the need to support the ever-increasing demand for high data-rates services is the key driver of innovation in cellular communication systems. In this context, different metrics are used to characterize the system performance, as described below:

1. **Area spectral efficiency** refers to the amount of data the network can serve per second per unit area. The general consensus is that the area spectral efficiency will need to increase by roughly $1000\times$ from fourth generation (4G) to 5G [4].
2. The **cell-edge rate** is a measure of the worst-case data rate that a user can receive with a high degree of certainty. The target 5G cell-edge rate ranges from 100 Mbps (sufficient for supporting high-definition streaming) to as high as 1 Gbps. In reality, meeting 100 Mbps for 95 percent of users presents one of the most crucial technological challenges in the context of 5G [2].
3. Finally, **the peak physical data rate** represents the data rate that a user can receive in the best-case scenario. The 5G vision for the peak physical data rate is expected to be in the range of tens of Gbps [2].

Latency

Another important characteristic of the 5G ecosystem is the ability to provide ultra-low latencies for several applications. Currently, in the radio access network of 4G systems, the end-to-end round-trip time is of the order of 10-20 ms [5], which is sufficient for a majority of current cellular services [6]. However, the future wireless applications like two-way gaming, tactile Internet, and virtual reality need the cellular networks to be optimized for providing ultra-low latency. In fact, for several applications, the 5G access network will need to be able to support a round-trip latency as low as 1 ms [7]. This presents a challenge for the design of the sub-frame structure and the protocol stack.

Furthermore, reducing the latency in the core and the transport network is also a key requirement to reduce the end-to-end latency.

Reliability

In addition to supporting services characterized by high data-rates and very low-latency, one of the major novelties within the 5G ecosystem is the provisioning of ultra-reliable communications. In a nutshell, ultra-reliable communication aims at facilitating end-to-end successful¹ communication links up to 99.999% or even 99.99999% of the times [8]. Exemplary services in this mode include disaster search and rescue [9], tele-surgery [10], industrial automation [11] and reliable vehicle-to-vehicle (V2V) communication [12].

Massive Connectivity

Another feature of the future wireless networks is the need to support massive access by a large number of devices. It consists of providing wireless connectivity to tens of billions of often low-complexity low-power machine-type equipments. In the crux of these services is the need for scalable connectivity for an increasing number of devices, wide area coverage, and deep indoor penetration. A typical example of this type of service is the collection of the measurements from a large number of sensors, such as smart metering [13].

Energy Efficiency

As the 5G technologies are developed and deployment pick momentum, a major consideration will be to maintain the per-link energy [2]. A major consideration in this regard is to maintain the per-link energy costs. To go into details, as the per-link data rates offered by the operator increases by about $100\times$, the Joules per bit will need to diminish by at least $100\times$ [14] to maintain the revenue of the operators.

Flexible and Low-Cost Network Management

Finally, it is imperative to note that the future mobile networks must be optimized in terms of cost. For example, the 5G small cells should be $10\text{-}100\times$ cheaper to deploy than the legacy macro BSs for enabling the flexibility to deploy new services [15]. Another major cost consideration for 5G is the backhaul

¹The definition of "successful" depends on the actual applications.

from the network edges to the core. This is more crucial in the 5G networks as compared to the legacy 4G networks, due to the high BS densities and increased bandwidth [16].

1.1.2 Key Technologies for 5G

In this section we describe some of the key technologies to address the key requirements for 5G networks as described in Section 1.1.1. The technologies enumerated below do not present an exhaustive list in the context of 5G, and we focus only the ones relevant to this thesis.

1. Massive MIMO technology [17], which is based on the aggregation of a large number of antennas in the BS, is an important direction of research, specially for enhancing the data rate per node per unit of spectrum. Apart from the better throughput and spectrum efficiency, massive MIMO can also improve the improvement of the coverage performance of the network by exploiting transmit diversity [18] and beamforming techniques in mm-wave [19]. Furthermore, due to the possibility of parallel transmission of multiple data streams, massive MIMO also promises to reduce the communication latency.
2. Ultra-dense deployment of small cells [20] enables to bring the users closer to their access points. This enhances the downlink performance by augmenting the received power. Furthermore, due to the reduced proximity of the users to the BSs, the uplink transmit power is also reduced, which decreases the interference and improves the handset battery life [21]. It also presents the possibility of improving reliability in communications, owing to the multiple available proximal access points. Thus, a user can switch to a new access point, or transmit using multiple links [22], in case the link to the serving access point deteriorates.
3. Operating at higher frequency spectrum which were previously deemed unusable, specially at the mm-wave range [23], is another key direction of research. The higher frequency transmission will bring with it massive bandwidths, which would enhance the data rates.

Additionally, recently the enhanced positioning capability with mm-wave has been investigated [24]. In the future 5G networks, positioning will play an ever-increasing role, not only for location-based services like autonomous vehicles, but also for location-aware intelligent communication

solutions such as proactive radio resource management. It is widely believed that 5G architecture with ultra-densification, large antenna arrays, and wide bandwidths will provide excellent resources for efficient positioning and ranging.

4. Finally, network slicing [25] is expected to play a critical role in 5G networks because of the multitude of use cases and new services. These will place different demands on the network in terms of functionalities, and their performance requirements will vary significantly. Within the purview of network slicing, each virtual network (network slice) comprises an independent set of logical network functions that supports the requirements of the particular use case. Each slice will be optimized to provide the resources and network topology for the specific service to be supported. Thus, network slicing presents an attractive solution for enabling low-cost network management by optimizing the utility of physical infrastructure, i.e., communication, computational, and storage resources.

Other technological advancements such as enhanced interference management [26], non-orthogonal multiple-access (NOMA) [27], full duplex communications [28], carrier aggregation [29] etc., may also contribute to data-rate improvements.

In this thesis we deal with some of these technologies and characterize and optimize the coverage, the downlink data-rate, and the localization performance of cellular users operating within different deployment geometries of mm-wave small cells. In what follows, we discuss mm-wave and multi-RAT communications in the context of 5G. Then, we introduce the notion of stochastic geometry, which is a mathematical tool for analyzing complex heterogeneous networks involving multiple tiers and RATs.

1.2 Mm-Wave and Multi-RAT Challenges

1.2.1 Mm-wave Communications

The limited bandwidth of the traditional frequency bands is expected to fall short of providing sufficient resources for sustaining the high data rates envisaged for the future wireless applications. As mentioned in the previous section, one key direction of research in this regard is the usage of higher frequencies, specifically in the mm-wave band from 30 GHz to 300 GHz. Most of the current work in the context of mm-wave communication is focused on the 28 GHz

band [30], the 38 GHz band [31], the 60 GHz band [32], 71–76 GHz band and the 81–86 GHz band [33]. In fact, for indoor wireless personal area networks (WPAN) or wireless local area networks (WLAN), several standards with mm-wave technology are already defined, such as the IEEE 802.15.3c [34] and IEEE 802.11ad [35]. This stimulates growing interests for the study and experimentation of mm-wave transmissions in cellular systems.

However, transmissions in such high frequencies are heavily susceptible to blockages by obstacles (e.g., humans and vehicles) [36, 37]. This is precisely due to the fact that the electromagnetic waves fail to diffract significantly around obstacles of size larger than the wavelength. For example, blockage by a human penalizes the mm-wave link budget by 20-30 dB [38]. Furthermore, the rain attenuation and atmospheric and molecular absorption characteristics of the mm-wave propagation limit the range of communications [23]. Therefore, maintaining a reliable connection, specially for delay-sensitive applications such as high-definition broadcasting/multi-casting is a big challenge for mm-wave communications.

The signal loss due to attenuation in the mm-wave band can be efficiently mitigated using beamforming techniques, with large number of antennas [39]. As the wavelengths are shorter in the mm-wave frequency bands, antennas are consequently smaller. Thus, deploying a large number of antennas in a given area becomes feasible. By tuning each antenna element, the antenna array can steer the mm-wave beam towards the desired direction and provide high antenna gain, while simultaneously reducing the gain in other directions. Consequently, the highly directional antennas also reduces the co-channel interference [40].

On the downside, thin beamwidths pose new challenges in terms of ubiquitous coverage and user tracking. Furthermore, providing initial access to standalone mm-wave BS presents a difficult design challenge [41]. To make the transmitter and receiver direct their beams towards each other, the procedure of beam training is needed, which may result in an increased access delay [42].

In the context of both providing initial access and enhancing communication reliability, one solution consists of using the sub-6GHz band to aid the mm-wave links [43]. Specifically, from the initial access point of view, given suitable signal processing mechanisms, the position and orientation of the users relative to a sub-6GHz BS can be determined [44]. If sub-6GHz and mm-wave BS are co-located, or their position and orientation relative to one another are known,

the coarse-grained angle information for beam-training of the mm-wave radio-frequency (RF) front-end can be derived easily, which significantly speeds up the initial access procedure. On the other hand, from the reliability point of view, efficient algorithms need to be devised to switch the data transfers from the high-speed mm-wave links to the more reliable sub-6GHz links when the quality of the former degrades [45].

Due to this reliance on the legacy bands for operation, it is unrealistic to assume ubiquitous coverage with only mm-wave small cells, and it is envisioned that multiple RATs will co-exist in future cellular networks [46] [47]. In what follows, we briefly discuss the concept of multi-RAT association, its requirements, and the modeling challenges associated with it. This gives us a motivation for the stochastic modeling of complex multi-RAT networks, which forms the crux of this thesis.

1.2.2 Multi RAT Association

As the 5G technologies evolve, and the new radio deployment picks momentum, the cellular networks will become more and more heterogeneous. As discussed in the previous sub-section, a key feature therein will be the increased integration and interoperability between different RATs, specially different radio bands [48]. An illustration of a 5G cellular deployment is shown in Figure 1.1. Here multi-RAT and standalone mm-wave small cells are deployed on top of the existing macro and small cell architecture [45]. It is clear that typical 5G devices should be able to support not only new 5G standards (e.g., operation at mm-wave frequencies), but also be backward compatible with respect to the 3G and 4G LTE standards. In this context, accurate modeling of the cellular networks is needed for efficient design of user association algorithms with different tiers and RATs, which results in the improvement of user performance [49]. For example, even a simple inter-cell interference scheme consisting of cell range expansion and almost-blank sub-frames, has been shown to increase edge rates by as much as 500 percent [50]. In this thesis, we consider small cells overlaid on top of the macro architecture and equipped with multi-RAT antennas, thereby enabling them to opportunistically switch between mm-wave and the sub-6GHz bands. In this context, we study the optimal user association with the different tiers and RATs to address different performance objectives such as load balancing, user throughput, and deal with diverse requirements of 5G services.

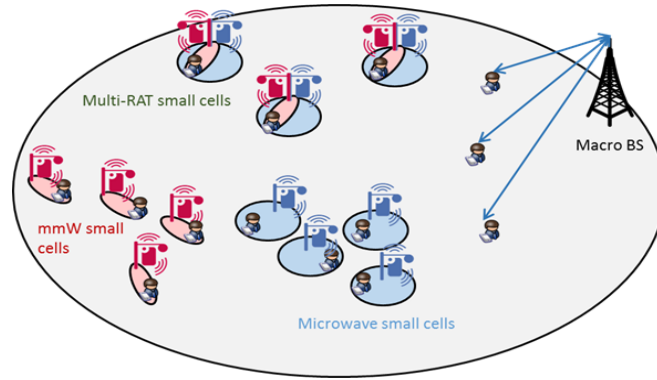


FIGURE 1.1: An illustration of 5G cellular architecture consisting of mm-wave multi-RAT small cells.

The existence of multiple RATs, in addition to the increased ad-hoc deployments of the access points, leads to a complex heterogeneous architecture, which can be difficult to model and analyze [14]. Additionally, determining the optimal user association with the access points, and the selection of radio bands therein, presents a difficult combinatorial optimization problem [49]. This is further complicated by the fact that future wireless applications will have diverse requirements, not all of which can be modeled by a limited set of performance metrics [51]. In the following section, we introduce the notion of stochastic geometry, which is a mathematical tool that has gained popularity in the modeling and analysis of the large scale, complex, multi-tier multi-RAT networks.

1.3 Stochastic Geometry Based Modeling

One of the main tools that has recently gained interest to tackle the modeling challenge of cellular networks is stochastic geometry [52]. Specifically, stochastic geometry models the positions of the nodes of the network (BSs, users, etc.) as stochastic processes. Subsequently, it enables the operator to perform efficient initial resource planning and dimensioning of the cellular networks prior to the actual deployments [53]. In what follows, we first highlight some basic notions of stochastic geometry analysis. Then, we briefly describe a classical SINR modeling in single-tier large-scale networks, so as to introduce the elements of stochastic geometry to the reader. For a rigorous and complete mathematical treatment of stochastic geometry based modeling of wireless networks, the reader may refer to the works by Chiu et al. [52] and Baccelli et al. [54]

1.3.1 Key Notions of Stochastic Geometry

- **Point processes:** A point process is a measurable mapping ϕ from a probability space to the space of point measures² on some space \mathcal{E} . The process ϕ can be denoted by a sum of Dirac measures on \mathcal{E} :

$$\phi = \sum_i \delta_{X_i},$$

where $\{X_i\}$ represent the points of ϕ . In this thesis, the space \mathcal{E} is the Euclidean space \mathbb{R}^d of dimension $d \in \{1, 2\}$.

- **Intensity measure:** The intensity measure Λ of ϕ is defined as $\Lambda(B) = \mathbb{E}[\phi(B)]$ for Borel B , where $\phi(B)$ denotes the number of points in $\phi \cap B$. Thus, the intensity measure represents the expected number of points of the point process in a given Borel set B .
- **PPP:** Let Λ be a locally finite measure on \mathbb{R}^d . A point processes ϕ is Poisson on \mathbb{R}^d if the following conditions hold true:

1. For all disjoint subsets A_1, \dots, A_n of \mathcal{E} , the random variables $\phi(A_i)$ are independent, and
2. For all sets A of \mathcal{E} , the random variables $\phi(A)$ are distributed according to a Poisson random variable with parameter Λ .

An important property of the PPP used throughout this thesis is that: conditionally on the fact that $\phi(A) = n$, the n points in A are independently (and uniformly for homogeneous PPP) located in A .

- **Laplace functional:** The Laplace functional evaluated for a function f is defined for point processes ϕ as:

$$L(f) = \mathbb{E} \left[\exp \left(- \int_{\mathbb{R}^d} f(x) \phi(dx) \right) \right] = \mathbb{E} \left[\exp \left(- \sum_{X_i \in \phi} f(X_i) \right) \right]. \quad (1.1)$$

- **Probability generating functional:** The probability generating functional (PGF) of a point process ϕ evaluated for a function ν is defined

²A point measure is a measure which is locally finite and which takes only integer values.

mathematically as the Laplace functional of $-\log \nu$, and is calculated as:

$$G_\phi(\nu) = \mathbb{E} \left[\prod_{x_i \in \phi} \nu(x_i) \right], \quad (1.2)$$

where the expectation is with respect to ϕ .

- **Palm probability:** The Palm probability refers to the probability of an event conditioned on a point of the process being located at a given position. Accordingly, the Palm distribution represents how the point process would look when viewed from one of its atoms (points).
- **Slivnyak's theorem:** Slivnyak's theorem [52] for a PPP (ϕ) states that conditioning on the event that a point of ϕ is located at the origin (o) (in other words $o \in \phi$), is equivalent to *add* a point at o to the PPP ϕ . Mathematically,

$$\mathbb{P}(\phi \in Y | o) = \mathbb{P}(\phi \cup \{o\} \in Y),$$

where Y is any point process property.

This can be thought of as removing an infinitesimally small area corresponding to a ball $B(x, r)$ for $r \rightarrow 0$, since the distributions of points in all non-overlapping regions are independent for a PPP. This means that any property seen from a point o is the same whether or not we condition on having a point at o in ϕ .

With these definitions in mind, in the following section, we describe how stochastic geometry fundamentals can be used to characterize the downlink SINR of a single tier network.

1.3.2 SINR Coverage in Single-Tier Networks

In large-scale cellular networks, the received signal power at an average user is a random variable, due to the uncertainty in the spatial distribution of the serving BS and the users, and due to channel fading [53]. Additionally, due to concurrent co-channel transmissions throughout the network, the interference power is governed by a number of different stochastic processes e.g., the spatial distribution of the location of the interfering BSs, the random shadowing, and fading [55]. Mathematically, the SINR for a receiver placed at the origin o can

be written as:

$$\text{SINR} = \frac{S}{N + I}, \quad \text{where } S = P_t h_t \ell(\|x_t\|), \quad I = \sum_{i \in T} P_i h_i \ell(\|x_i\|), \quad (1.3)$$

where S , N , and I are the desired signal, noise, and interference powers, respectively. The subscript t refers to the transmitter, which can be selected according to an association scheme such as maximum downlink power association or nearest-BS association. The summation for the calculation of I is taken over the set of all interfering transmitters T . Here, P_i is the transmit power, and h_i is a random variable that characterizes the cumulative effect of shadowing and fast-fading from the transmitter $i \in T$. The path loss function ℓ is assumed to depend only on the distance $\|x_i\|$ from the origin to the interferer situated at position x_i in space. In general, T , h_t , h_i , x_t and x_i , and possibly P_i are random quantities. Thus, characterizing the average SINR is a difficult challenge to address. However, thanks to the results from stochastic geometry, and some convenient, yet meaningful assumptions, the complementary CDF of the SINR (or the SINR coverage probability) can be easily derived. In simple terms, the SINR coverage probability $\mathcal{P}_C(\gamma)$ is the probability that an average user in the network receives an SINR above a certain threshold γ . In other words, it represents the fraction of the users under coverage in the network with respect to an SINR threshold γ .

Let us assume that the locations of the set of interfering BSs are modeled as points of a PPP. Furthermore, we assume that the fast-fading in all the links are independent and distributed according to a Rayleigh distribution with variance equal to one³. Then, mathematically, we have:

$$\begin{aligned} \mathcal{P}_C(\gamma) &= \mathbb{P} \left(\frac{P_t h_t \ell(\|x_t\|)}{N + \sum_{i \in T} P_i h_i \ell(\|x_i\|)} \geq \gamma \right) \\ &= \mathbb{P} \left(h_t \geq \frac{\gamma (N + \sum_{i \in T} P_i h_i \ell(\|x_i\|))}{P_t \ell(\|x_t\|)} \right) \\ &\stackrel{(a)}{=} \mathbb{E} \left[\exp \left(- \frac{\gamma (N + \sum_{i \in T} P_i h_i \ell(\|x_i\|))}{P_t \ell(\|x_t\|)} \right) \right] \\ &\stackrel{(b)}{=} \mathbb{E} \left[\exp \left(- \frac{\gamma N}{P_t \ell(\|x_t\|)} \right) \mathbb{E} \left[\exp \left(- \frac{\gamma \sum_{i \in T} P_i h_i \ell(\|x_i\|)}{P_t \ell(\|x_t\|)} \right) \right] \right] \end{aligned}$$

³These are standard assumptions for the modeling of sub-6 GHz networks [56]. In this thesis, we will outline other assumptions regarding the network geometry based on the deployment scenario investigated in each case.

$$\stackrel{(c)}{=} \mathbb{E} \left[\exp \left(-\frac{\gamma N}{P_t \ell(\|x_t\|)} \right) \mathbb{E} \left[\prod_{i \in T} \exp \left(-\frac{\gamma P_i h_i \ell(\|x_i\|)}{P_t \ell(\|x_t\|)} \right) \right] \right]. \quad (1.4)$$

Here step (a) follows from the exponential distribution of the random variable h_t . In step (b), the outer expectation is with respect to the serving BS, whereas the inner expectation is with respect to the positions of the interfering BSs. Step (c) follows from the fact that the exponential of the sum equals the product of the exponentials. Now the second part of the above expression is evaluated using classical results from stochastic geometry as follows:

$$\begin{aligned} & \mathbb{E} \left[\prod_{i \in T} \exp \left(-\frac{\gamma P_i h_i \ell(\|x_i\|)}{P_t \ell(\|x_t\|)} \right) \right] \\ & \stackrel{(d)}{=} \exp \left(-\int 1 - \mathbb{E} \left[\exp \left(-\frac{\gamma P_i h_i \ell(\|x\|)}{P_t \ell(\|x_t\|)} \right) \right] \Lambda(dx) \right) \\ & \stackrel{(e)}{=} \exp \left(-\int 1 - \frac{1}{1 + \frac{\gamma P_i \ell(\|x\|)}{P_t \ell(\|x_t\|)}} \Lambda(dx) \right). \end{aligned} \quad (1.5)$$

Here, step (d) follows from the evaluation of the PGF of the PPP [52]. The expectation inside the exponential is with respect to the independently and identically distributed (i.i.d.) exponential random variables h_i , and accordingly, in step (e) we use the Laplace functional of h .

For some special cases of path-loss functions the expression (1.5) and hence (1.4) can be easily computed. As an example, let us assume that $P_i = P_t \forall i$ and $\ell(\|x\|) = K \cdot \|x\|^{-2}$ [45]. Then (1.5) becomes:

$$\mathbb{E} \left[\prod_{i \in T} \exp \left(-\frac{\gamma P_i h_i \ell(\|x_i\|)}{P_t \ell(\|x_t\|)} \right) \right] = \exp \left(-\int_{x_t}^{\infty} \frac{\gamma \|x\|^{-2}}{\gamma \|x\|^{-2} + \|x_t\|^{-2}} \lambda dx \right) \quad (1.6)$$

Thus, the characterization of the SINR becomes simpler as compared to evaluating the statistical properties of (1.3) directly⁴. In Figure 1.2 we plot the SINR coverage probabilities for two cases of transmit powers. The higher transmit power results in an improved SINR coverage probability.

The CDF of the SINR is then studied to derive meaningful insights on the user performance in a network. For example, the outage probability of an

⁴It must be noted that this analysis is just one example of wireless network characterization using stochastic geometry. For a detailed discussion of stochastic geometry modeling of wireless networks, the reader may refer to the work by Andrews et al. [56]

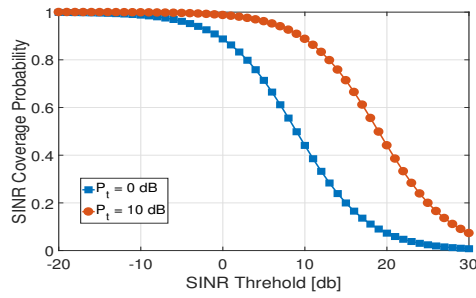


FIGURE 1.2: SINR coverage probability vs SINR threshold with respect to different transmit powers.

average user in the network is calculated directly as one minus the coverage probability. Furthermore, once the CDF of the SINR is derived, the downlink data-rate coverage (\mathcal{P}_R) probability is then easily characterized as follows:

$$\mathcal{P}_R(R_0) = \mathcal{P}_C \left(2^{\frac{R_0}{B}} - 1 \right). \quad (1.7)$$

The data-rate coverage probability denotes the fraction of users in the network that receive a data-rate of more than R_0 bps. The SINR and the rate coverage probability of the users are further used to derive other non-trivial performance metrics such as the network load [57] the user throughput [45]. In this thesis, we define and study several of these metrics in the context of the key requirements of 5G, with varying deployment geometries, physical blockages (e.g., due to buildings), as well as moving objects such as vehicles. Thereby, we provide a realistic evaluation of the mm-wave multi-RAT networks for aiding the operators for the deployment of the future 5G architecture.

1.4 Bound-Based Characterization of mm-wave Positioning

In the 5G cellular networks, highly accurate position information will be a necessity, especially due to the exponential increase of the device-centric and context-aware applications [58]. Conventional positioning techniques using global positioning system (GPS) and terrestrial radio-location technologies that rely on the existing wireless communication standards such as Bluetooth and WiFi are expected to fall short of addressing the positioning accuracy needed for the future wireless applications. This is precisely due to the fact that these existing solutions provide positioning accuracy of a few meters at best [59, 60]. In this

context, the mm-wave technology operating in large available bandwidths with compact and highly directive antenna arrays, and hence, to the capability of getting spatialized information with very high reactivity under device mobility, offers an attractive solution [23]. Furthermore, with the advent of massive deployment of small cells, there will be an increasing number of anchor nodes to aid to the localization accuracy [61, 62]. Thus, on the one hand, the mm-wave infrastructure can be utilized for highly accurate positioning. Whereas, on the other hand, to facilitate effective data-communication for 5G application using mm-wave beams, accurate positioning will be necessary for functionalities such as initial access, user tracking etc [2]. The position information can not only be considered as an add-on feature, but rather an integral feature necessary for the communications [58].

Benchmarking localization performance in wireless networks has traditionally been done using the Cramer-Rao lower bound (CRLB), which provides a lower bound on the position or orientation error of any unbiased estimator [63]. Common practice has been to analyze the CRLB in fixed scenarios of anchor nodes and a target. This strategy produces a scalar/fixed value for the CRLB and is specific to the scenario being analyzed. Although these analyses give meaningful insights about the positioning performance, it fails to take into account the randomness in the location of the nodes in the network. In random networks, as the position of the nodes being localized (e.g., a UE in a cellular network) or the anchor nodes (such as a SBS) are stochastic and follow different distributions, the CRLB itself becomes a random variable [64]. In this thesis, we evaluate the statistical characteristics of the CRLB of the position estimates of randomly located users based on received signal-strength indicator (RSSI) measurements.

As an example, in what follows, we describe the CRLB formulation based on RSSI measurements in a one-dimensional network (such as on-road deployment of SBSs). Let the transmit power of the anchor SBS be given by P_L , and let us assume that the SBSs are of height h_B , and equipped with directional antennas of gain G_0 . Let each user be localized by its nearest SBS. Using our previously described notions of stochastic geometry, we can derive the distance distribution of the nearest SBS for a deployment density of λ as:

$$f_d(x) = 2\lambda \exp(-2\lambda x) \quad (1.8)$$

Now, if the transmit signal for localization is $x(t)$, the received signal can be written as:

$$y(t) = \frac{\sqrt{KG_0P_L}}{(h_B^2 + d^2)^{\frac{\alpha}{4}}} x(t) + n(t), \quad (1.9)$$

where $n(t)$ is a zero mean additive white Gaussian noise resulting in estimation errors. In the following lemma, we calculate the Fischer information for the estimation of d using RSSI measurements. Then, the CRLB, i.e., a lower bound on the variance of any unbiased estimator of d , is the inverse of the Fisher information.

Lemma 1. *The expected value of the Fisher information for the estimation of the distance (d) is calculated as:*

$$J_D = \frac{KG_0P_L 2\lambda \bar{f}^2}{\sigma_N^2} \int_1^\infty \frac{e^{-2\lambda x}}{(h_B^2 + x^2)^{\frac{\alpha}{2}}} dx, \quad (1.10)$$

where $\bar{f}^2 = 1.25\pi^2 B^2$. Furthermore, the prior information is: $J_p = \log(2\lambda) - 1$.

Proof. The Fisher information for a given d is [63]:

$$J_d = \frac{KG_0P_L}{(h_B^2 + d^2)^{\frac{\alpha}{2}} \sigma_N^2} \bar{f}^2, \quad (1.11)$$

where $\bar{f}^2 = \frac{\int_{-\infty}^{\infty} (2\pi f)^2 |X(f)|^2 df}{\int_{-\infty}^{\infty} |X(f)|^2 df}$ is the effective bandwidth of the signal. In our case, we assume that the signal has a flat spectrum [24], and accordingly, we have $\bar{f}^2 = 1.25\pi^2 B^2$. Now using the distribution of d from (1.8), the expectation of the Fisher information is calculated as:

$$J_D = \mathbb{E}_d [J_d] = \frac{KG_0P_L 2\lambda \bar{f}^2}{\sigma_N^2} \int_1^\infty \frac{e^{-2\lambda x}}{(h_B^2 + x^2)^{\frac{\alpha}{2}}} dx. \quad (1.12)$$

Finally, the prior information can be calculated as:

$$\begin{aligned} J_p &= \mathbb{E} [\log(f_d(x))] = \int_0^\infty \log(f_d(x)) f_d(x) dx \\ &= \int_0^\infty \log(2\lambda \exp(-2\lambda x)) 2\lambda \exp(-2\lambda x) dx \\ &= \log(2\lambda) - 1 \end{aligned}$$

This completes the proof. □

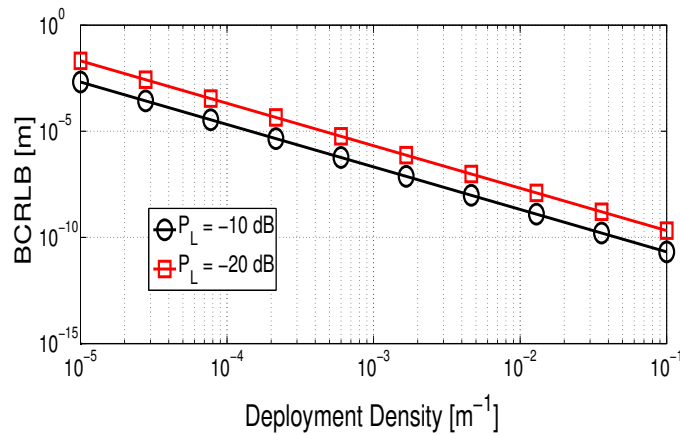


FIGURE 1.3: The BCRLB with varying deployment densities for two values of transmit power.

Finally, the Bayesian information can be obtained as $J_B = J_D + J_P$. Consequently, the BCRLB and Jeffrey's prior, (which is simply the square root of the Bayesian information) corresponding to the Bayesian information are calculated as $\frac{1}{J_B}$ and $\sqrt{J_B}$, respectively.

We study the BCRLB for a mm-wave system with 1 GHz bandwidth. In Fig. 1.3 we plot the BCRLB with respect to the deployment densities for two values of transmit powers. We notice that as the deployment gets more dense, the positioning accuracy increases due to closer proximity of the UE to the serving SBS. The positioning accuracy improves with increasing transmit power as well. We observe a linear relationship between the BCRLB and the deployment density in the log domain. Finally, it is interesting to note that the variance of positioning error is in the sub-meter range with mm-wave. In Part II of this thesis, we characterize and optimize the positioning error of the UE in the network in relation to their data-communication performance.

Now, we summarize the overall contributions of the thesis in the next section.

1.5 Contributions and Organization

This thesis begins with the definition and characterization of performance metrics of multi-tier heterogeneous networks (HetNets) with multi-RAT mm-wave small cells. First, we consider a homogeneous deployment of the BSs and study the coverage performance of the users in the network. We propose cell range expansion algorithms for enhancing coverage performance or to facilitate efficient load-balancing in multi-RAT HetNets. Then, we consider a more realistic

deployment geometry in the context of urban scenarios, where the multi-RAT small-cells are deployed along the roads of a city. We perform coverage analysis of the users in this network and propose cell range expansion algorithms primarily aimed at service differentiation in the context of 5G. Finally, for this urban scenario with on-road deployment of small cells, we characterize a network deployed to support simultaneous positioning and communication services.

The thesis is broadly organized into two parts. The first part (Chapters 2-4) deals with the modeling and performance analysis of multi-tier and multi-RAT networks with mm-wave small cells.

In Chapter 2, we characterize a two tier heterogeneous network, consisting of classical sub-6GHz macro cells, and multi RAT small cells able to operate in sub-6GHz and mm-wave bands. For optimizing coverage and to balance loads, we propose a two-step mechanism based on two biases for tuning the tier and RAT selection, where the sub-6GHz band is used to speed-up the initial access procedure in the mm-wave RAT. First, we investigate the effect of the biases in terms of SINR distribution, cell load, and user throughput. More specifically, we obtain the optimal biases that maximize either the SINR coverage or the user downlink throughput. Then, we present one of the first studies of dynamic traffic of a cellular network using stochastic geometry, and characterize the network load. Using this result, we derive upper bounds on the overloading probabilities of each tier. Finally, for a given traffic density, we provide the small cell density required to satisfy system constraints in terms of overloading and outage probabilities. Our analysis highlights the importance of using multi-RAT technology in particular when small cells are sparsely deployed or in case of heavy traffic.

In Chapter 3, in order to realistically characterize the user performance, we model the position of the mm-wave multi-RAT small cells along roads. A BS located sufficiently close, but on a different street than that of a UE may not provide sufficient downlink power to the UE due to blockages by buildings, which is not straightforward to capture using single or multiple LOS ball models. First, we provide tractable, yet realistic models to characterize the mm-wave interference and the effect of vehicular blockages on the mm-wave signals. Then, we introduce an association policy where a user selects the serving tier using the powers measured on the sub-6GHz band, and then, using the biased power of the mm-wave band selects the RAT. Based on this, we derive the SINR coverage probabilities of pedestrian users. We investigate the effect of the the

vehicular density on the user performance and optimize the RAT selection bias with respect to vehicular blockage, SINR coverage probability, and rate coverage probability. Our analysis highlights that the operator should implement a varied range of RAT selection biases to support the diverse applications of the 5G mobile systems. Accordingly, we provide a slice-aware RAT selection strategy to support three types of services characterized by different requirements in terms of reliability, coverage, and data rates.

Part II (Chapters 4 and 5) deals with the joint characterization of positioning and communication performance of users using mm-wave communications. Particularly, in Chapter 5, we revisit our millimeter wave network deployed along the streets of a city, and characterize the user performance in terms of positioning and downlink data-rate performance, respectively. First, we present a transmission scheme where the BS provide jointly positioning and data-communication functionalities. Accordingly, we study the trade-off between the localization and the data rate performance based on theoretical bounds. Then, we obtain an upper bound on the probability of beam misalignment based on the derived localization error bound. Finally, we prescribe the network operator a scheme to select the beamwidth and the splitting factor between the localization and communication resources to address different service requirements, while limiting cellular outage.

In Chapter 5, we propose an optimal beamwidth selection policy maximizing the rate coverage for a localization assisted mm-wave network. We formulate the localization performance in terms of delay and AoA and down-link rate performance (in terms of rate coverage probability) of a mm-wave network deployed along the streets of an urban environment. We study the trade-off between localization and communication performance with respect to the resources allotted to these functionalities, and accordingly, we characterize the optimal beamwidth selection strategy based on this trade-off. With more energy allocated for precise localization, we have a lower beam selection error, although it reduces the energy available for communications and hence the rate performance. Conversely, we obtain better rate performance with more energy allocation to communication while increasing the chance of beam selection error due to less precise localization.

Patents and Publications

Patents

[P4] **G. Ghatak**, R. Koirala, A. De Domenico, and B. Denis, *Initial Access Scheme for Positioning Assisted mm-Wave Service*. [In Preparation]

[P3] **G. Ghatak**, R. Koirala, A. De Domenico, and B. Denis, *Beam Dictionary Design and Resource Partitioning Scheme for Positioning Assisted mm-Wave Service*. [In Preparation]

[P2] **G. Ghatak**, A. De Domenico, and M. Coupechoux, *RAT Selection Method for mm-Wave multi-RAT Small Cells for QoS Optimization of 5G Services*. [In Preparation]

[P1] **G. Ghatak**, A. De Domenico, *Load Balancing Method in a Heterogeneous Multi-Technology Radio Access Network*, (EU, FR, US) E.N. 17 58112, Filing Date: 1/9/2017.

Journal papers

[J6] **G. Ghatak**, A. De Domenico, and M. Coupechoux, *Relay Placement for Reliable Localization in Cooperative mm-Wave Systems*, (To be submitted).

[J5] **G. Ghatak**, R. Koirala, A. De Domenico, B. Denis, D. Dardari, B. Uguen and M. Coupechoux, *Rate Analysis and Beamwidth Optimization for Positioning-Assisted mm-Wave Service*, (To be submitted).

[J4] **G. Ghatak**, A. De Domenico, and M. Coupechoux, *Small Cell Deployment Along Roads: Coverage Analysis and Slice-Aware RAT Selection* (Revised and re-submitted to IEEE Transactions on Communications).

[J3] **G. Ghatak**, M. Matthe, A. Banerjee, and G. P. Fettweis, *On Preambles With Low Out of Band Radiation for Channel Estimation* (Major Revision submitted to Elsevier Physical Communication).

[J2] **G. Ghatak**, A. De Domenico, and M. Coupechoux, *Coverage Analysis and Load Balancing in HetNets with mmWave Multi-RAT Small Cells*, in IEEE Transactions on Wireless Communications, vol. 17, no. 5, pp. 3154-3169, May 2018. doi: 10.1109/TWC.2018.2807426

[J1] A. Chatterjee, G. K. Mahanti, and **G. Ghatak** . *Synthesis of satellite footprint patterns from rectangular planar array antenna by using swarm-based optimization algorithms*. International Journal of Satellite Communications and Networking, 32(1), 25-47.

Conference Papers

[C7] **G. Ghatak**, S. R. Khosravirad and A. De Domenico, *Stochastic Geometry Analysis of Cooperative Industrial Wireless Control*, IEEE Wireless Communications and Networking Conference (WCNC), Marrakech, Morocco, April 2019 (Submitted)

[C6] R. Koirala, **G. Ghatak**, B. Denis, D. Dardari, B. Uguen and A. De Domenico, *Throughput Characterization and Beamwidth Selection for Positioning-Assisted mmWave Service*, Asilomar Conference on Signals, Systems and Computers, October 2018, Pacific Grove, USA.

[C5] **G. Ghatak**, A. De Domenico, M. Coupechoux, *Accurate Characterization of Dynamic Cell Load in Noise-Limited Random Cellular Networks*, IEEE 88th Vehicular Technology Conference (VTC2018-Fall), August 2018, Chicago, USA.

[C4] **G. Ghatak**, R. Koirala, A. De Domenico, B. Denis, D. Dardari and B. Uguen, *Localization Data-Rate Trade-off in Small Cells and Service Differentiation for 5G Networks*, IEEE 87th Vehicular Technology Conference (VTC2018-Spring), June 2018, Porto, Portugal.

[C3] **G. Ghatak**, A. De Domenico, M. Coupechoux, *Modeling and Analysis of HetNets with mm-Wave Multi-RAT Small Cells Deployed Along Roads*, IEEE Global Communications Conference (GLOBECOM) December 2017, Singapore.

[C2] **G. Ghatak**, A. De Domenico, M. Coupechoux, *Performance Analysis of Two-Tier Networks with Closed Access Small-Cells*, IEEE 14th International Symposium Modeling and Optimization in Mobile, Ad Hoc, and Wireless Networks (WiOpt), May 2016, Arizona, USA.

[C1] A. Ghosh, **G. Ghatak**, and A. Chandra, *SEP of dual-ring star-QAM over FSO channels with atmospheric turbulence*, In IEEE International Conference on Signal Processing and Communications (SPCOM), July 2014, Bangalore, India .

Part I

Modeling and Performance Analysis of Multi-Tier Networks with mm-Wave Multi-RAT Small Cells

Chapter 2

Coverage Analysis and Load Balancing in HetNets with mm-wave Multi-RAT Small Cells

2.1 Introduction

Future cellular networks will require a tremendous increase in data rates. This multi-fold enhancement cannot be achieved through incremental improvements on existing schemes [2]. For this, two techniques are particularly attractive: network densification using small cells [65] and mm-wave wave communications [23]. Densification of cellular networks consists of massive deployments of small cells, overlaying the existing macro cell architecture. Traditionally, small cells are deployed in sub-6GHz frequencies with the aim of offloading macro-cells. This calls for Inter-Cell Interference Coordination [66, 67] and load balancing [68]. To further increase the data rates, mm-wave small cells, providing a very high bandwidth, are gaining popularity. Apart from the large bandwidths, mm-wave communication comes with highly directional antennas, which greatly reduces the co-channel interference [40]. Transmissions using higher frequencies suffer from larger attenuation and high sensitivity to blockages [36, 37]. The attenuation in mm-wave can be efficiently mitigated using beamforming techniques, with large number of antennas. As the wavelength is shorter, antennas are also smaller than in sub-6 GHz bands, so that deploying many more antennas becomes feasible. The highly directional antenna patterns pose in turn new issues in terms of coverage and user tracking. Moreover, providing initial access to standalone mm-wave base stations using beamtraining

with thin beams presents a difficult challenge [41]. In this regard, the sub-6GHz band can be used to aid the initial access mechanism [43]. Specifically, given suitable signal processing mechanisms, the position and orientation of the users relative to a sub-6GHz BS can be determined (see e.g., [44]). If sub-6GHz and mm-wave BS are co-located, or their position and orientation relative to one another are known, the coarse-grained angle information for beamtraining of the mm-wave RF front-end can be derived easily, which significantly speeds up the initial access procedure. As a result, it is unrealistic to assume ubiquitous coverage with only mm-wave small cells, and it is envisioned that multiple RAT will co-exist in future cellular networks [46] [47].

In this chapter, we analyze the SINR distribution, the cell load, and the downlink user throughput in a heterogeneous network with multi-RAT small cells using stochastic geometry. In order to optimize the user's SINR or to balance loads between tiers and RATs, we propose a cell association scheme based on two biases. In addition, we show the interest of deploying multi-RAT small cells to improve users' QoS.

2.1.1 Related Work

Elsawy et al., have presented a comprehensive survey on stochastic geometry to model multi-tier cellular networks [53]. The SINR and physical data rate distributions have been derived in the literature by Bai et al. [69] for single-tier mm-wave networks, by Singh et al. [70] for multi-tier sub-6GHz and by Di Renzo for mm-wave networks [71]. In case of small cells operating in the same band of the macro cell, Singh et al. [70], have shown that, without advanced interference management techniques, the SINR decreases with increasing offloading bias. On the contrary, in this chapter, we investigate how employing mm-wave in conjunction with sub-6GHz in small cells affects the system performance, and we show that optimizing the offloading biases can increase the user's SINR.

In the context of random networks, Yao et al. [72], similar to Di Renzo [71] have characterized the SINR coverage probability and the physical data rate in a multi-tier mm-wave network. However, the authors have not studied how traffic dynamics in a multi-user scenario impacts the network performance and the average user throughput. On the other hand, Elshaer et al. [73] have analyzed a multi-tier network with sub-6GHz macro cells and mm-wave small cells. They have derived the SINR coverage probability as a function of the tier association bias, and they have shown only by simulations that a non-trivial

optimal tier selection bias may exist. They have also investigated the relation between the association bias and throughput but without considering dynamic traffic. Moreover, they have characterized the load by using the average number of associated users in a cell; although, for a more realistic characterization, a dynamic traffic model should be considered. Furthermore, they have not optimized the user throughput while considering SINR outage constraints as well as overloading constraints.

In this perspective, Bonald and Proutiere [74] have studied the relations between the traffic arrival rate and the cell load for a single cell scenario. In the case of single-tier cellular network, Blaszczyzyn and Karray [57] have approximated the cell load by a mean-cell approach to calculate the number of active users in a cell and the average user throughput. We leverage on these studies to design the optimal load balancing in multi-RAT heterogeneous networks and to derive bounds on overloading probabilities.

2.1.2 Contributions and Organization

The contributions of this chapter can be summarized as follows:

- **SINR Coverage in a multi-RAT Heterogeneous Network:** By using stochastic geometry, we derive the association probabilities and the SINR distribution of a typical user in a multi-RAT heterogeneous network with small cells operating in sub-6GHz and millimeter wave bands. In the literature, SINR coverage and throughput analyses have not been performed so far for such a system model.
- **Association Scheme for Tier and RAT Selection:** We introduce a mechanism based on two biases, Q_T and Q_R , for tuning the tier and RAT selection, respectively. The principle of using biased received power for association has been used so far for tier offloading, whereas in this chapter, we introduce a second bias to distribute the users between the available RATs in the small cells. Using these biases, we propose a two-step association scheme, in which initial access is performed in the sub-6GHz band. We compare our association mechanism with a more natural and exhaustive one-step association procedure in terms of sub-optimality of biased received power and downlink throughput. We show that this two-step association scheme fares better than cell association with beamtraining

in mm-wave in terms of downlink throughput, specially in case of higher access delays.

- **Bias Optimization for SINR Coverage:** Contrary to single-RAT heterogeneous networks, biasing the received power can lead to an improved SINR in a multi-RAT system. However, bias optimization is difficult in general. In the general case, Q_T and Q_R can be obtained by brute force if the range of possible values is small. To limit the complexity of this approach, we provide a strategy that sets Q_R based on the ratio of the approximated mean SINR in sub-6GHz band and mm-wave. Thereafter, Q_T is obtained using a random-restart hill-climbing algorithm with adaptive step-size. We show that this strategy achieves near-optimal SINR coverage probability. We also highlight through simulations that sparse deployments require sub-6GHz band service for guaranteeing SINR requirements, whereas, in case of dense deployments, mm-wave may provide good SINR coverage, but with limited macrocell offloading. However, we show that, with large macrocell offloading, users at the edge of small cells, even in relatively dense deployments, need sub-6GHz band service to receive appreciable SINR coverage.
- **Cell Load Characterization and Load Balancing:** Next, we analyze the effect of traffic density on the downlink user throughput by using a M/G/1/PS queue model. The existing literature in stochastic geometry defines the cell load as the average number of associated full buffer users, uniformly distributed over the cell area, see e.g., [53, 75]. This approach is static in nature and ignores the effect of dynamic traffic on the user distribution: users with low data rate tend indeed to stay longer in the system so that the user distribution becomes inhomogeneous in space. To account for this effect, we rely on results from queuing theory [74] and characterize the load of each cell by the mean cell approximation [57]. We solve a fixed point equation for the load to take the load of the interfering base stations into account. Accordingly, we derive upper bounds on the probability for a cell in each tier and RAT to become overloaded. Based on the derived bounds, we provide values of minimum necessary deployment densities required for a given traffic density so as to limit overloading and outage. We then derive and optimize the downlink user throughput with respect to tier and RAT biases under these constraints. We analyze the fundamental trade-off between user throughput, overloading and outage

TABLE 2.1: Notations and System Parameters

Notation	Parameter	Value
ϕ_M, λ_M	MBS process and density	$\lambda_M = 5$ per sq. km.
ϕ_S, λ_S	SBS process and density	$\lambda_S = 5$ -200 per sq. km.
P_M, P_S	MBS/SBS power	46 dBm, 30 dBm
$\alpha_{tLr}, \alpha_{tNr}$	Approximated LOS/non line-of-sight (NLOS) path-loss exponents	2, 4
G_0	Maximum directivity gain with mm-wave antenna	36 dB
N_0	Noise power density	-174 dBm/Hz
B_μ, B_{mm}	Sub-6GHz/mm-wave bandwidth	20 MHz, 1 GHz
$\sigma_{N,mm}^2, \sigma_{N,\mu}^2$	Noise power	$N_0 B_{mm}, N_0 B_\mu$
d_M, d_S	MBS/SBS LOS ball radius	200 m, 20 m
θ	Beamwidth	15 degrees

probabilities. We finally highlight that the capability of the small cells to operate also in the sub-6GHz band plays a key role to restrict outage, thereby justifying our system model.

The rest of the chapter is organized as follows. In Section 2.2, we introduce our two-tier heterogeneous network model. In Section 2.3.2, we describe the proposed tier and RAT selection procedure and we derive the related association probabilities. Then, in Section 2.4, we compute and optimize the network downlink SINR distribution in terms of the tier and RAT selection biases. In Section 2.5, we characterize the load of the network and the downlink user throughput under a dynamic traffic model, and, hence, we design the load balancing such that the user performance is maximized. Simulation results are provided in Section 2.6. Finally, the chapter concludes in Section 4.5. Main notations used in this chapter are shown in Table 2.1.

2.2 System Model

2.2.1 Two-Tier Network Model

Consider a two-tier network consisting of macro BSs referred to as MBSs, and small cell BSs referred to as SBSs. MBSs are deployed to guarantee continuous coverage to the users. On the contrary, multi-RAT SBSs locally provide high data rate by jointly exploiting sub-6GHz and mm-wave bands. We also assume that the same sub-6GHz band is shared by MBSs and SBSs. Therefore, users receiving services on this band experience both co-tier and cross-tier interference. MBS and SBS locations are modeled as independent Poisson point processes (PPP), ϕ_M and ϕ_S , with intensities λ_M and λ_S , respectively. Let the transmit power of MBS be given by P_M ; the small cell transmit power, in both the bands, is assumed to be equal to P_S . End users are assumed to be distributed according to a PPP ϕ_U , independent of both ϕ_M and ϕ_S . Due to the independence of

the PPPs and Slivnyak's theorem [53], without loss of generality, we carry out our downlink analysis considering a typical user located at the origin.

2.2.2 Blockage Processes

Cellular networks generally suffer from link blockages due to buildings, vehicles, etc. We assume a blockage process independent of the BS processes. Let the probability of a MBS and SBS to be in LOS with respect to the typical user at a distance r , be denoted by $p_M(r)$ and $p_S(r)$, respectively. For a given SBS, the LOS probability in sub-6GHz is assumed to be the same as that in mm-wave. This is because, the probability of a signal to be blocked mainly depends on the blockage process, which is independent of the carrier frequency [76]. Due to the blockages, MBSs and SBSs can be categorized into either LOS or NLOS processes: ϕ_{ML} , ϕ_{MN} , ϕ_{SL} , and ϕ_{SN} , respectively. The intensity of these modified processes are given by $p_M(r)\lambda_M$, $(1 - p_M(r))\lambda_M$, $p_S(r)\lambda_S$, and $(1 - p_S(r))\lambda_S$, respectively. In our work, we use the LOS ball approximation introduced in [69]. Accordingly, let d_M be the MBS LOS ball radius. The probability of the typical user to be in LOS from a MBS at a distance r is $p_M(r) = 1$, if $r < d_M$, and $p_M(r) = 0$, otherwise.¹ We assume a similar LOS ball for the SBS process with a different radius d_S .

2.2.3 Directional Beamforming in mm-wave

In case of mm-wave operations, the received powers take advantage of the directional antenna gain of the transmitter and the receiver. The user and the serving BS are assumed to be aligned, whereas the interfering BSs are randomly oriented with respect to the typical user. Here, we assume a tractable model, where the product of the transmitter and receiver antenna gains, G , takes on the values a_k with probabilities b_k as given in Table 1 of [69]. Let the maximum value of G be G_0 .

¹Note that the ball-based LOS probability model is not used in the literature for sub-6GHz frequencies. Instead, a model with LOS probability equal to 1 until a certain distance and then decreasing exponentially is preferred, see e.g., [77]. For simplicity and tractability reasons, we use here a step probability model following criterion 1 in [69] to make the connection between the two approaches.

2.2.4 Path-loss Processes

We assume a distance based path-loss model where the path-loss at a distance d_{tvr} from a transmitter is given by: $l_{tvr}(d) = K_{tvr}d_{tvr}^{-\alpha_{tvr}}$ for a BS of type tvr , i.e., characterized by tier t (MBS or SBS), visibility state v (LOS or NLOS), and RAT r (sub-6GHz or mm-wave). Parameters K_{tvr} and α_{tvr} are derived from 3GPP UMa model for sub-6GHz MBSs, Umi model for sub-6GHz SBSs [78], and Umi model for mm-wave data transmission in SBSs [36]. By assuming a fast fading that is Rayleigh distributed with variance equal to one, the average received power is thus given by $P_{tvr} = P_t K_{tvr} d_{tvr}^{-\alpha_{tvr}}$, where P_t is the transmit power of a BS of tier t .

With our values (see Table 2.1) of transmit powers, path-loss exponents, and LOS ball radii, we have $\frac{d_S^{\alpha_{SL\mu}}}{K_{SL\mu}P_S} \leq \frac{d_M^{\alpha_{ML\mu}}}{K_{ML\mu}P_M} \leq \frac{d_S^{\alpha_{SN\mu}}}{K_{SN\mu}P_S} \leq \frac{d_M^{\alpha_{MN\mu}}}{K_{MN\mu}P_M}$. The analysis in this chapter is done considering that this ordering does not change even when powers are biased². This assumption is reasonable considering that if a LOS BS exists and the tier bias is moderate, its biased received power is very likely to be greater than that of any NLOS BS. Accordingly, we analyze the performance of the network with tier-selection bias (Q_T) in the range: $1 \leq Q_T \leq \frac{d_S^{\alpha_{SN\mu}} K_{ML\mu} P_M}{d_M^{\alpha_{ML\mu}} K_{SN\mu} P_S} = Q_T^{max}$.

2.2.5 Dynamic Traffic Model

We consider a model in which users arrive in the system, download a file, and leave the system. Any new download by the same user is considered as a new user. The arrival process of the new users is Poisson distributed with an intensity λ [users \cdot s⁻¹ \cdot m⁻²] and these new users are uniformly distributed over the network area A . The average file size is σ [bits/user]. When there are n users simultaneously served by a base station, the available resources are equally shared between them in a Round Robin fashion. Accordingly, we define the traffic density w in the network as $w = \lambda \cdot \sigma$ [bits \cdot s⁻¹ \cdot m⁻²]. Note that, while the user arrivals are uniform in space, as the space-time process evolves, users farther from the serving base stations which are characterized by lower data rates stay longer in the system, resulting in an inhomogeneous distribution of active users in the network.

²This assumption of ordering is considered only for the sake of simplicity and practicality. Considering higher bias values marginally alters the theoretical developments by modifying integral bounds in association probabilities. From an engineering point of view, very high bias values also lead to unacceptable outage probabilities and thus are of little interest.

2.3 Cell Association Procedure

In this section, we propose a cell association scheme based on tier and RAT selection biases and we derive the corresponding association probabilities. We start below by a preliminary result.

2.3.1 Distribution of the Path-loss Process

To analyze the cell association, path-loss processes are reformulated as one dimensional processes, $\phi'_{tvr} = \{\xi_{tvr,i} : \xi_{tvr,i} = \frac{\|x_i\|^{\alpha_{tvr}}}{K_{tvr}P_t}, x_i \in \phi_{tv}\}$, $t \in \{M, S\}$, $v \in \{L, N\}$, $r \in \{\mu, m\}$. The processes ϕ'_{tvr} are non-homogeneous with intensities calculated as below.

Lemma 2. *The intensity measures of the LOS and NLOS path-loss processes, ϕ'_{tLr} and ϕ'_{tNr} are:*

$$\begin{aligned} \Lambda'_{tLr}(0, x) &= \begin{cases} \pi \lambda_t (K_{tvr} P_t)^{\frac{2}{\alpha_{tLr}}} x^{\frac{2}{\alpha_{tLr}}}, & x < \frac{d_t^{\alpha_{tLr}}}{K_{tvr} P_t} \\ \pi \lambda_t d_t^2, & x > \frac{d_t^{\alpha_{tLr}}}{K_{tvr} P_t} \end{cases}, \\ \Lambda'_{tNr}(0, x) &= \begin{cases} 0, & x < \frac{d_t^{\alpha_{tNr}}}{K_{tvr} P_t} \\ \pi \lambda_t ((K_{tvr} P_t x)^{\frac{2}{\alpha_{tNr}}} - d_t^2), & x > \frac{d_t^{\alpha_{tNr}}}{K_{tvr} P_t} \end{cases}. \end{aligned} \quad (2.1)$$

Proof. The derivation of the intensity measure is similar to that in [79]. \square

The related intensities are obtained by differentiating the intensity measures, and are given by:

$$\begin{aligned} \lambda'_{tLr}(x) &= \begin{cases} \frac{2\pi \lambda_t (K_{tvr} P_t)^{\frac{2}{\alpha_{tLr}}} x^{\frac{2}{\alpha_{tLr}} - 1}}{\alpha_{tLr}}, & x < \frac{d_M^{\alpha_{tLr}}}{K_{tvr} P_t} \\ 0, & x > \frac{d_t^{\alpha_{tLr}}}{K_{tvr} P_t} \end{cases} \\ \lambda'_{tNr}(x) &= \begin{cases} 0, & x < \frac{d_M^{\alpha_{tNr}}}{K_{tvr} P_t} \\ \frac{2\pi \lambda_t (K_{tvr} P_t)^{\frac{2}{\alpha_{tNr}}} x^{\frac{2}{\alpha_{tNr}} - 1}}{\alpha_{tNr}}, & x > \frac{d_t^{\alpha_{tNr}}}{K_{tvr} P_t} \end{cases}. \end{aligned} \quad (2.2)$$

Lemma 3. *The probability density function (PDF) of the first point of $\phi'_{tv\mu}$, which corresponds to strongest sub-6GHz BS, is:*

$$f_{\xi_{tv\mu 1}}(r) = e^{-\Lambda'_{tv\mu}(0,r)} \lambda'_{tv\mu}(r).$$

Proof. The pdf of the first point in $\phi'_{tv\mu}$ is computed as

$$\begin{aligned} f_{\xi_{tv\mu 1}}(r) &= \frac{d}{dr} [\mathbb{P}(\phi'_{tv\mu} \cap (0, r) = 0)] = \frac{d}{dr} [e^{-\Lambda'_{tv\mu}(0,r)}] \\ &= e^{-\Lambda'_{tv\mu}(0,r)} \lambda'_{tv\mu}(r), \end{aligned}$$

where $\Lambda'_{tv\mu}$ and $\lambda'_{tv\mu}$ are given by Eq. (2.1) and Eq. (2.2), respectively. \square

2.3.2 Tier and RAT Selection Scheme

For the cell association mechanism, we assume that BSs send their control signals in the sub-6GHz band. This is due to the fact that sub-6GHz communication benefits from a higher reliability and better coverage than mm-wave signals [80]. Our scheme is based on two biases Q_T and Q_R for selecting the tier and the RAT respectively, to which the user will be associated. Parameter Q_T is the classical cell range expansion parameter [70]: a user compares the strongest MBS signal with the strongest *biased* SBS signal. By varying Q_T , we are able to offload users from MBSs to SBSs. Once associated to a SBS, in our approach, a user compares the sub-6GHz received signal with the mm-wave signal strength *biased* with a second parameter Q_R . By varying Q_R , users can be distributed between RATs of the same SBS³. The association policy, summarized in Algorithm 1, consists of two steps: tier selection and RAT selection.

2.3.3 Tier Selection

The tier selection is based on the transmitted signal on the sub-6GHz band. As a result, a user can be served either by: 1. an MBS in LOS (ML), 2. an MBS in NLOS (MN), 3. an SBS in LOS (SL), or 4. an SBS in NLOS (SN). Each of these tiers form separate PPPs. The biased received powers in sub-6GHz from the strongest LOS MBS, NLOS MBS, LOS SBS, and NLOS SBS are denoted as $P_{ML\mu 1}$, $P_{MN\mu 1}$, $Q_T P_{SL\mu 1}$, and $Q_T P_{SN\mu 1}$, respectively. User association is only based on measured biased received power. With the ordering assumption of Section 2.2.4, however, a user associates with an NLOS BS only in absence of an LOS BS. It must be noted that the user does not know the visibility state of

³An alternative association scheme could be realized through the control of the SBS power in the different bands. However, as the transmit powers of SBSs are generally limited, we do not take this into consideration. Moreover, our approach can be easily adapted to study this alternative scheme.

Algorithm 1: Tier and RAT Selection

```

1: Measure downlink sub-6GHz received powers from all MBS, SBS.
2: Let  $P_{Mv\mu 1}$  and  $P_{Sv\mu 1}$  be the strongest powers received from an MBS and an SBS,
   respectively.
3: if  $P_{Mv\mu 1} \geq Q_T P_{Sv\mu 1}$  then
4:   Associate to the strongest MBS
5: else
6:   Associate to the strongest SBS
7:   Measure the mm-wave received power from the SBS ( $P_{Svm1}$ ).
8:   if  $P_{Sv\mu 1} \geq Q_R P_{Svm1}$  then
9:     Start service from SBS in sub-6GHz band.
10:  else
11:    Start service from SBS in mm-wave band.
12:  end if
13: end if

```

the base stations and associates only according to the biased received powers. The result that the user associates with an NLOS BS only in the absence of a LOS BS follows from the ordering described in Section 2.2.4, which in turn, is a result of the values of the transmit powers and LOS ball radii. As a consequence, for a LOS BS, the association probability of a typical user with tier t can be calculated as:

$$\mathbb{P}_{tL} = \mathbb{E}[\mathbf{1}(tL)] \cdot \mathbb{E}[\mathbf{1}(t'L)] \cdot \mathbb{P}(\tilde{Q}_T P_{tL\mu 1} > \tilde{Q}_{T'} P_{t'L\mu 1}) + \mathbb{E}[\mathbf{1}(tL)] \cdot (1 - \mathbb{E}[\mathbf{1}(t'L)]), \quad (2.3)$$

where $t, t' \in \{M, S\}$, $t \neq t'$, and $\mathbf{1}(\cdot)$ is an indicator function: $\mathbf{1}(tL) = 1$ if and only if a point of tier t with visibility state L exists. The value of \tilde{Q}_T is equal to 1 if $t = M$, else it is equal to Q_T . The first term of Eq. (2.3) is the product of the probabilities of 1) the existence of a LOS SBS and 2) the existence of a LOS MBS and 3) that the received power from the serving tier is greater than the one from the non-serving tier. The second term is the product of the probabilities of the existence of at least one LOS BS of the serving tier and the absence of a LOS BS of the non-serving tier. In the same way, for the NLOS BSs, we have:

$$\mathbb{P}_{tN} = (1 - \mathbb{E}[\mathbf{1}(t_M L)]) \cdot (1 - \mathbb{E}[\mathbf{1}(t_S L)]) \cdot \mathbb{P}(\tilde{Q}_T P_{tN\mu 1} > \tilde{Q}_{T'} P_{t'N\mu 1}). \quad (2.4)$$

From these observations, we can deduce the tier selection probabilities as follows.

Lemma 4. *The tier selection probabilities are:*

$$\mathbb{P}_{ML} = \exp(-\pi\lambda_M d_M^2) \cdot \exp(-\pi\lambda_S d_S^2) \cdot W_1 + \exp(-\pi\lambda_M d_M^2) \cdot (1 - \exp(-\pi\lambda_S d_S^2)),$$

$$\mathbb{P}_{MN} = (1 - \exp(-\pi\lambda_M d_M^2)) \cdot (1 - \exp(-\pi\lambda_S d_S^2)) \cdot W_2,$$

$$\mathbb{P}_{SL} = \exp(-\pi\lambda_M d_M^2) \cdot \exp(-\pi\lambda_S d_S^2) \cdot (1 - W_1) + \exp(-\pi\lambda_S d_S^2) \cdot (1 - \exp(-\pi\lambda_M d_M^2)),$$

$$\mathbb{P}_{SN} = (1 - \exp(-\pi\lambda_M d_M^2)) \cdot (1 - \exp(-\pi\lambda_S d_S^2)) \cdot (1 - W_2),$$

where,

$$W_1 = \frac{(1 - e^{-(K_1+1)t_1})}{1 + K_1} + \exp(-\pi\lambda_S d_S^2) \cdot \left[\exp\left(-\Lambda'_{ML\mu}\left(0, \frac{d_S^{\alpha_{SL\mu}}}{Q_T K_{SL\mu} P_S}\right)\right) - \exp(-\pi\lambda_M d_M^2) \right],$$

$$W_2 = \exp(-\pi\lambda_S d_S^2) \frac{e^{-(K_2+1)t_2}}{1 + K_2},$$

$$K_1 = \pi\lambda_S \left(\frac{K_{SL\mu} P_S Q_T}{K_{ML\mu} P_M}\right)^{\frac{2}{\alpha_{SL\mu}}} (\pi\lambda_M)^{-\frac{\alpha_{ML\mu}}{\alpha_{SL\mu}}},$$

$$t_1 = \pi\lambda_M (K_{ML\mu} P_M)^{\frac{2}{\alpha_{ML\mu}}} \left(\frac{d_S^{\alpha_{SL\mu}}}{Q_T K_{SL\mu} P_S}\right)^{\frac{2}{\alpha_{ML\mu}}},$$

$$K_2 = \pi\lambda_S \left(\frac{K_{SN\mu} P_S Q_T}{K_{MN\mu} P_M}\right)^{\frac{2}{\alpha_{SN\mu}}} (\pi\lambda_M)^{-\frac{\alpha_{MN\mu}}{\alpha_{SN\mu}}}, \text{ and } t_2 = \pi\lambda_M d_M^2 (K_{MN\mu} P_M)^{\frac{2}{\alpha_{MN\mu}} - 1}.$$

Proof. See Appendix A.1. □

Lemma 5. *Given that a user is associated to a tier t of visibility state v , the pdf of the point in the 1D process of the serving BS is given by:*

$$\hat{f}_{\xi_{tv\mu 1}}(x) = \frac{f_{\xi_{tv\mu 1}}(x)}{\mathbb{P}_{tv}} \prod_{\forall (t'v' \neq tv)} \mathbb{P}(\phi'_{t'v'} \cap (0, x) = 0), \quad (2.5)$$

where $f_{\xi_{tv\mu 1}}(x)$ is given by Lemma 3.

Proof. The proof follows from Lemma 3 above and Lemma 3 of [69]. □

2.3.4 RAT Selection in SBS

A dual-band user, associated with an SBS, is served using mm-wave if and only if the biased estimated power in the mm-wave band is larger than the power received in the sub-6GHz band.

Lemma 6. *Given that a user is associated with a SBS of visibility state v , the sub-6GHz and mm-wave RAT selection probabilities are respectively given by:*

$$\mathbb{P}_{v\mu} = \exp\left(-\pi\lambda_S \left(\frac{K_{Svm}G_0Q_R}{K_{Sv\mu}}\right)^{\frac{2}{\alpha_{Svm}-\alpha_{Sv\mu}}}\right) \quad (2.6)$$

$$\mathbb{P}_{vm} = 1 - \mathbb{P}_{v\mu}. \quad (2.7)$$

Proof. See Appendix A.2. □

We denote $\mathbb{P}_{tvr} \triangleq \mathbb{P}_{tv}\mathbb{P}_{vr}$ as the association probability to a BS of type tvr with the convention that when $t = M$, $\mathbb{P}_{v\mu} = 1 - \mathbb{P}_{vm} = 1$.

2.3.5 Comparison to a One-Step Association Strategy

It must be noted that our proposed two-step association scheme is different from a more natural and exhaustive scheme (e.g., [73]), which directly compares the biased received powers from all the tiers and RATs (i.e., one-step procedure). In this regard, our two-step association procedure suffers from some sub-optimality with respect to the biased received power. However, access delay is lower with our strategy because the users position and orientation can be acquired in the sub-6GHz band before performing beamtraining.

First, we show that both the one-step strategy and our approach result in the same RAT selection, given that the user associates with the small cell tier. Then, our strategy differs from the one-step strategy when a user associates to an MBS while the biased power received from an SBS in mm-wave is higher than the biased power received from the MBS. We characterize hereafter the probability of this event.

Proposition 1. *If the typical user receives a higher sub-6GHz received power from an SBS S_1 as compared to an SBS S_2 , then it also receives higher mm-wave power from S_1 than from S_2 . Moreover, the tier selection and RAT selections biases Q_T and Q_R , do not impact this ordering of received powers.*

Proof. See Appendix A.4. □

From Proposition 1, we conclude that it is not possible for the typical user to have a higher received power in sub-6GHz band from SBS S_1 as compared to S_2 and lower mm-wave power from the same. Thus, the two schemes result in the same RAT selection, in case the user associates with the SBS tier. Therefore, the only difference in association arises when the biased received power from the

strongest SBS (denoted S_1) in sub-6GHz band is less than that received from the strongest MBS (denoted by M_1), while simultaneously, the biased received power from S_1 in mm-wave is higher than the biased received power from M_1 . Let us call these events E_1 and E_2 , respectively. This results in sub-optimal association of some users in the sense that these users are not associated to the tier-RAT pair providing the highest biased power. We have the following result to model this sub-optimal association.

Lemma 7. *The probability of suboptimal association in case of an association with LOS MBS instead of mm-wave LOS SBS is given as:*

$$\mathbb{P}_{SO} = 2\pi\lambda_M \frac{1 - \exp(-\pi(\lambda_S\zeta_2 - 2\lambda_S\zeta_1 + \lambda_M)d_M^2)}{2\zeta_2}, \quad (2.8)$$

where $\zeta_1 = \frac{P_S Q_T}{P_M}$ and $\zeta_2 = \frac{K_m P_S Q_R Q_T}{K_\mu P_M}$

Proof. See Appendix A.5. □

In Section 2.6, we provide numerical results to show that the sub-optimality is limited, and this loss can be compensated by a faster access procedure, which may increase the network throughput.

2.3.6 A Simple Strategy to Prioritize mm-wave RAT

Depending on the network load and the active services, the mobile operator may want to prioritize one RAT over the other. For instance, the utilization of mm-wave frequencies for latency sensitive applications, can be an attractive strategy to offload the sub-6GHz band, which can mainly be dedicated to communications requiring reliability and continuous service. In the following, we propose a strategy to achieve this goal. For that, we introduce the following definition:

Definition 1. *The critical distance with respect to the typical user is the distance of the SBS from which the typical user receives equal mm-wave and sub-6GHz power.*

For our system model, the critical distance for the LOS SBS tier can be expressed as:

$$d_{CL} = \left(\frac{K_{SLm}}{K_{SL\mu}} G_0 \right)^{\frac{1}{\alpha_{SLm} - \alpha_{SL\mu}}} \quad (2.9)$$

Proposition 2. *If there exists exactly one point of the LOS SBS process within the critical distance, the typical user always selects mm-wave as serving RAT. Moreover, in this scenario, this is the optimal strategy in terms of SINR for the typical user.*

Proof. In the case where this condition holds, the useful signal received in mm-wave is greater than that received in sub-6GHz (as per definition of d_{CL}). Thus, the typical user always selects the mm-wave RAT from the serving SBS. Moreover, as all interfering LOS SBS are outside d_{CL} , the sub-6GHz interference has state-wise dominance with respect to the mm-wave interference. Hence, the mm-wave SINR is always larger than the sub-6GHz SINR. \square

From Eq. (2.9), we see that, for given path-loss exponent values of each user, the critical distance can be controlled by varying the product of the transmitter and receiver antenna gain G_0 . This enables the users served by LOS SBSs to adjust their antenna gain in order to select mm-wave communications, and ensure that this choice is optimal from the SINR perspective. In addition, given a fixed antenna gain G_0 , we have the following corollary, which provides the deployment density of SBSs that maximizes the probability of occurrence of a single LOS SBS within the critical distance.

Corollary 1. *The maximum probability of occurrence of exactly one point of LOS SBS within the critical distance is $1/e$, and this occurs at:*

$$\lambda_S = \frac{1}{\pi} \left(\frac{K_{Sv\mu}}{K_{Sv\mu}} G_0 \right)^{\frac{2}{\alpha_{SL\mu} - \alpha_{SLm}}}.$$

Proof. The probability of existence of only one point within the critical distance is calculated as:

$\mathbb{P}(\phi'_{SL} \cap b(0, d_{CL}) = 1) = \pi \lambda_S d_{CL}^2 \exp(-\pi \lambda_S d_{CL}^2)$, where $b(0, d_{CL})$ is the ball of radius d_{CL} centered at the origin. The maximum value of this probability occurs at $\pi \lambda_S d_{CL}^2 = 1$, then substituting the value of d_{CL} from Eq. (2.9) completes the proof. \square

2.4 Downlink SINR Distribution

In this section, we first derive the downlink SINR coverage probability for the maximum biased received power association policy and then optimize the biases with respect to the cell coverage.

2.4.1 SINR Coverage Probability

The SINR coverage probability at a threshold γ , can be expressed as $\mathbb{P}_C(\gamma) = \mathbb{P}(\text{SINR} > \gamma)$. Following the theorem of total probabilities, we have:

$$\mathbb{P}_C(\gamma) = \sum_{t \in \{M, S\}, v \in \{L, N\}, r \in \{\mu, m\}} \mathbb{P}(\text{SINR}_{t,v,r} > \gamma | t, v, r) \mathbb{P}_{tvr}, \quad (2.10)$$

We divide the problem of finding the overall coverage probability into two parts: the one related to the sub-6GHz service and the one associated with the mm-wave service, and we compute the coverage probability by relying on 1D processes ϕ'_{tvr} .

Lemma 8. *The conditional SINR coverage probability, given that the user is associated with a sub-6GHz BS of tier t and visibility state v , is given by:*

$$\mathbb{P}_{C_{tv\mu}}(\gamma) = \int_0^\infty \exp\left(-\gamma \cdot \sigma_{N,\mu}^2 \cdot x - \sum_{t',v'} A_{t'v'}(\gamma, x)\right) \hat{f}_{\xi_{tv\mu 1}}(x) dx, \quad (2.11)$$

where,

$$A_{t'v'} = \int_{l_{t'}}^\infty \frac{\gamma x}{y + \gamma x} \Lambda'_{t'v'\mu}(dy), \quad \forall t' \in \{M, S\}, v' \in \{L, N\}.$$

Additionally, $l_{t'} = x$ if $t' = t$, $l_{t'} = Q_T \cdot x$, when $t = M$ and $t' = S$, and $l_{t'} = x/Q_T$, when $t = S$ and $t' = M$.

Proof. See Appendix A.3. □

Lemma 9. *The conditional SINR coverage probability, given that the user is associated with a SBS in mm-wave of visibility state v , is given by:*

$$\mathbb{P}_{C_{Svm}}(\gamma) = \int_0^\infty \exp\left(-\frac{\gamma \cdot x \cdot \sigma_{N,mm}^2}{G_0} - B_1(\gamma, x) - B_2(\gamma, x)\right) \hat{f}_{\xi_{Svm 1}}(x) dx, \quad (2.12)$$

$$\text{with } B_1(\gamma, x) = \sum_{k=1}^4 \left(-b_k \int_x^\infty \left(\frac{a_k \gamma x}{y + a_k \gamma x} \Lambda'_{Svm}(dy) \right) \right),$$

$$\text{and, } B_2(\gamma, x) = \sum_{k=1}^4 \left(-b_k \int_x^\infty \left(\frac{a_k \gamma x}{y + a_k \gamma x} \Lambda'_{Sv'm}(dy) \right) \right).$$

Proof. The proof follows in a similar way to that of Lemma 7. □

2.4.2 A Near-Optimal Strategy for Bias Selection

On the one hand, obtaining optimal biases with respect to the SINR coverage probability is difficult because of the complex expressions. On the other hand, using brute force to search through all the possible pairs of tier and RAT selection biases can have a very high time-complexity which limits practical implementation. Accordingly, in this section, we propose a strategy to select the tier and RAT selection biases with the aim of maximizing the SINR coverage.

Specifically, the proposed strategy is based in two parts: 1) computing the RAT selection bias, Q_R and 2) obtaining the tier selection bias Q_T based on a random-restart hill-climbing algorithm.

Heuristic for Selection of Q_R

The heuristic to set the RAT selection bias Q_R consists of computing the ratio of the mean signal to interference and noise perceived by the typical user on the sub-6GHz and mm-wave bands. That is:

$$Q_R = \frac{\mathbb{E} \left[\frac{S_{mm}}{I_{mm} + \sigma_{N,mm}^2} \right]}{\mathbb{E} \left[\frac{S_{\mu}}{I_{\mu} + \sigma_{N,\mu}^2} \right]}, \quad (2.13)$$

where I_{μ} and I_{mm} , respectively, are the sum of the interference from all the (LOS and NLOS) BSs in sub-6GHz and mm-wave, respectively. It must be noted that evaluating the above expression without the knowledge of the coverage probability is not possible. However, with a relaxation of independence of the useful signal and the interference for each of the RATs, the expected values can be approximated using the results of [81]. Once Q_R is computed, Q_T can be obtained by the following step

Random-Restart Hill-Climbing Algorithm for Selection of Q_T

We start with a random value of Q_T , i.e., Q_T^0 and calculate the gradient of \mathbb{P}_C at Q_T^0 . In case the gradient is non-negative, we increase the value of Q_T by a step size of k . If the gradient is negative, we decrease the value of Q_T by the same step size k . We continue this procedure with the updated value of Q_T until the variation in Q_T is sufficiently small. In the case where the product of two consecutive values of the gradient is non-positive, and as a result we cross a stationary point, we reduce the step size by a factor β and continue the algorithm.

In our algorithm, Q_T^{max} is the maximum value of the bias in the moderate range. If the coverage probability is monotonic, quasi-convex or quasi-concave, this procedure provides the optimal value of Q_T . In the general case, the procedure stops at a local maximum in the range $1 \leq Q_T \leq Q_T^{max}$. This local maximum can be improved by repeatedly starting the same algorithm with random starting points. This procedure to obtain Q_T is summarized in Algorithm 2. In Section VI, we compare the performance of this proposed scheme with the optimal case.

Algorithm 2: Random-restart hill-climbing algorithm with Adaptive Step-Size

```

1: Set  $t = 1$ ,  $k > 0$ ,  $\epsilon > 0$  and  $\beta > 1$ .
2: Set  $Q_T(0) = Q_T^0$ .
3: while  $|Q_T(t) - Q_T(t-1)| > \epsilon$  do
4:   if  $\frac{dP_C}{dQ_T}(Q_T(t)) > 0$  then
5:      $Q_T(t) = \min\{Q_T(t-1) + k, Q_T^{max}\}$ .
6:   else
7:      $Q_T(t) = \max\{Q_T(t-1) - k, 1\}$ .
8:   end if
9:   if  $\frac{dP_C}{dQ_T}(Q_T(t)) \cdot \frac{dP_C}{dQ_T}(Q_T(t-1)) < 0$  then
10:     $k \leftarrow \frac{k}{\beta}$ .
11:   end if
12:    $t \leftarrow t + 1$ 
13: end while

```

2.5 Cell Load, User Throughput, and Load Balancing

In the previous section we have focused only on coverage aspects, we now take into account cell loads to show how tier and RAT selection biases can improve the user average throughput. For this, we consider a multi-user system where the users share the available radio resources according to a round robin policy.

2.5.1 Cell Load Characterization

According to our model of the traffic arrival process, the traffic density is given as $w = \lambda \cdot \sigma$ [bits/s/m²]. For a single cell scenario, Bonald et al. [74] have modeled the load of the cell of area A as $\rho = \int_A \frac{w}{R(s)} ds$ [74], where $R(s)$ is the physical data rate of a user located at s . In case of Poisson-Voronoi cells, the average load is generally difficult to evaluate because of the randomness in the

shape and sizes of the cells. Furthermore, in a multi-cell scenario, the load of a cell depends on the SINR characteristics of the cell, which in turn, depends on the load of the other cells in the network.

We know from the ergodicity of the PPP, that the fraction of the BS of type tvr that are idle is equal to the fractional idle time of the typical BS of same type. Accordingly, assuming that the load of the typical BS of type tvr is given by $\bar{\rho}_{tvr}$, then, the fraction of idle BS of type tvr is given by $1 - \bar{\rho}_{tvr}$. We substitute this value $\forall t, v, r$ in the calculation of the load as:

$$\bar{\rho}_{tvr} = \int_{\gamma} \frac{wA_{tvr}}{B_r \log_2(1 + \gamma)} p_{tvr}(\bar{\rho}, \gamma) d\gamma, \quad (2.14)$$

where the pdf of the SINR $p_{tvr}(\bar{\rho}_{tvr}, \gamma)$ is a function of the average idle fraction of the BS and $\bar{\rho}$ is a vector of the fraction of idle BSs of all BS types, i.e., $\bar{\rho} = [\rho_{tvr}] \forall t, v, r$. This fixed point equation is then solved in an iterative manner to obtain the actual load of the BS of all the tiers (starting from zero load). Then, the SINR coverage probability with $1 - \bar{\rho}$ fraction of BSs idle, given that the user is associated with a sub-6GHz BS of tier t and visibility state v , is given by:

$$\mathbb{P}_{C_{tv\mu}}(\bar{\rho}, \gamma) = \int_0^{\infty} \exp\left(-\gamma \cdot \sigma_{N,\mu}^2 \cdot x - \sum_{t',v'} A_{t'v'}(\gamma, x, \rho_{t'v'\mu})\right) \hat{f}_{\xi_{tv\mu 1}}(x) dx, \quad (2.15)$$

where,

$$A_{t'v'}(\gamma, x, \rho_{t'v'\mu}) = \int_{l_{t'}}^{\infty} \frac{\gamma x}{y + \gamma x} \Lambda'_{t'v'\mu}(dy, \rho_{t'v'\mu}), \forall t' \in \{M, S\}, v' \in \{L, N\}.$$

Additionally, $l_{t'} = x$ if $t' = t$, $l_{t'} = Q_T \cdot x$, when $t = M$ and $t' = S$, and $l_{t'} = x/Q_T$, when $t = S$ and $t' = M$. The intensity measures Λ_{tvr} are obtained by modifying λ_t to $\lambda_t \rho_{tvr}$ for each BS type. The calculation for the mm-wave BS follows in the same way.

It should be noted that in case of a Poisson distributed network, there exists a non-zero fraction of unstable cells ($\rho \geq 1$), which cannot handle their load.

Lemma 10. *The probability of a typical cell of type tvr to be unstable is bounded as:*

$$\mathbb{P}(\rho_{tvr} \geq 1) \leq \min \left\{ \frac{\sigma_{tvr}^2}{(1 - \bar{\rho}_{tvr})^2}, \bar{\rho}_{tvr} \right\}, \quad (2.16)$$

where $\sigma_{tvr}^2 = \mathbb{E}[\rho_{tvr}^2] - \bar{\rho}_{tvr}^2$, is the variance of the load, which can also be calculated, similar to $\bar{\rho}_{tvr}$ by using the SINR coverage probability of the typical user.

Proof. We have for every $k > 0$,

$$\mathbb{P}[(\rho_{tvr} - \bar{\rho}_{tvr}) \geq k\sigma_{tvr}] \leq \mathbb{P}[|\rho_{tvr} - \bar{\rho}_{tvr}| \geq k\sigma_{tvr}] \stackrel{(a)}{\leq} \frac{1}{k^2},$$

where, (a) is from Chebyshev inequality. Substituting $k \cdot \sigma_{tvr} = 1 - \bar{\rho}_{tvr}$, we obtain the first term of the right hand side in (2.16). The second term is a direct result of Markov inequality. \square

2.5.2 Average User Throughput

The average downlink throughput that a user receives from a BS of type tvr is $T_{tvr} \triangleq \frac{wA_{tvr}}{N_{tvr}}$, where N_{tvr} is the average number of active users in a cell, which can be approximated by using the mean cell approach [57]. The mean cell is defined as a hypothetical cell that has the same average load as that of a typical cell.

Lemma 11. *The downlink average user's throughput in a non-overloaded mean cell of type tvr is:*

$$T_{tvr} = \lambda \cdot \sigma \frac{1 - \bar{\rho}_{tvr}}{\bar{\rho}_{tvr}} A_{tvr}.$$

Proof. The proof is similar to that presented in [74]. \square

The average user throughput is then given by theorem of total probability as: $T = \sum_{tvr} \mathbb{P}_{tvr} T_{tvr}$. Due to the different operating bandwidths, the bias values which provide the optimal user throughput may lead to weak SINR, which in turn increases the outage. Thus, to guarantee the communication reliability, it is necessary to consider an SINR constraint on the selection of the optimal biases. We define the outage probability with respect to a SINR threshold γ_{\min} as:

$$\mathbb{P}_{o,tvr}(\gamma_{\min}) = 1 - \mathbb{P}_{Ctvr}(\gamma_{\min}). \quad (2.17)$$

Therefore, we introduce the notion of effective throughput, which measures the throughput of the users, which are not in outage, as: $T_{eff}(\gamma_{\min}) = \sum_{tvr} \mathbb{P}_{tvr} \cdot T_{tvr} \cdot \mathbb{P}_{Ctvr}(\gamma_{\min})$. In Section 2.6, we optimize Q_T and Q_R so as to maximize the average effective user throughput $T_{eff}(\gamma_{\min})$ under the constraint of a maximum outage probability $\mathbb{P}_{o,tvr}(\gamma_{\min}) \leq \bar{\mathbb{P}}_o$ for every BS type tvr .

2.5.3 Delay-Throughput Trade-off of the One-Step Association Scheme.

It must be noted that the sub-optimality in biased received power does not always deteriorate the downlink user throughput, specially for larger access delays. To illustrate this, let us assume that the initial access using mm-wave suffers from a delay given by Δ . In this regard, the throughput for the users associated to the SBSs in mm-wave RAT is given by:

$$T_{Svm} = \frac{\sigma}{\frac{N_{Svm}}{\Lambda} + \Delta}, \quad (2.18)$$

where $\Lambda = \lambda \cdot A_{Svm}$ is the traffic arrival rate in terms of users per second in the mm-wave cell of visibility state v of coverage area $A_{Svm} = \frac{\mathbb{P}_{Svm}}{\lambda_S}$, $N_{Svm} = \frac{\bar{\rho}_{Svm}}{1 - \bar{\rho}_{Svm}}$ is the number of active users in the cell, and $\frac{N_{Svm}}{\Lambda}$ is the transmission time according to Little's theorem [82]. In Section VI, we provide some numerical results to show that in case of realistic access delay with the mm-wave RAT, our scheme performs better in terms of the downlink throughput.

2.6 Simulation Results

In this section, we first validate our path-loss exponent approximation with respect to 3GPP values. Then, we study the effects of biases on SINR and user throughput. Finally, we discuss the selection of optimal biases.

2.6.1 Validation of the Path-loss Exponent Approximation

Fig. 2.1 shows the comparison of our analytical results using the approximated path-loss exponents from Table I with Monte-Carlo simulations with actual path-loss exponents from the 3GPP recommendations [78, 36] in terms of SINR

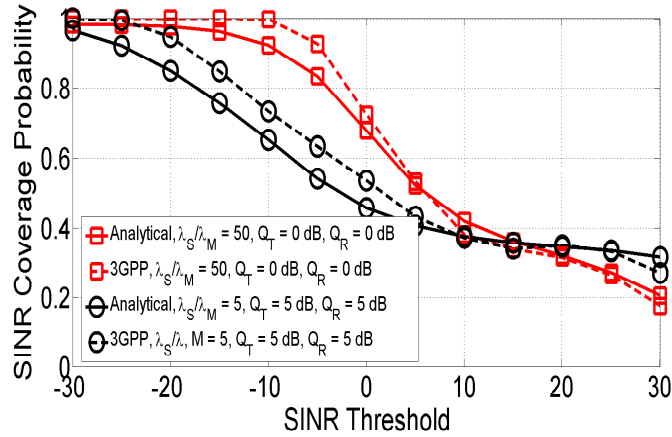


FIGURE 2.1: Validation of the approximated path-loss exponents with 3GPP parameters.

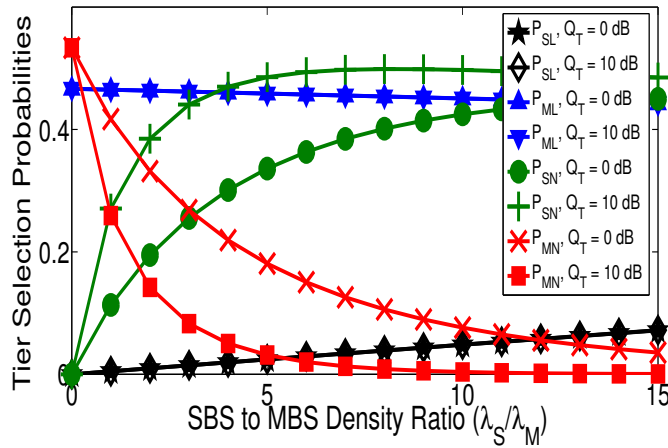


FIGURE 2.2: Tier selection probability

coverage probability for various tier, RAT selection biases, and density values. Our results indicate that the analytical expressions based on approximated path-loss exponents provide good approximations to the simulated results with 3GPP values of exponents. Hence, this approximation can be used for analyzing the system performance.

2.6.2 Trends in Cell Association Probabilities

Fig. 2.2 shows the tier selection probabilities with respect to the ratio of the MBS and SBS densities λ_S/λ_M with $Q_T = 10$ dB and with $Q_T = 0$ dB. As expected, the association to MBSs decreases as λ_S/λ_M increases or when Q_T increases. However, the association to LOS BSs does not change appreciably when increasing Q_T from 0 to 10 dB. Only cell edge users, which are more likely to be in NLOS visibility, are indeed affected by moderate values of Q_T .

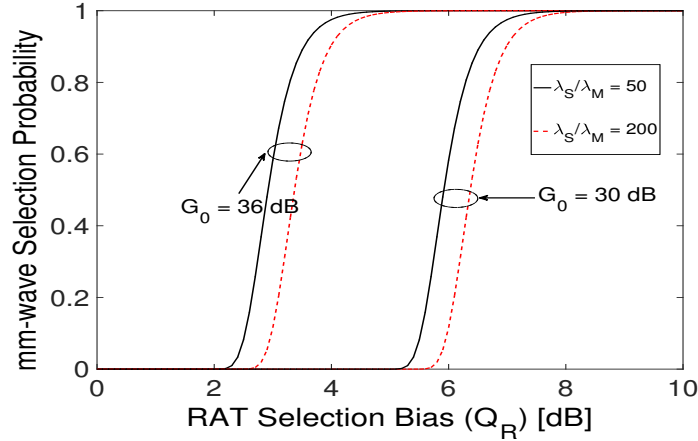


FIGURE 2.3: Conditional mm-wave RAT selection probability with 3GPP parameters.

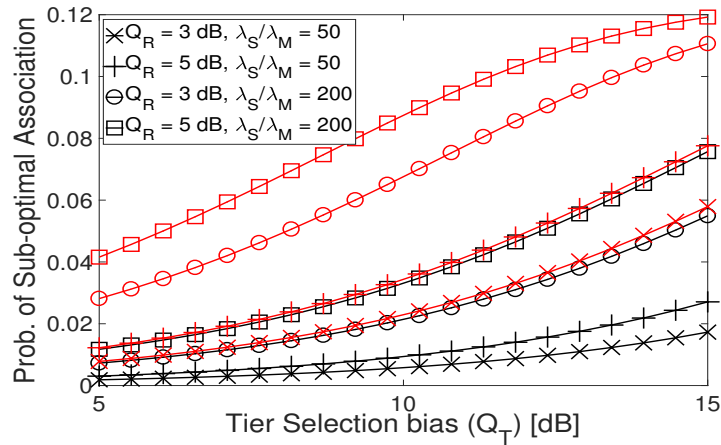


FIGURE 2.4: Probability of sub-optimal association for different Q_R and for different $\frac{\lambda_S}{\lambda_M}$. The black curves correspond to $G_0 = 30$ dB and the red curves correspond to $G_0 = 36$ dB;

The conditional probability of mm-wave service, given that the user has associated with a SBS, is plotted in Fig. 2.3, by varying Q_R for two different antenna gains and deployment density ratios. As expected, this probability increases with Q_R . However, it is interesting to note that the maximum directional antenna gain has a large effect on the RAT selection regardless of the SBS density. For example, increasing by only 3 dB the antenna gains of transmitter and receiver each has much more impact on the mm-wave association than deploying four times more SBSs.

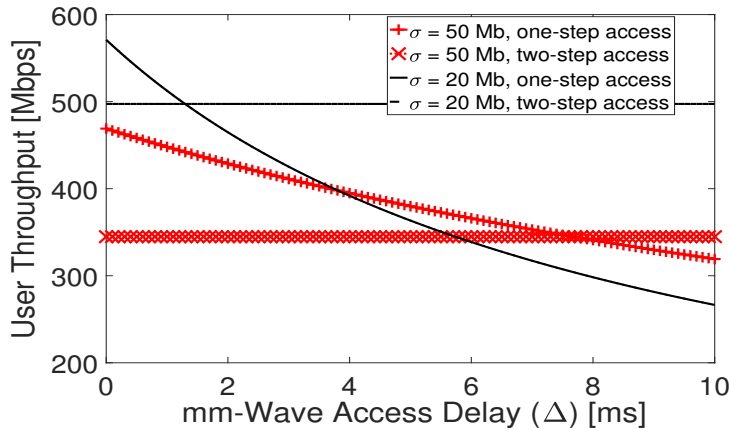


FIGURE 2.5: Delay-throughput trade-off with mm-wave initial access; $G_0 = 36$ dB, $Q_T = 10$ dB, $Q_R = 5$ dB, $\lambda = 100$ [user \cdot km $^{-2}$ s $^{-1}$].

2.6.3 Comparison with the One-Step Association Strategy:

We plot the probability of sub-optimal association (2.8) in the Figure 2.4, for various tier and RAT selection biases and two antenna gains. We note that the probability of sub-optimal association is low ($\leq 12\%$). Moreover, the probability becomes negligible with low tier selection bias ($\leq 1\%$). This is because with lower Q_T , the biased received power of the mm-wave transmission in SBS are lower, thereby reducing the probability of sub-optimality. Similarly, with lower antenna gain (G_0), the biased mm-wave power is lower, resulting in low sub-optimality. Furthermore, we observe that the probability of sub-optimal association increases with increasing network densification, since denser networks correspond to higher mm-wave powers. However, for $G_0 = 30$ dB, the probability of sub-optimal association does not exceed 8% even for very dense deployments.

In Figure 2.5, we compare the throughput perceived by the typical user with the two approaches (2.18). We plot the downlink user throughput vs the initial access delay Δ , for two different file sizes (σ). We see that with increasing Δ , the throughput with the one-step association scheme decreases, and goes below the throughput achieved by using our two-step solution. In practical systems, the initial access delay in mm-wave can be of the order of several milliseconds [41]. As a result, our two step association is more efficient in terms of the user throughput as compared to the case where association is performed in one-step.

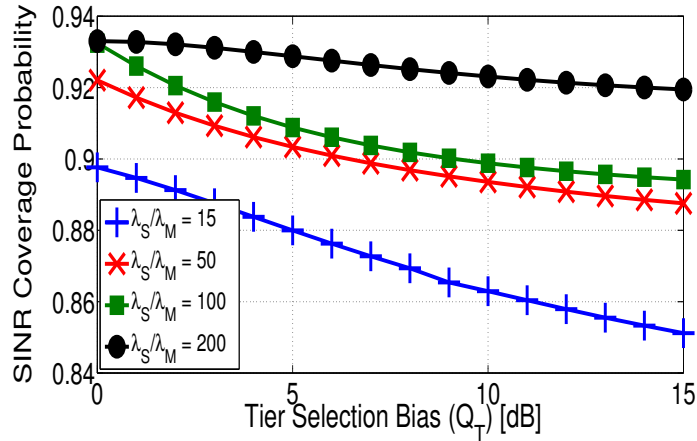


FIGURE 2.6: SINR coverage probability vs tier selection bias at a threshold of $\gamma = -10$ dB for $Q_R = -\infty$ dB;

2.6.4 Trends in SINR Coverage Probabilities

In Fig. 2.6 and 2.7, we plot the SINR coverage probability of the typical user, with respect to Q_T and various ratios of SBS to MBS densities. In the case where the SBSs operate only in sub-6GHz band, i.e., $Q_R = -\infty$ dB (Fig. 2.6), increasing the tier selection bias decreases the SINR coverage probability because some users are forced to associate with BSs providing less signal power. For $d_M = 200$ m and $d_S = 20$ m, Fig. 2.7 shows that the same effect can be observed when SBSs transmit data only in mm-wave, i.e., $Q_R = \infty$, regardless of the deployment densities.

However, in the latter case, when varying the blockage characteristics, we observe two different behaviors for the SINR coverage probability. In Fig. 2.8, we see that depending on the LOS ball radii, the SINR may increase with the tier selection bias. Indeed, the SINR may improve by associating macro cell users to SBSs transmitting data only in mm-wave, even though this SBS offers less power in sub-6GHz band, because the received power in mm-wave may be higher due to antenna gain. Additionally, the interference in mm-wave is generally lower than the one in the sub-6GHz band. However, increasing the bias further forces the users closer to the MBS to associate with a SBS that provide very limited received power, which leads to lower SINR.

Assuming maximum power tier selection ($Q_T = 0$ dB), Fig. 2.9 shows that increasing Q_R has contrasting effects on the SINR depending on the ratio of SBS to MBS densities. Increasing the SBS density increases co-channel interference more in sub-6GHz than in mm-wave. Moreover, as the user-SBS distance decreases, the useful signal power increases more in mm-wave than in sub-6GHz.

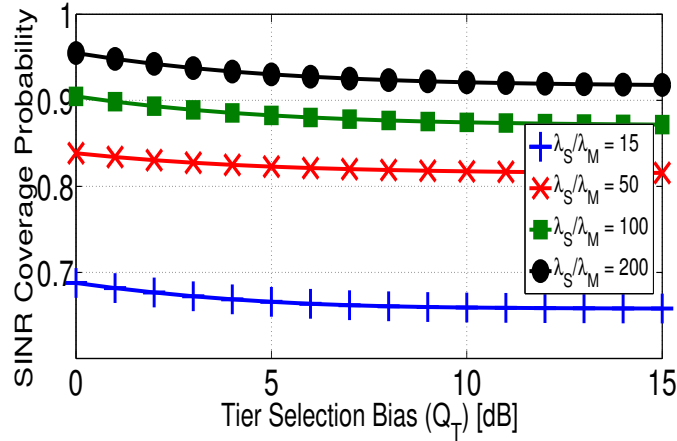


FIGURE 2.7: SINR coverage probability vs tier selection bias at a threshold of $\gamma = -10$ dB for $Q_R = \infty$, $d_M = 200$ m, $d_S = 20$ m.

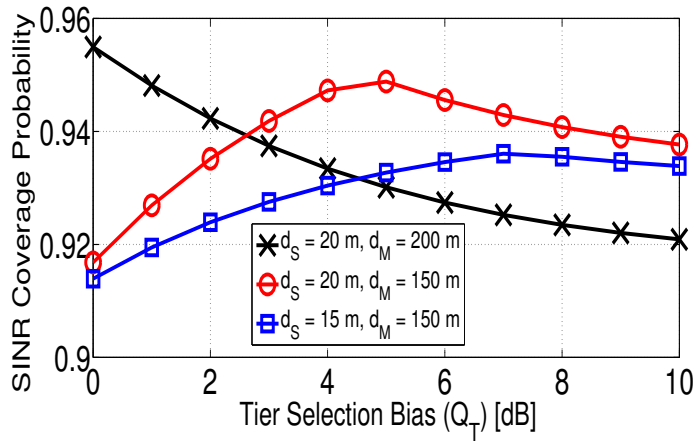


FIGURE 2.8: SINR coverage probability with different LOS radii for $Q_R = \infty$, $\lambda_S/\lambda_M = 200$

Both effects are due to the difference in the path-loss models. As a consequence, as the SBS density increases ($\lambda_S/\lambda_M = 200$), it is more and more attractive for a user to be served by mm-wave band, which is realized by higher values of Q_R . On the contrary, in case of sparser SBS deployments ($\lambda_S/\lambda_M = 15, 50, 100$), increasing Q_R forces users to be served from distant SBSs in mm-wave, and the gain due to the reduced interference cannot compensate the signal strength loss. Note that this contrasting effect cannot be observed with single RAT networks.

We now study the joint effect of Q_T and Q_R for dense ($\lambda_S/\lambda_M = 200$) and sparse ($\lambda_S/\lambda_M = 50$) deployments in Fig. 2.10 and 2.11, respectively. For sparse SBS deployments, the conclusions drawn so far hold: high SINR regions occur at low Q_T and Q_R . The optimum biases as marked in the figure are $Q_T = 0$ dB and $Q_R = 0$ dB. For dense deployments, however, we can observe that, for a high Q_T (here for $Q_T > 8$ dB), SINR coverage probability generally decreases

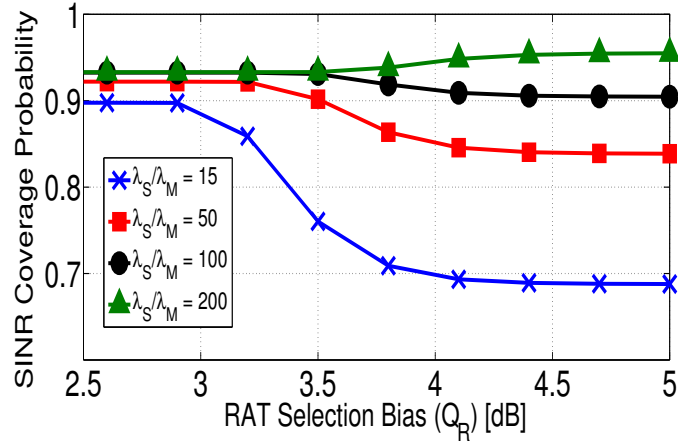


FIGURE 2.9: SINR coverage probability vs RAT selection bias with $Q_T = 0$ dB.

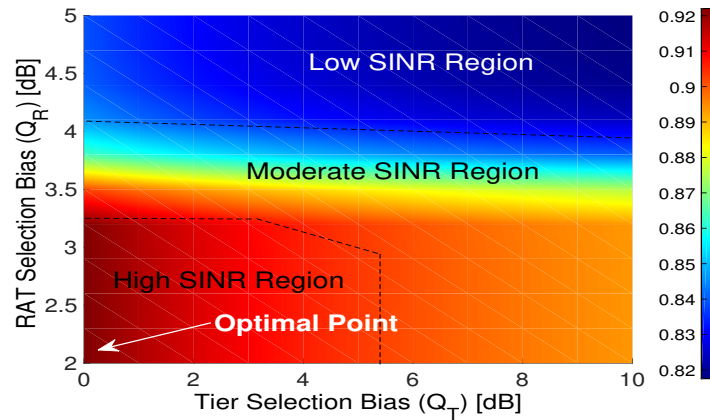


FIGURE 2.10: SINR coverage probability as a function of Q_T and Q_R at a threshold of $\gamma = -10$ dB for $d_M = 200$ m, $d_S = 20$ m for $\lambda_S/\lambda_M = 50$.

with increasing Q_R , which is in contrast to the case when Q_T is small. This is because, for users far away from their serving SBS, it is now preferable to get associated with sub-6GHz than with mm-wave. The optimal biases in this case are $Q_T = 0$ dB and $Q_R = 5$ dB.

2.6.5 Performance of the Near-Optimal Strategy to Select Tier and RAT Biases

In Section 2.4.2, we have proposed a near-optimal strategy to fix the RAT and tier-selection bias, to reduce the complexity of the brute force search. In this strategy, first Q_R is selected according to (2.13). Then, for the fixed Q_R , a Q_T is selected according a random-restart hill-climbing algorithm as described

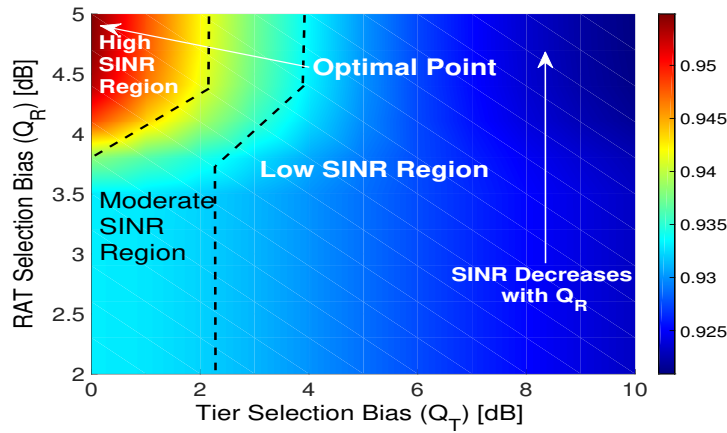


FIGURE 2.11: SINR coverage probability as a function of Q_T and Q_R at a threshold of $\gamma = -10$ dB for $d_M = 200$ m, $d_S = 20$ m for $\lambda_S/\lambda_M = 200$.

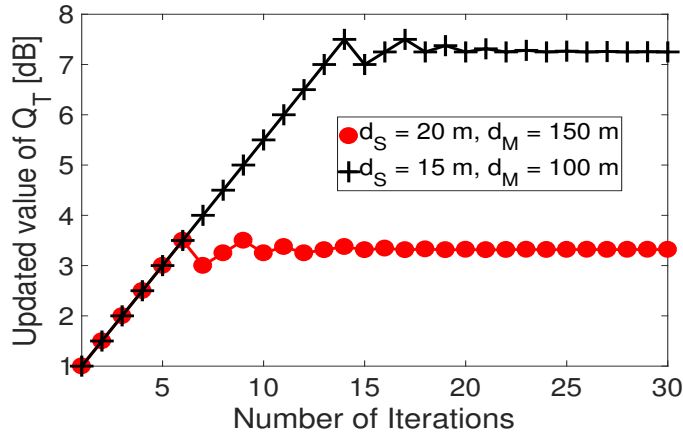


FIGURE 2.12: Convergence of gradient descent algorithm for $\lambda_S/\lambda_M = 100$, $d_S = 10$ m and $d_M = 100$ m

in Algorithm 2. We show the convergence of the algorithm in Fig. 2.12 for $\lambda_S/\lambda_M = 200$ and for two pairs of LOS radii. With $k = 0.5$ and $\beta = 2$, the proposed algorithm converges at $Q_T = 3.19$ dB for $d_S = 20$ m and $d_M = 150$ m, and at $Q_T = 7.16$ dB for $d_S = 15$ m and $d_M = 100$ m. Fig. 2.13 compares various bias selection strategies. We observe that our proposed strategy performs at least as good as the classical strategy based on the maximum received power. In particular, for sparse deployment of SBSs, the proposed strategy and the maximum power association perform equal to the optimal association. However, with increasing SBS density, the performance of the maximum power association decreases due to the increasing interference in the sub-6GHz RAT. On the contrary, since our strategy takes interference into account, it achieves near optimal SINR.

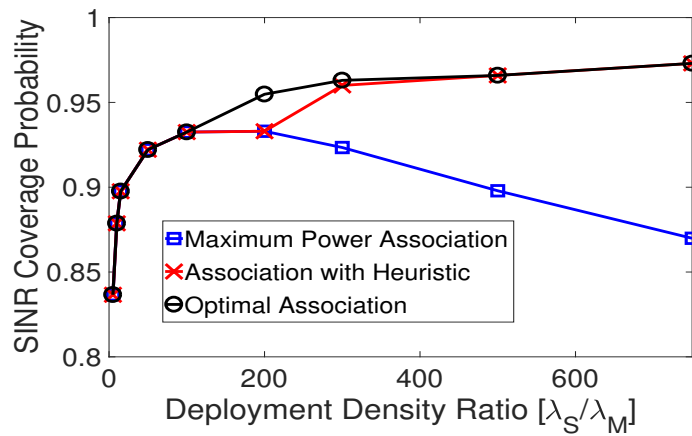


FIGURE 2.13: Comparison of RAT selection strategies

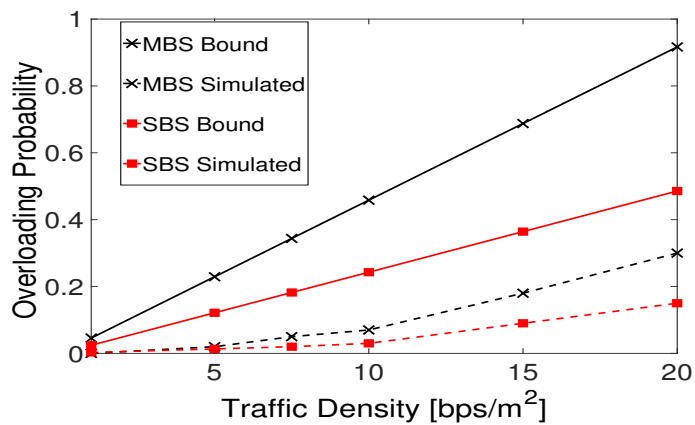


FIGURE 2.14: Tightness of the bound on probability of overloading.

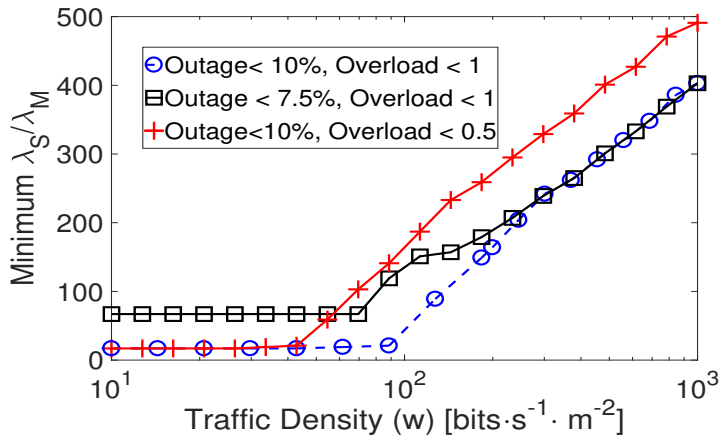


FIGURE 2.15: Minimum required deployment density for a given traffic density

2.6.6 Analysis of the Bound on Overloading Probabilities

In this section, we investigate the relation between the cell overloading probabilities and the traffic density, based on the analytical bound derived in Lemma 10. We see in Fig. 2.14 for $\lambda_S/\lambda_M = 5$ that the proposed bound is relatively loose but it provides the operator the guarantee that the overload probability will not exceed this value. Based on this bound and a constraint on the overall outage probability, a conservative network sizing can be derived. In Fig. 2.15, we show the minimum deployment density required such that feasible biases exist to meet both these constraints. The more stringent the constraints are, the more SBSs the operator should deploy. When the traffic density is low, the outage probability is the limiting constraint and accordingly, the minimum deployment density is the one required to maintain coverage. However, as traffic density increases, overloading probability is determining.

2.6.7 Rate Optimal Choice of Tier and RAT Selection Biases

In this section, we optimize tier and RAT selection biases with respect to the average effective throughput. To guarantee a good coverage, we impose a constraint on the outage probability (from 7.5 to 12.5%⁴). The MBS association probability corresponding to the optimal Q_T as a function of the traffic density

⁴Note that generally, PPP based modeling of cellular networks provide a pessimistic view of the network. Previous studies showed that an outage of 1% in hexagonal model corresponds to 10% outage in a PPP based modeling for the same network parameters [83].

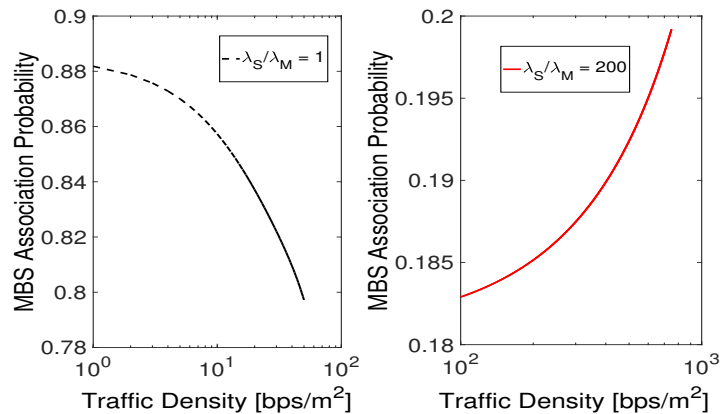


FIGURE 2.16: Throughput optimal MBS association probabilities.

is shown in Fig. 2.16. Depending on the ratio of densities λ_S/λ_M , users are offloaded from MBS to SBS (for low SBS densities) or vice-versa (for high SBS densities).

In Fig. 2.17, we show the optimal effective downlink throughput as a function of the traffic density for various deployment densities and outage constraints. We observe that more stringent outage constraints result in lower downlink throughput in the network. This is because biases are mainly optimized to guarantee coverage also for cell edge users. We also observe that increasing the SBS density not only results in higher throughput, but also increases the range of traffic densities that the network can serve, i.e., the network capacity. In this evaluation, we have obtained the downlink throughput by considering that the users in overloaded base stations receive zero throughput. Therefore, even though the network as a whole can serve traffic densities up to 1 Gbps/m², the MBS tier gets overloaded for much lower traffic densities. Accordingly, the network is no longer well-dimensioned for the region of traffic densities beyond the MBS overloading points. Furthermore, in Fig. 2.18, we plot the optimum association probabilities as a function of outage probability with $\lambda_S/\lambda_M = 50$ and traffic density of 200 bits·s⁻¹·m⁻². We see that for more stringent outage constraints, sub-6GHz service in SBSs becomes necessary, in addition to mm-wave service, to satisfy the QoS constraints of outage and overloading simultaneously, thus justifying the interest of deploying dual band SBSs.

As a conclusion, in dense SBS deployments (see Fig. 2.20), the users do not suffer from outage even in the case of high tier biases. In this case, Q_R should

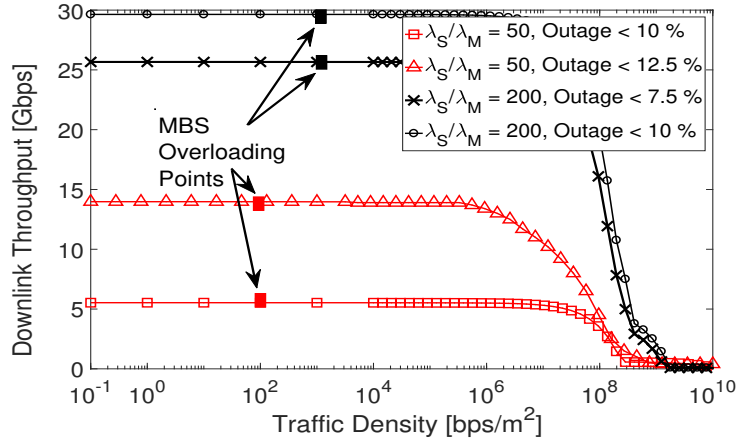


FIGURE 2.17: Optimal downlink user throughput

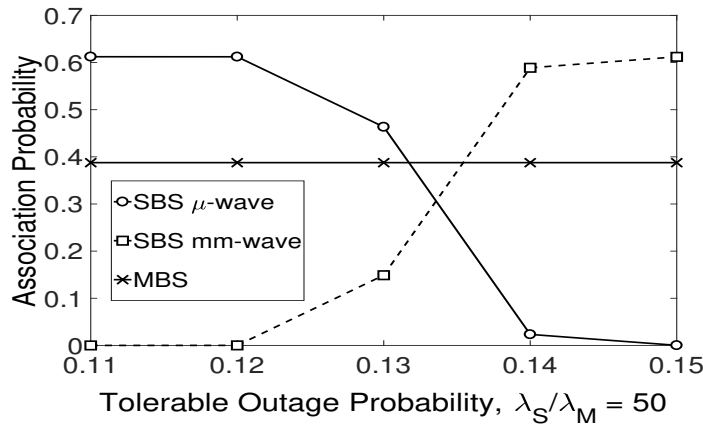


FIGURE 2.18: Optimal association probabilities for different outage probability constraints.

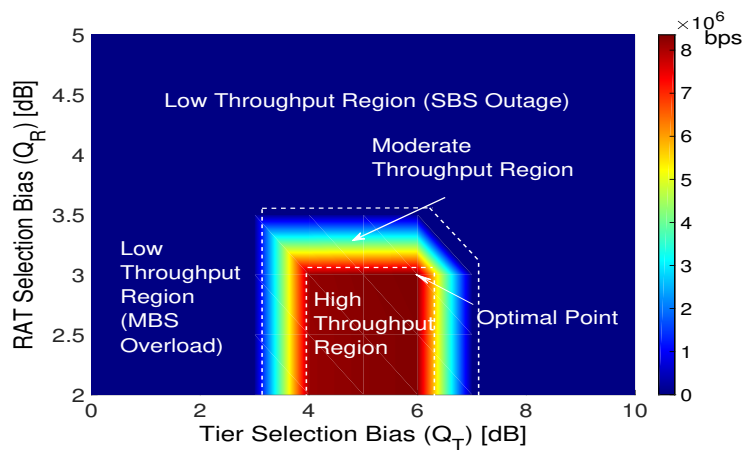


FIGURE 2.19: Effective user throughput vs Q_T and Q_R at a traffic density of $100 \text{ bits}\cdot\text{s}^{-1}\text{m}^{-2}$, tolerable outage probability of 0.10, $d_M = 200 \text{ m}$, $d_S = 20 \text{ m}$ for $\lambda_S/\lambda_M = 50$

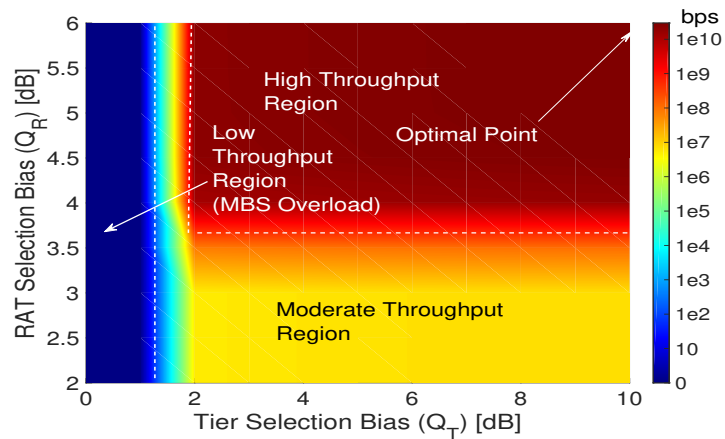


FIGURE 2.20: Effective user throughput vs Q_T and Q_R at a traffic density of $100 \text{ bits}\cdot\text{s}^{-1}\text{m}^{-2}$, tolerable outage probability of 0.10, $d_M = 200 \text{ m}$, $d_S = 20 \text{ m}$ for $\lambda_S/\lambda_M = 200$.

be high enough to maximize the mm-wave association probability. In case of $\lambda_S/\lambda_M = 200$, this results in a maximum throughput of around 30 Gbps at $Q_T = 10 \text{ dB}$ and $Q_R = 6 \text{ dB}$. In sparse SBS deployments (Fig. 2.19), high values of Q_T are desirable to offload traffic from overloaded MBSs. However, as the SBS ranges increase, mm-wave becomes unattractive for users at the SBS cell edges. We can observe that increasing Q_R beyond a certain limit pushes the SBS users in outage thereby decreasing the effective throughput. The maximum average throughput in this scenario, considering the regime of biases where the MBS tier is not overloaded, is 10 Mbps at $Q_T = 6 \text{ dB}$ and $Q_R = 3 \text{ dB}$.

2.7 Chapter Conclusion

In this chapter, we characterize a two tier network, consisting of classical sub-6GHz macro cells, and Multi RAT small cells, able to operate in sub-6GHz and mm-wave bands. First, we propose a two-step tier and RAT selection strategy where the sub-6GHz band is used to speed-up the initial access procedure in the mm-wave RAT, and then we investigate the effect of tier and RAT offloading in terms of SINR, cell load, and throughput. Our study highlights the fundamental trade-offs between outage probability, user throughput, and overloading probability, and, thereby, underscores the necessity of the dual band small cells to maintain outage below a certain threshold, specially in sparse deployments. In our system model, we have proposed effective approaches to optimize the user association. However, obtaining closed form solutions for the optimal biases and the maximum traffic density that the network can handle are open challenges.

Moreover, the dual band nature of the base stations calls for advanced radio resource management, which is an interesting topic to be investigated.

Chapter 3

Small Cell Deployment Along Roads: Coverage Analysis and Slice-Aware RAT Selection

3.1 Introduction

Future wireless applications anticipate an explosion in the plethora of use-cases, which cannot be sustained by incremental improvements on the existing communication schemes [2]. To address this, exploiting mm-wave spectrum for broadband services is gaining popularity. Additionally, mm-wave communications employ directional antennas, which reduces co-channel interference, thereby improving the performance at the UE [40]. However, mm-wave transmissions suffer from detrimental path-losses and high sensitivity to blockages [23]. For example, a vehicle located between a BS and a pedestrian UE may block the signal and induce a temporary service outage. To mitigate the path-loss, beam-forming techniques should be adopted, which poses issues in terms of coverage and initial access [41]. One solution to this problem consists of enabling the UEs to simultaneously receive signals in the mm-wave and in the sub-6GHz band, and to use the sub-6GHz to support the initial access on the mm-wave band [45].

Thus, it is unrealistic to assume ubiquitous coverage with only mm-wave SBSs, and it is envisioned that multiple RAT will co-exist in future [45]. The ad-hoc deployments of SBSs using multiple RAT will lead to a complex heterogeneous architecture. For example, in an urban scenario, the mm-wave SBSs can be deployed along the urban infrastructure, e.g., on top of lamp-posts [15]. Accordingly, it is important to characterize such a multi-tier multi-RAT network, and derive algorithms to optimize the UE and network performance, and

fully exploit the potential gains from mm-wave SBS deployment. In this chapter, we model a multi-tier network operating in sub-6GHz and mm-wave bands, where the SBSs are deployed along the roads. We characterize the UE performance in terms of SINR coverage probability, rate coverage probability, and vehicular blockages.

In the fourth generation (4G) networks, tier selection biasing is used mainly for load balancing. Offloading the UEs from the MBS to the SBSs is facilitated by a network-wide bias to expand the range of SBSs. On the contrary, we propose to use various RAT selection biases to distribute services among the available RATs in order to satisfy their quality of service (QoS) requirements. To sustain the diverse use cases of 5G, a mobile operator will be able to define service-based logical partitions of its network over a common physical infrastructure. *Network slicing* facilitates the creation and management of such network instantiations (the network slices), each one composed by functions and parameters (e.g., the RAT bias in our work) tailored to address specific requirements [84].

3.1.1 Related Work

In heterogeneous networks, the UE performance is analyzed using stochastic geometry by calculating the SINR coverage probability and rate coverage probability [85]. These metrics have been derived to investigate single-tier [69] and multi-tier mm-wave networks [71], as well as multi-RAT networks with mm-wave SBSs [73]. In literature, multi-tier networks are modeled using homogeneous two dimensional PPP [73, 71] or using repulsive processes [86]. These models, although tractable, are not able to capture the urban deployment of SBSs along the metropolitan infrastructure, e.g., along the roads and on lamp posts. For example, traditional models of such networks either consider only the proximity of the BS for UE association [73], or characterize UE association by modeling mm-wave link blockages using distance-based LOS ball models [71]. However, a BS located sufficiently close, but on a different street than that of a UE may not provide sufficient downlink power to the UE due to blockages by buildings, which is not straightforward to capture using single or multiple LOS ball models. In our work we address this issue by studying the performance of on-road deployment of mm-wave SBSs in a dense blocking environment.

In this regard, Gloaguen *et al.* [87] have modeled roads using either a Poisson

line tessellation (PLT), Poisson-Voronoi tessellation, or a Poisson-Delaunay tessellation. Specifically, using the PLT model, they have analyzed a two-tier wired network with respect to the mean shortest path length and the mean subscriber line length. The PLT was used by Morlot [88] to model the location of UEs and by Choi and Baccelli [89] to model vehicular BSs and UEs. In our previous work [90], we have characterized a multi-RAT network using SBS deployments based on a PLT and performed a first coverage analysis for pedestrian UEs.

Furthermore, the effect of the blockages due to vehicular traffic on the pedestrian UE performance is generally ignored. This inhibits a realistic study of the mm-wave cellular networks, since vehicular blockage is an integral part of a metropolitan scenario. Recently, Tassi *et al.* [91] have investigated a highway scenario with moving vehicles modeled as rectangles on the lanes. In our work, we model vehicles as cuboids, and analyze the effect of vehicular blockages on the pedestrian UE performance. Accordingly, we have revealed unique features of the network, especially related to how the UEs are distributed across various RATs to satisfy the associated slice requirements for varying degrees of link blockage due to the vehicles. Measurement campaigns affirm that in a street light based SBS deployment, the physical structures like buildings, vehicles etc. will be critical for performance evaluation [92]. Therefore, our model that takes into account blockages due to buildings and moving vehicles presents a very realistic characterization of such a network.

Finally, Foukas *et al.* [84] have provided a survey of the challenges in 5G network slicing. They have identified that the multiplexing of different RATs is *the* main challenge for resource virtualization. In this chapter, we provide a first study in this direction, in the context of multi-RAT multi-tier networks, by proposing a RAT selection mechanism to support applications on different network slices. The major contributions of this work are enumerated below.

3.1.2 Contributions and Organization

- We use the Poisson line process (PLP) to model the roads of an urban scenario on which multi-RAT SBSs, operating in both sub-6GHz and mm-wave bands are deployed to serve pedestrian UEs. Although this scenario is widely envisioned for future networks architectures, the investigation of such multi-tier, multi-RAT network has not yet been performed in the literature to the best of our knowledge. Thus, our analysis provides

more reliable results in terms of association probabilities and SINR coverage probabilities as compared to the traditional models.

- We propose a mm-wave interference model for SBS deployment along roads. For that, we derive the worst-case probability of the interference perceived at a UE from the n -th neighboring SBS. Then, we show that the accurate characterization of the mm-wave interference in presence of vehicular blockages is analytically difficult. We thus introduce a tractable dominant-interferer based interference model. We show that our model is more accurate in characterizing the SINR coverage as compared to a noise-limited approach, which is adopted for simple design of resource allocation and interference management mechanisms in mm-wave networks, see e.g. [93].
- We consider the effect of the vehicles that cause a temporary blockage in the LOS link between an outdoor UE and the SBSs. We exploit the properties of the PLCP to characterize the average vehicular blockage probability of a pedestrian UE from its serving SBS. This enables the operators to properly dimension the network so as to cater to the needs of reliability constrained applications. Although vehicular blockages are considered in studying vehicular communications [91], our model is the first tractable approach to analyze the UE performance in a multi-tier multi-RAT networks.
- We propose a two-step association policy where the UEs are connected to a tier based on the maximum received power in the sub-6GHz band. In case the UE associates to an SBS, it requests service from the RAT that provides the maximum biased instantaneous downlink received power. We compare this association scheme with an approach that uses an averaged power measured over a longer duration. We highlight that the first scheme suffers from an upper bound on the mm-wave selection probability, due to the vehicular blockages, and thus hampers aggressive mm-wave offloading. Using the derived results of the PLCP and the association probabilities with various tiers and RATs, we derive the SINR coverage probabilities for the UEs.
- Our results show that for a given density of the SBSs and vehicles, the optimal RAT selection bias should vary for addressing different service

requirements, e.g., vehicular blockage, coverage, and data rate. Accordingly, we consider different classes of services, namely URLLC, mMTC, and eMBB [94], and provide to the operator an algorithm to tune the RAT selection bias, in order to support their requirements.

The rest of the chapter is organized as follows. In Section 3.2, we present some preliminary results on the PLCP. In Section D.2, we introduce our system model. In Section 3.4, we characterize the vehicular blockage and mm-wave interference. The association probabilities and the SINR coverage probabilities are derived in Section 3.5 and Section 3.6, respectively. In Section 3.7 we present our slice-aware RAT selection strategy. Simulation results are provided in Section 3.8. Finally, the chapter concludes in Section 3.9.

3.2 Preliminary Results on PLCP

In this section, we present the construction and some salient properties of the PLCP. For that, we first describe the formation of a PLP, which will act as the domain of the PLCP.

3.2.1 PLCP Definition

A line process $\mathcal{P} \subset \mathbb{R}^2$ is a collection of random lines $\{L_1, L_2, \dots\}$ in the Euclidean plane. Any line that belongs to \mathcal{P} is uniquely characterized by the distance d between the origin O and its projection P on the line, and by the angle ψ between \vec{OP} and the x-axis on the other hand. Let the domain of the pair of parameters (ψ, d) be the half cylinder $\mathcal{C} := [0, 2\pi) \times \mathbb{R}^+$. We will call \mathcal{C} as the generating set of \mathcal{P} , and a point $x_i \in \mathcal{C}$, corresponding to a line $L_i \in \mathcal{P}$, the generating point of L_i . Accordingly, there is a bijective mapping $f : \mathcal{P} \rightarrow \mathcal{C}$ between any random point $x_i \in \mathcal{C}$ and a corresponding line $L_i \in \mathcal{P}$. We can now define a PLP.

Definition 2. *A line process $\mathcal{P} \triangleq \{L_i\}$ in \mathbb{R}^2 is a PLP, if and only if the set of corresponding generating points $\{x_i = f(L_i)\}$ is a PPP in \mathcal{C} .*

On every line $L_i \in \mathcal{P}$, we define a one-dimensional PPP (ϕ_i) , with intensity λ_S . The collection of all such points on all the lines of \mathcal{P} is a PLCP, denoted ϕ_S . Thus, the resulting point process is doubly stochastic, with the density concentrated along the lines. Naturally, $\phi_S = \cup_{i \in \mathcal{P}} \phi_i$.

Definition 3. A PLCP based on a PLP \mathcal{P} , is a process driven by a measure λ_S given by: $\lambda_S(B) = N\ell_1(\mathcal{P} \cap B)$, for a Borel set B , where N is a positive constant and ℓ_1 is the total length of all the lines of \mathcal{P} in B .

Definition 4. Two points x and x' are neighbors to each other, if and only if $\exists i: x, x' \in \phi_i$. Thus, from the perspective of one point x , all the neighbors on either side of it can be enumerated as n -th neighbors, where $n \in \mathbb{N} \setminus \{0\}$.

3.2.2 Palm Perspective of the PLCP

Let us study the PLCP from the perspective of a point of the process itself, using Palm calculus¹. Thanks to the Slivnyak's theorem [52] for a PPP (ϕ), conditioning on the event that a point of ϕ is located at the origin (o) (in other words $o \in \phi$), is equivalent to *add* a point at o to the PPP ϕ . Mathematically, $\mathbb{P}(\phi \in Y|o) = \mathbb{P}(\phi \cup \{o\} \in Y)$, where Y is any point process property. On similar lines, we state the following Lemma for a PLCP [88].

Lemma 12. For a PLCP \mathcal{P} , we have $\mathbb{P}(\phi_S \in Y|o) = \mathbb{P}(\phi_S \cup \phi_0 \cup \{o\} \in Y)$, where ϕ_0 is a realization of ϕ_i which passes through the origin.

In other words, Palm distribution i.e., conditioning on a point of ϕ_S to be at the origin, is equivalent to *add* (i) an independent Poisson process of intensity λ_S on a line through the origin with uniform independent angle and (ii) an atom at the origin to the PLCP. The implication of this result is observed in several results that we derive in this work. As an example, assume the SBSs are distributed as a PLCP. Then, if a UE is associated with an SBS located at x , then we have to condition the SBS process based on the fact that there exists a point of the SBS process located at x . This directly implies that the corresponding Palm process must include a line (road) containing SBSs passing through x .

3.2.3 Probability Generating Functionals of the PLCP

Here, we introduce the notion of the PGF of the point processes. The PGF of a point process ϕ evaluated for a function ν is defined mathematically as the Laplace functional of $-\log \nu$, and is calculated as: $G_\phi(\nu) = \mathbb{E} \left[\prod_{x_i \in \phi} \nu(x_i) \right]$, where the expectation is with respect to ϕ . In our study, the PGF is used for

¹In point process theory, the Palm probability refers to the probability of an event conditioned on a point of the process being located at a given position.

deriving the SINR coverage probability at the typical UE. For this, we derive the PGF of ϕ_S and ϕ_i :

Lemma 13. *The PGF of the stationary, isotropic PLCP ϕ_S is given by:*

$$G_{\phi_S}(\nu) = \exp \left(-2\pi\lambda_R \left(\int_0^\infty 1 - \exp \left(-2\lambda_S \int_0^\infty 1 - \nu \left(\sqrt{r^2 + t^2} \right) dt \right) dr \right) \right). \quad (3.1)$$

The PGF of the PPP ϕ_i , on a randomly oriented line, at a fixed distance d from the origin is:

$$G_{\phi_i,d}(\nu) = \frac{1}{\pi} \int_0^\pi \exp \left(-2\lambda_S \int_0^\infty \left(1 - \nu \left((d^2 + t^2 + 2td \cos \theta)^{\frac{1}{2}} \right) \right) dt \right) d\theta. \quad (3.2)$$

Proof. See Appendix A. □

Let us denote by $G_\phi^x(\nu)$, the conditional PGF of ν with respect to a point process ϕ given that there are no points of the process within a distance x from the origin. This is calculated by changing the lower limit of the outer integral in (3.1) and the inner integral in (3.2) from 0 to x . Finally, we note that as the UE compares the powers from the BSs of each tier, it is important to characterize the distance distributions of the nearest points of the PLCP.

Lemma 14. *Let the distance of the nearest point of the PLCP from the origin be given by d_1 . Then, the CDF, F_{d_1} , and the PDF of d_1 , f_{d_1} , are given by:*

$$\begin{aligned} F_{d_1}(x) &= \exp \left(-2\pi\lambda_R \left(x - \int_0^x \exp \left(-2\lambda_S \sqrt{x^2 - r^2} \right) dr \right) \right), \\ f_{d_1}(x) &= 2\pi\lambda_R F_{d_1}(x) \left[2\lambda_S x \int_0^x \frac{\exp(-2\lambda_S \sqrt{x^2 - r^2})}{\sqrt{x^2 - r^2}} dr \right]. \end{aligned} \quad (3.3)$$

Proof. See Appendix B.2. □

3.3 System Model

Consider an urban scenario with a dense blocking environment (see Fig. 3.1 for an illustration). In this scenario, we study the downlink characteristics of a

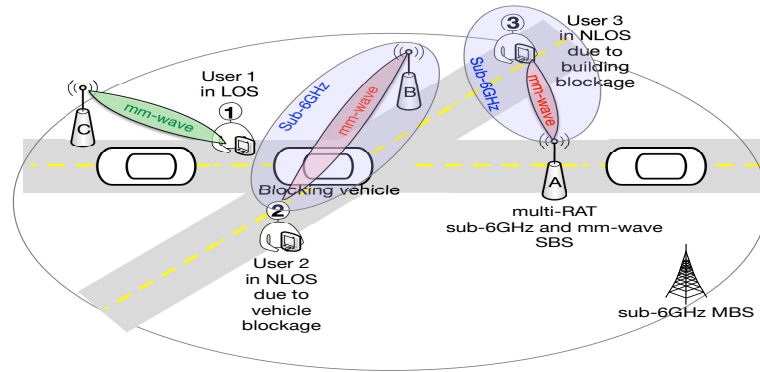


FIGURE 3.1: System model showing on-road deployment of SBSs with pedestrian UEs.

cellular network consisting of MBS and SBSs. The MBSs operate in the sub-6GHz band, whereas, the multi-RAT SBSs, deployed along the roads (e.g., on the lamp posts [15]), provide high data rate and ad-hoc coverage by jointly exploiting sub-6GHz and mm-wave bands. We assume that the sub-6GHz band is shared by MBSs and SBSs, so that UEs experience both co-tier and cross-tier interference in this band. We study the performance of the pedestrian UEs located on the sidewalks.

3.3.1 Network Geometry

The MBS locations are modeled as points of a homogeneous PPP ϕ_M with intensity λ_M defined on \mathbb{R}^2 . The roads are modeled as realizations of a PLP with intensity λ_R defined on $[0, 2\pi) \times \mathbb{R}^+$. Each road is assumed to contain one sidewalk for pedestrians. The SBSs are deployed on the PLT of the roads and their locations are modeled as the points of a PPP ϕ_i with intensity $\lambda_S \in \mathbb{R}^+$, where i is the index of the road. We denote by ϕ_S the overall SBS process. Furthermore, we consider pedestrian UEs on the sidewalks, whose locations are modeled as an independent stationary PPP ϕ_U along the PLT of roads, with an intensity $\lambda_U \in \mathbb{R}^+$. Thus, both the SBSs and UEs are modeled by PLCPs driven by the PLP [52].

3.3.2 Static Urban Blockage

For sub-6GHz transmissions from MBSs blockage is generally a secondary effect [95]; moreover, the path-loss exponent calculated from propagation measurements takes the blocking effects into account [78]. Mm-wave transmissions, on the other hand, suffer heavily from blockages and communication becomes

infeasible in case the link is blocked. Accordingly, we assume that the power received from a mm-wave SBS whose signal is blocked by a building is null [37].

Due to random blockages, MBSs can be categorized into either LOS or NLOS processes: ϕ_{ML} and ϕ_{MN} , respectively. The intensities of these modified processes are given by $p_M(r)\lambda_M$, and $(1 - p_M(r))\lambda_M$, respectively, where $p_M(r)$ is the probability of an MBS located at a distance r from the UE to be in LOS. In our work, we use the LOS ball approximation [69]. Accordingly, let D_M be the MBS LOS ball radius. The probability of the typical UE to be in LOS from a MBS at a distance r is $p_M(r) = 1$, if $r < D_M$, and $p_M(r) = 0$, otherwise.² Furthermore, due to the blockage by buildings, all SBSs in other streets as that of a UE are considered to be in NLOS with respect to that UE (e.g., UE 3 and SBS A in the figure) and are denoted by a process ϕ_{SN} ; all SBSs in the same street are denoted by a process ϕ_{SL} and are in LOS (e.g., UE 1 and SBS C) except if vehicles block the signal at cross-roads between the transmitter and the receiver (e.g., UE 2 and SBS B). In our analysis, we use the subscript notation t, v, r , where $t \in \{M, S\}$ denotes the tier (MBS or SBS), $v \in \{L, N\}$ denotes the visibility state, i.e., LOS and NLOS, and $r \in \{\mu, m\}$ denotes the RAT (sub-6GHz or mm-wave). We use the subscript “1” when referring to the *closest* BS of each type. The distance distributions of the nearest BSs of each type and visibility state is given in the following lemma:

Lemma 15. *The distribution of the distance from a UE to the nearest NLOS SBS (d_{SN1}) is given by (3.3). Whereas, the distributions of the distances from a UE to the closest LOS SBS (d_{SL1}), LOS MBS (d_{ML1}), and NLOS MBS (d_{MN1}) are given by:*

$$\begin{aligned} f_{d_{SL1}}(x) &= 2\lambda_S \exp(-2\lambda_S x), & f_{d_{ML1}}(x) &= 2\pi\lambda_M x \exp(-\pi\lambda_M x^2); & x < D_M, \\ f_{d_{MN1}}(x) &= 2\pi\lambda_M x \exp(-\pi\lambda_M (x^2 - D_M^2)); & & & x \geq D_M, \end{aligned} \quad (3.4)$$

3.3.3 Blockage due to Moving Vehicles

We assume that vehicles located on the roads may cause blockage to the mm-wave links. Due to our assumption that the UEs are on the sidewalks, vehicular blockage is caused by vehicles present at crossings of the roads between the UEs and the SBS (see Fig. 1). Let the vehicles be of length L_V and relative height h_V with respect to the UE, and located equidistant from each other. Accordingly,

²We convert the semi-graded LOS probability model recommended by 3GPP [77] to a step probability model, following criterion 1 in [76].

if the density of the vehicles is λ_V , the fraction of the roads occupied by the vehicles is $\lambda'_V = L_V \cdot \lambda_V$. Due to the high penetration losses of mm-wave transmissions, we assume that the mm-wave signals are completely lost in case the path between the SBS and the UE is obstructed by a vehicle [37].³ Although mm-waves can provide very high throughputs, the blockage due to vehicles can be detrimental for services requiring a high reliability. Note that although secondary paths may exist for mm-wave propagation due to specular reflections, we assume that reflected signals contribute insignificantly to the received power. As a consequence, a mm-wave signal blocked by a vehicle is received with zero power.

3.3.4 Path Gain

The path-gain at a distance d_{tvr} from a transmitter is given by $h_r K_r d_{tvr}^{-\alpha_{tvr}}$, where K_r and α_{tvr} are the path-loss coefficient and exponent, respectively. For sub-6GHz communications, we assume a Rayleigh fast fading h_μ , with unit variance. Whereas, due to the low local scattering, we consider a Nakagami fading h_m with shape factor n_0 for mm-wave communications [95]. In our work, we assume a sectored model for the transmission pattern of the mm-wave antennas [69], consisting of a main-lobe of beamwidth θ , and a side-lobe. Let G_0 be the directivity gain product of the main-lobe transmitting and receiving antenna⁴; then, the received power at a distance d_{tvr} is given by $P_{tv\mu} = P_t h_\mu K_\mu d_{tvr}^{-\alpha_{tv\mu}}$ for sub-6GHz and $P_{tvm} = G_0 P_t h_m K_m d_{tvm}^{-\alpha_{tvm}}$ for mm-wave transmissions, where P_t is the transmit power of a BS of tier t . Following our observations on mm-wave blockage for NLOS SBS, we have, $P_{SNm} = 0$.

3.3.5 Tier and RAT Selection Procedure

We assume that the UEs are uniformly distributed along the roads, and associate to the BS providing the maximum downlink received power. For this, the BSs send their control signals in the sub-6GHz band, which is more reliable as compared to the mm-wave band. A UE may select mm-waves RAT when the strongest BS is an SBS. In this case, it compares the power in sub-6GHz band (i.e., $P_S h_\mu K_\mu d_{Sv\mu}^{-\alpha_{Sv\mu}}$) with that in the mm-wave band biased by a multiplicative

³Thanks to multi-path propagation and larger beam-widths, which result in larger angular spread for the signal, we assume that the vehicular blockages do not affect the sub-6GHz band communications significantly.

⁴For highly directional antennas, the side-lobe gain is negligible; thus, for simplicity, we assume it to be zero.

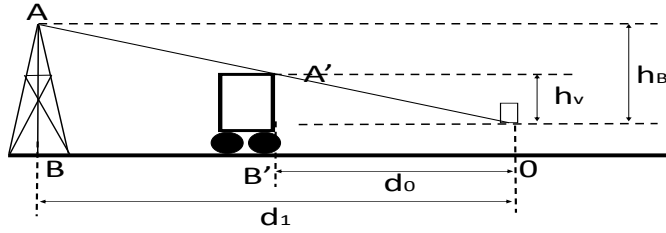


FIGURE 3.2: Model for calculating the blockage due to moving vehicles.

factor Q_R (i.e., $Q_R G_0 P_t h_m K_m d_{tvm}^{-\alpha_{Svm}}$). The parameter Q_R is called the RAT selection bias and will be used to differentiate the network slices.

The power in each band can be either measured instantaneously, or averaged over a time window. In the *instantaneous power RAT selection* case, the UE simultaneously measures the mm-wave power received in different control channels and averages out the effect of fast fading. The instantaneous vehicular blockage condition may however inhibit a proper RAT selection. When *averaged power RAT selection* is performed, the UE measures the mm-wave power for a longer duration of time attempting to average out the effect of the vehicular blockages as well, which gives a more accurate idea of the radio scene. In our analysis we will compare the mm-wave selection probability of both these schemes.

Finally, the way the parameter Q_R should be optimized is highly dependent on the QoS requirements of each slice. We thus assume that the UEs are connected to a slice characterized by QoS triplets $T^* = (\mathcal{B}^*, \mathcal{P}_C^*, \mathcal{P}_R^*)$, where \mathcal{B}^* is the tolerable vehicular blockage probability, \mathcal{P}_C^* is the minimum SINR coverage probability, and \mathcal{P}_R^* is the target rate coverage.

3.4 Vehicular Blockage and mm-wave Interference

In this section, we derive the vehicular blockage probability, and we propose an interference model for system-level evaluations of mm-wave networks.

3.4.1 Characterization of the Vehicular Blockage Probability

We study the blockages of the link between the SBSs and the UEs due to the vehicles (see Fig. 3.2), and use this result to derive the mm-wave selection

probability and the overall SINR.

Proposition 3. *The probability that a link between an SBS and a UE at a distance d is not blocked by a vehicle is given by: $\mathcal{L}(d) = \exp\left(-\lambda'_V \lambda_R \frac{h_V}{h_B} d\right)$, where h_B is the relative height of the SBS with respect to the UE. Thus, the vehicular blockage probability $\mathcal{B}(Q_R)$, i.e., the probability given Q_R that a UE served in the mm-wave RAT is blocked by a vehicle is given by:*

$$\mathcal{B}(Q_R) = \int_0^H \left(1 - \exp\left(-\lambda_R \lambda'_V \frac{h_V}{h_B} x\right)\right) f_{d_{SL1}}(x) dx, \quad (3.5)$$

where the upper limit in the integral is given by $H = \left(\frac{K_m G_0 Q_R}{K_\mu}\right)^{\frac{1}{\alpha_{SLm} - \alpha_{SL\mu}}}$.

Proof. See Appendix B.3. □

3.4.2 Interference Characterization in mm-wave

Interference models traditionally used in the stochastic geometry literature are planar and thus ignore the elevation of the antenna pattern. In this section, we propose a model to overcome this limitation in a tractable way for accurately analyzing a scenario where the SBSs are deployed along a road. For this, we first characterize the interference caused by an SBS to a UE served by its n -th neighboring SBS of the same street. Observe that the SBS to which a UE U is associated (SBS 1 in Fig. 3.3a), causes interference to UEs located in the n -th neighboring SBS if its beam reaches (at location X on the figure) the n -th cell. As a worst case interference scenario, assume 1) that U is located at cell boundary (at distance $\frac{d_a}{2}$ from the SBS, where d_a is the distance between SBSs 1 and 2) and 2) that this interfering signal is not obstructed by any vehicle.

Lemma 16. *In the worst case scenario, the probability that an SBS causes interference in mm-wave transmissions in the coverage area of its n -th neighbor is given by:*

$$\mathcal{P}_{n,WC} = \mathbb{E}_{d_{n-1}, d_n} \left[\exp\left(-2\lambda_S h_B \frac{d_n + d_{n-1} - 2h_B \tan \frac{\theta}{2}}{2h_B + (d_n + d_{n-1}) \tan \frac{\theta}{2}}\right) \right], \quad (3.6)$$

where d_n and d_{n-1} are the distances between the serving SBS and the n -th and $(n-1)$ -th neighboring SBS, respectively, and θ is the beamwidth. The expectation is with respect to the joint distribution of d_n and d_{n-1} , which is given by $f_{d_{n-1}, d_n}(x, y) = \frac{\lambda_S^2 \exp(-\lambda_S y)}{(n-2)!} (\lambda_S x)^{n-2}$, for $y \geq x$.

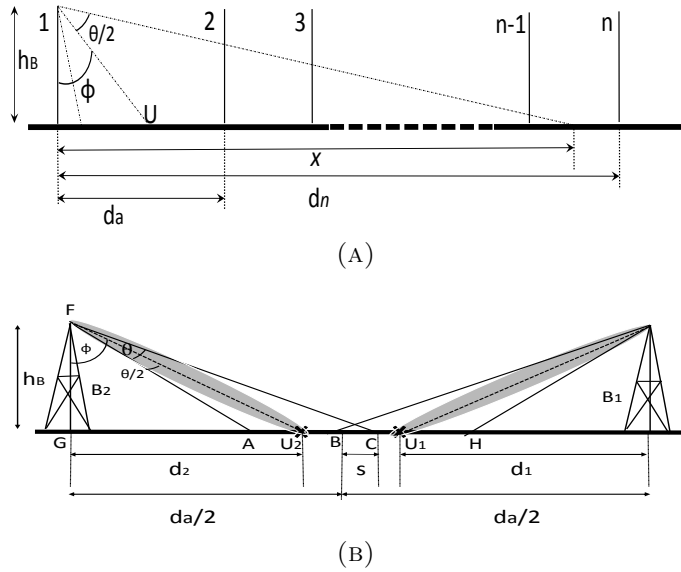


FIGURE 3.3: (a) Interference to the n-th SBS from the typical SBS, and (b) Simplified interference model for LOS mm-wave SBS.

Proof. See Appendix B.4. □

In the general case, the accurate characterization of the actual interference is relatively difficult, precisely due to two reasons: 1) the position distributions of the served UEs for each SBS up to the n-th SBS should be taken into account, and 2) in the presence of vehicular blockages, the number of neighboring blocked SBSs that do not contribute to the interference, is a random variable. Moreover, our results in Section 3.8 suggest that the dominant-interferer contributes to almost all the interference. Our model is thus based on the following assumption.

Assumption 1. *The closest SBS on the opposite side than that of the serving SBS, i.e., the dominant-interferer, is the only SBS that creates substantial interference to the UEs in mm-wave. Accordingly, if the dominant-interferer is blocked, the mm-wave transmission is noise-limited.*

Based on this assumption, we compute the probability \bar{p}_G that the dominant-interferer creates interference to the typical UE, in case it is not blocked by a vehicle. As shown in Fig. 3.3b, the dominant-interferer B_2 causes interference if its beam partly overlaps the coverage of SBS B_1 .

Lemma 17. *For an arbitrary small beamwidth θ , the typical UE experiences mm-wave interference from its closest neighboring SBS with a probability (\bar{p}_G) given by (3.7), where $x_0 = 2h_B \tan\left(\frac{\theta}{2}\right)$, $x_1 = h_B \tan\left(\arctan\frac{x}{2h_B} - \frac{\theta}{2}\right)$, $x_2 =$*

$$\begin{aligned} \bar{p}_G = \int_{x_0}^{\infty} \int_{x_1}^{x_2} \exp\left(-\lambda_S \left(x - h_B \tan\left(\frac{\theta}{2} + \arctan\frac{y}{h_B}\right)\right)\right) \left(1 - \exp\left(\lambda_U \left(\frac{x}{2} - x_1\right)\right)\right) + \\ f_{yx}(y, x) dy dx \int_{x_0}^{\infty} \int_{x_2}^{\frac{x}{2}} \left(1 - \exp\left(\lambda_U \left(\frac{x}{2} - x_1\right)\right)\right) f_{yx}(y, x) dy dx. \end{aligned} \quad (3.7)$$

$h_B \tan\left(\arctan\left(\frac{x}{h_B}\right) - \frac{\theta}{2}\right)$, and $f_{xy}(x, y) = \lambda_S \lambda_U \exp(-\lambda_S x) \exp(-\lambda_U (\frac{x}{2} - y))$.

Proof. See Appendix B.5. \square

The condition on the beamwidth comes from the simplifying assumption that the spillover created by the SBS B_2 by serving a UE U_2 in its neighboring cell B_1 does not go beyond B_1 ⁵.

This model has the advantage of being tractable for system level evaluations. It also provides more accurate results than a noise-limited approach (see Section 3.8).

3.5 Association Probabilities

In this section, we derive the BS tier selection probabilities and the RAT selection probabilities for mm-wave and sub-6GHz bands.

3.5.1 Tier Selection for a UE

For each UE, there are four cases for the serving BS: MBS in LOS (ML), MBS in NLOS (MN), SBS in LOS (SL), and SBS in NLOS (SN). Let E_{tv} denote the event that the serving BS is of tier $t \in \{M, S\}$ and in visibility state $v \in \{L, N\}$. In what follows, we describe the association probabilities for the case where $\{tv\} = \{ML\}$. Note that for E_{ML} , we only have to consider the joint event $\{P_{ML1} > P_{SL1}\} \cap \{P_{ML1} > P_{SN1}\}$ as in our model we always have $P_{ML1} > P_{MN1}$. This event can occur in two ways: (i) $P_{ML1} > P_{SL1} > P_{SN1}$, or (ii) $P_{ML1} > P_{SN1} > P_{SL1}$. For the first event (i):

$$P_{ML1} > P_{SL1} > P_{SN1} \iff \left(\frac{P_S}{P_M} d_{ML1}^{\alpha_{ML\mu}}\right)^{\frac{1}{\alpha_{SL\mu}}} < d_{SL1} < d_{SN1}^{\frac{\alpha_{SN\mu}}{\alpha_{SL\mu}}}.$$

⁵For a given θ , this occurs with a probability $\exp\left(\frac{h_B}{2 \tan(\frac{\theta}{2})} \sqrt{1 - \tan^2(\frac{\theta}{2})}\right)$, which tends to 1 as $\theta \rightarrow 0$. In deterministic deployments, an operator can set $\theta \leq 2 \arctan\left(\frac{h_B d_a}{2h_B^2 + d_a^2}\right)$ to ensure that this condition always holds.

$$\begin{aligned}
\mathcal{P}_{ML} &= W_1 \left(\int_0^\infty \int_x^\infty \exp \left(-2\lambda_S \left(y^{\frac{\alpha_{SN\mu}}{\alpha_{SL\mu}}} - \left(\frac{P_S}{P_M} x^{\alpha_{ML\mu}} \right)^{\frac{1}{\alpha_{SL\mu}}} \right) \right) \mathcal{T}_1(x) f_{d_{SN1}}(y) f_{d_{ML1}}(x) dy dx + \right. \\
&\quad \left. \int_0^\infty \int_0^x \left(F_{d_{SN1}} \left(x^{\frac{\alpha_{SL\mu}}{\alpha_{SN\mu}}} \right) - F_{d_{SN1}} \left(\left(\frac{P_S}{P_M} x^{\alpha_{ML\mu}} \right)^{\frac{1}{\alpha_{SN\mu}}} \right) \right) F_{d_{SN1}} \left(x^{\frac{\alpha_{SL\mu}}{\alpha_{SN\mu}}} \right) f_{d_{ML1}}(y) f_{d_{SL1}}(x) dy dx \right). \\
\mathcal{P}_{MN} &= (1 - W_1) \left(\int_0^\infty \int_0^x \exp \left(-2\lambda_S \left(y^{\frac{\alpha_{SN\mu}}{\alpha_{SL\mu}}} - \left(\frac{P_S}{P_M} x^{\alpha_{MN\mu}} \right)^{\frac{1}{\alpha_{SL\mu}}} \right) \right) \mathcal{T}_2(x) f_{d_{SN1}}(y) f_{d_{MN1}}(x) dy dx + \right. \\
&\quad \left. \int_0^\infty \int_x^\infty \left(F_{d_{SN1}} \left(x^{\frac{\alpha_{SL\mu}}{\alpha_{SN\mu}}} \right) - F_{d_{SN1}} \left(\left(\frac{P_S}{P_M} y^{\alpha_{MN\mu}} \right)^{\frac{1}{\alpha_{SN\mu}}} \right) F_{d_{SN1}} \left(x^{\frac{\alpha_{SL\mu}}{\alpha_{SN\mu}}} \right) \right) f_{d_{MN1}}(y) f_{d_{SL1}}(x) dy dx \right). \\
\mathcal{P}_{SL} &= W_1 \left(\int_0^\infty \int_x^\infty \exp \left(-\pi\lambda_M \left(\left(\frac{P_M}{P_S} y^{\alpha_{SN\mu}} \right)^{\frac{1}{\alpha_{ML\mu}}} - \left(\frac{P_M}{P_S} x^{\alpha_{SL\mu}} \right)^{\frac{1}{\alpha_{ML\mu}}} \right) \right) \mathcal{T}_2(x) f_{d_{SL1}}(x) f_{d_{SN1}}(y) dy dx + \right. \\
&\quad \int_0^\infty \int_0^x \left(F_{d_{SN1}} \left(\left(\frac{P_S}{P_M} x^{\alpha_{ML\mu}} \right)^{\frac{1}{\alpha_{SN\mu}}} \right) - F_{d_{SN1}} \left(y^{\frac{\alpha_{SL\mu}}{\alpha_{SN\mu}}} \right) F_{d_{SN1}} \left(\left(\frac{P_S}{P_M} x^{\alpha_{ML\mu}} \right)^{\frac{1}{\alpha_{SN\mu}}} \right) \right) f_{d_{SL1}}(y) f_{d_{ML1}}(x) dy dx \\
&\quad + (1 - W_1) \left(\int_0^\infty \int_x^\infty \exp \left(-\pi\lambda_M \left(\left(\frac{P_M}{P_S} y^{\alpha_{SN\mu}} \right)^{\frac{1}{\alpha_{MN\mu}}} - \left(\frac{P_M}{P_S} x^{\alpha_{SL\mu}} \right)^{\frac{1}{\alpha_{MN\mu}}} \right) \right) \mathcal{T}_3(x) f_{d_{SL1}}(x) f_{d_{SN1}}(y) dy dx + \right. \\
&\quad \left. \int_0^\infty \int_0^x \left(F_{d_{SN1}} \left(\left(\frac{P_S}{P_M} x^{\alpha_{ML\mu}} \right)^{\frac{1}{\alpha_{SN\mu}}} \right) - F_{d_{SN1}} \left(y^{\frac{\alpha_{SL\mu}}{\alpha_{SN\mu}}} \right) F_{d_{SN1}} \left(\left(\frac{P_S}{P_M} x^{\alpha_{ML\mu}} \right)^{\frac{1}{\alpha_{SN\mu}}} \right) \right) f_{d_{SL1}}(y) f_{d_{MN1}}(x) dy dx \right). \tag{3.8}
\end{aligned}$$

Using the CDF of d_{SL1} (see Lemma 15), for given instances of d_{ML1} and d_{SN1} , we have:

$$\begin{aligned}
&\mathbb{P} \left(\left(\frac{P_S}{P_M} d_{ML1}^{\alpha_{ML\mu}} \right)^{\frac{1}{\alpha_{SL\mu}}} < d_{SL1} < d_{SN1}^{\frac{\alpha_{SN\mu}}{\alpha_{SL\mu}}} \mid d_{ML1}, d_{SN1} \right) = \\
&\exp \left(-2\lambda_S \left(d_{SN1}^{\frac{\alpha_{SN\mu}}{\alpha_{SL\mu}}} - \left(\frac{P_S}{P_M} d_{ML1}^{\alpha_{ML\mu}} \right)^{\frac{1}{\alpha_{SL\mu}}} \right) \right) \cdot \exp \left(-2\lambda_S \left(\left(\frac{P_S}{P_M} x^{\alpha_{ML\mu}} \right)^{\frac{1}{\alpha_{SL\mu}}} \right) \right).
\end{aligned}$$

Then, taking the expectations with respect to d_{ML1} and d_{SN1} (see Lemmas 14 and 15), we evaluate the probability of (i). Similarly, we can evaluate the probability of the event (ii), where in the first step, we use the CDF of the variable d_{SN1} , and then we take expectations with respect to d_{ML1} and d_{SL1} . Finally, to compute the overall ML association probability, the sum of the probabilities of (i) and (ii) is multiplied with the probability that there exists a LOS MBS, i.e., $W_1 = 1 - \exp(-\pi\lambda D_M^2)$. In a similar manner, all the other probabilities are calculated.

Proposition 4. *The probabilities of association of a UE with a LOS and NLOS MBS and LOS SBS are given by (3.8), where:*

$$\begin{aligned}
W_1 &= 1 - \exp(-\pi\lambda_M D_M^2), \quad \mathcal{T}_1(x) = \exp \left(-2\lambda_S \left(\left(\frac{P_S}{P_M} x^{\alpha_{ML\mu}} \right)^{\frac{1}{\alpha_{SL\mu}}} \right) \right), \\
\mathcal{T}_2(x) &= \exp \left(-2\lambda_S \left(\frac{P_S}{P_M} x^{\alpha_{MN\mu}} \right)^{\frac{1}{\alpha_{SL\mu}}} \right), \\
&\text{and } \mathcal{T}_3(x) = \exp \left(-\pi\lambda_M \left(\left(\frac{P_M}{P_S} x^{\alpha_{SL\mu}} \right)^{\frac{1}{\alpha_{MN\mu}}} \right) \right).
\end{aligned}$$

$F_{d_{SN1}}(x)$ refers to the CDF of the first NLOS SBS, as given by Lemma 14. The association probability of the typical UE with an NLOS SBS is then given by: $\mathcal{P}_{SN} = 1 - \mathcal{P}_{ML} - \mathcal{P}_{MN} - \mathcal{P}_{SL}$.

Proof. See Appendix B.6. \square

We now derive the distribution of the distance between a UE and its associated serving BS.

Lemma 18. *Given that a UE is associated to a BS of a tier t with visibility state v , the PDF of its distance from the serving BS is given by:*

$$\hat{f}_{d_{tv1}}(x) = \frac{f_{d_{tv1}}(x)}{\mathcal{P}_{tv}} \prod_{\forall(t'v' \neq tv)} \mathbb{P}(\phi_{t'v'} \cap (0, x) = 0), \quad (3.9)$$

where $f_{d_{tv1}}(x)$ is the PDF of the distance of the nearest BS of type tv , $t \in \{M, S\}$ and $v \in \{L, N\}$, as derived in (3.4).

3.5.2 RAT Selection for Pedestrian UE

After having selected an SBS as the serving BS, a UE shall select the serving RAT. We thus derive and analyze the mm-wave selection probabilities for 1) the instantaneous power RAT selection scheme and 2) the averaged power RAT selection scheme.

Proposition 5. *The conditional mm-wave selection probability, given that the UE is associated with an LOS SBS and use instantaneous power RAT selection is given by:*

$$\mathcal{P}_m = \frac{2h_B\lambda_S}{\lambda'_V h_V \lambda_R + 2h_B\lambda_S} \left[1 - \exp \left(-2\lambda_S \left(\frac{K_m G_0 Q_R}{K_\mu} \right)^{\frac{1}{\alpha_{SLm} - \alpha_{SL\mu}}} \right) \right]. \quad (3.10)$$

In case the UE selects the RAT by adopting the averaged power RAT selection scheme, the mm-wave selection probability is given by:

$$\bar{\mathcal{P}}_m = \exp \left(\frac{-2\lambda_S h_B (\alpha_{SLm} - \alpha_{SL\mu})}{\lambda'_V \lambda_S h_V} \mathcal{W} \left(\frac{\lambda'_V \lambda_S h_v}{h_B (\alpha_{SLm} - \alpha_{SL\mu})} \left(\frac{K_m G_0 Q_R}{K_\mu} \right)^{\frac{1}{\alpha_{SLm} - \alpha_{SL\mu}}} \right) \right). \quad (3.11)$$

where \mathcal{W} is the Lambert W-Function.

Proof. See Appendix B.7. \square

From this lemma, some immediate observations follow as given below.

Remark 1. From (3.10), we observe that the mm-wave selection probability in case of instantaneous power RAT selection is upper bounded by $\mathcal{P}_m^* = \frac{2h_B\lambda_S}{\lambda_V h_V \lambda_R + 2h_B\lambda_S}$, regardless of G_0 or Q_R . From (3.11), we observe that with averaged power scheme, it is possible to have a greater degree of RAT tunability (because $\bar{\mathcal{P}}_m \rightarrow 1$ as $Q_R \rightarrow \infty$ or $G_0 \rightarrow \infty$).

The overall association probability of the typical UE is given by $\mathcal{P}_{tvr} = \mathcal{P}_{tv}\mathcal{P}_r$. When the serving BS is not a LOS SBS, as we have exclusively sub-6GHz operation ($r = \mu$), it follows that $\mathcal{P}_m = \bar{\mathcal{P}}_m = 0 \forall \{t, v\} \neq \{S, L\}$.

3.6 SINR Coverage Probabilities

In this section, we derive the downlink SINR coverage probability of the typical UE, which is mathematically defined as $\mathcal{P}_C(\gamma) = \mathbb{P}(\text{SINR} > \gamma)$. Following the theorem of total probabilities:

$$\mathcal{P}_C(\gamma) = \sum_{t \in \{M, S\}, v \in \{L, N\}, r \in \{\mu, m\}} \mathbb{P}(\text{SINR}_{tvr} > \gamma | t, v, r) \mathcal{P}_{tvr}. \quad (3.12)$$

In case of mm-wave association, we provide a lower bound of the SINR coverage probability, which we show to be tight in Section 3.8.1.

Theorem 1. *The conditional SINR coverage probability, given that the typical UE is associated to a BS of type 'tv' in sub-6GHz is given by:*

$$\mathbb{P}(\text{SINR}_{tv\mu} \geq \gamma) = \mathbb{E}_{d_{tv1}} \left[\exp \left(-\frac{\gamma \sigma_\mu^2}{P_S K_\mu d_{tv1}^{-\alpha_{SL\mu}}} \right) \prod_{\substack{\{t'v'\} \\ \neq \{tv\}}} G_{\phi_{t'v'}}^{\bar{d}_{tv}} \left(\frac{P_{t'} x^{\alpha_{t'v'}}}{P_{t'} x^{\alpha_{t'v'}} + \gamma P_t d_{tv1}^{\alpha_{tv}}} \right) \cdot \right. \\ \left. G_{\phi_{i, d_{SN1}}}^{\bar{d}_{tv}} \left(\frac{\gamma d_{S1}^{\alpha_{SN\mu}}}{x^{\alpha_{SN\mu}} + \gamma d_{S1}^{\alpha_{SN\mu}}} \right) G_{\phi_{tv} \setminus \{tv1\}}^{d_{tv1}} \left(\frac{x^{\alpha_{tv}}}{x^{\alpha_{tv}} + \gamma d_{tv1}^{\alpha_{tv}}} \right) \right]. \quad (3.13)$$

For NLOS SBS association, i.e., $t = S$ and $v = N$, the term $G_{\phi_{i, d_{SN1}}}^{\bar{d}_{tv}}(\cdot)$ is replaced by $G_{\phi_{i, d_{S1}} \setminus \{SN1\}}^{\bar{d}_{tv}}(\cdot)$. The PGFs of the NLOS SBS process are given in Lemma 13. For the PGF of the MBS and LOS SBS processes, see [52]. The conditional SINR coverage probability, given that the typical UE is associated to

a SBS in mm-wave is lower bounded by:

$$\begin{aligned} & \mathbb{P}(SINR_{SLm} \geq \gamma) \\ & \geq \sum_{n=1}^{n_0} (-1)^{n+1} \binom{n_0}{n} \mathbb{E}_{d_{SL1}, d_{SL2}} \left[\exp(-n\gamma_0 d_{SL1}^{-\alpha_{SLm}} \exp(K_0 d_{SL1})) \right. \\ & \quad \left. \frac{\exp(-K_0 d_{SL1}) d_{SL1}^{-2}}{\exp(-K_0 d_{SL1}) d_{SL1}^{-2} + n\gamma p_G \exp(-K_0 d_{SL2}) d_{SL2}^{-2}} \right], \end{aligned} \quad (3.14)$$

where $K_0 = \lambda_R \lambda_V \frac{h_V}{h_B}$, $\tilde{d}_{tv} = \left(\frac{P_t'}{P_t} d_{tv1}^{\alpha_{tv1}} \right)^{\frac{1}{\alpha_{t'v'1}}}$, and the expectation is taken with respect to the joint distribution of d_{SL1} and d_{SL2} : $f_{d_{SL2}, d_{SL1}}(x, y) = 2\lambda_S^2 \exp(-\lambda_S(x+y))$.

Proof. See Appendix B.8. □

Once the SINR coverage probability is obtained, the rate coverage probability for each tier and RAT is computed as: $\mathcal{P}_{R_{tvr}}(r_0) = \mathbb{P}\left(SINR_{tvr} \geq 2^{\frac{r_0}{B}} - 1\right) = \mathbb{P}_{C_{tvr}}\left(2^{\frac{r_0}{B_r}} - 1\right)$. Consequently, the overall rate coverage probability follows from the theorem of total probabilities:

$$\mathcal{P}_R(r_0) = \sum_{t \in \{M, S\}, v \in \{L, N\}, r \in \{\mu, m\}} \mathbb{P}(SINR_{tvr} > 2^{\frac{r_0}{B_r}} - 1 | t, v, r) \mathcal{P}_{tvr}. \quad (3.15)$$

3.7 A Slice-Aware RAT Selection Mechanism

3.7.1 Effect of RAT Selection Bias on Blockage, SINR, and Rate

We analyze the RAT selection from the perspective of three services [94]: i) URLLC characterized by tight link blockage requirement and high SINR coverage constraint, ii) mMTC characterized by continuous and ubiquitous coverage requirement and less stringent blockage constraints, and iii) eMBB characterized by high data rate requirement, under coverage constraints. In this section, we highlight the impact of the RAT selection probability on the blockage, SINR, and data rate. We then propose a slice-aware RAT selection strategy for the three services.

Effect of Bias on Blockage

For blockage-sensitive UEs, Q_R should be such that the vehicular blockage probability given that a UE is served in mm-wave band (3.5) is limited.

Remark 2. From (3.5), we observe that $\mathcal{B}(Q_R)$ increases with Q_R , and thus, for a given λ_S , there exists a maximum value of Q_R , beyond which the vehicular blockages become unacceptable. As $Q_R \rightarrow \infty$, the vehicular blockage probability, $\mathcal{B}(Q_R)$, attains a value $1 - \mathcal{P}_m^*$, where \mathcal{P}_m^* is the maximum mm-wave selection probability given in Remark 1.

Corollary 2. Leveraging on Remark 2, the minimum SBS deployment density that guarantees the vehicular blockage probability to be less than \mathcal{B}^* , regardless of the RAT biasing is:

$$\lambda_S^* = \frac{(1 - \mathcal{B}^*)}{2\mathcal{B}^*} \lambda_R \lambda_V \frac{h_V}{h_B}. \quad (3.16)$$

This enables the operator to properly dimension the cellular network, in terms of the minimum deployment density of SBS, so as to ensure reliable mm-wave service.

Effect of Bias on SINR and Data Rate

As we will show in Section 3.8-C, for a given λ_S , the SINR and rate coverage probability can either decrease or increase, depending on λ_V . In some cases, a non-trivial optimal RAT selection bias exists. This optimal RAT bias values (distinct for SINR and rate) can be obtained using a random-restart hill climbing algorithm [45].

3.7.2 Protocol for Slice-Aware RAT Selection

In our system model, the service requirements are characterized by a maximum tolerable vehicular blockage probability, a minimum SINR coverage probability, and a target rate coverage probability. As observed in Remark 2, Q_R can take values between 0 dB and a maximum value (say Q_B), which depends on λ_V . On the other hand, let the range of bias values that satisfy the SINR coverage probability constraint be given by (Q_{C1}, Q_{C2}) . Similarly, let the bias range that satisfies a target rate coverage probability be given by (Q_{R1}, Q_{R2}) .

We assume that for the QoS requirements of different slices, the network calculates the slice specific bias ranges $(1, Q_B)$, (Q_{C1}, Q_{C2}) , and (Q_{R1}, Q_{R2}) . For a given slice, and the associated bias range, the network computes and broadcasts the optimal bias value (Q_R^*), which in case of URLLC and mMTC services maximizes the SINR coverage, and in case of eMBB maximizes the data rate. Q_R^* is obtained using a random restart hill-climbing algorithm [45]

Algorithm 1 Network-Side Pseudo-code

Obtain the data about expected vehicular density in the service area. each slice of QoS triplet $(\mathcal{B}, \mathcal{P}_C, \mathcal{P}_R) \in \mathcal{T}$ Identify the set of biases $(0, Q_B)$ that satisfy \mathcal{B} , using (3.5). Identify the set of biases (Q_{C1}, Q_{C2}) that satisfy \mathcal{P}_C , using (3.12). Identify the set of biases (Q_{R1}, Q_{R2}) that satisfy \mathcal{P}_R , using (3.15). Obtain $Q_R^* \in (1, Q_B) \cap (Q_{C1}, Q_{C2}) \cap (Q_{R1}, Q_{R2})$ for maximizing \mathcal{P}_C in (3.12) if URLLC/mMTC slice, or for maximizing \mathcal{P}_R in (3.15) if eMBB slice, using random restart hill climbing. Broadcast Q_R^* within the slice.

Algorithm 2 UE-Side Pseudo-code

-
- 1: Measure downlink sub-6GHz received powers, $P_{tv\mu}$, from all BSs. $P_{Mv\mu1} \geq P_{Sv\mu1}$
 - 2: Request to be associated to the strongest MBS.
 - 3: Request to be associated to the strongest SBS and measure the mm-wave power from it ($P_{Sv\mu1}$). Obtain the RAT bias Q_R^* for the associated slice. $P_{Sv\mu1} \geq Q_R^* P_{Sv\mu1}$
 - 4: Request to be served from SBS in sub-6GHz band.
 - 5: Request to be served from SBS in mm-wave band.
-

such that $Q_R^* \in (1, Q_B) \cap (Q_{C1}, Q_{C2}) \cap (Q_{R1}, Q_{R2})$. When a UE associates to an SBS, it receives the bias value depending on its slice and uses it for the RAT selection procedure. In the next section, we will show how the mm-wave association probability varies for the three types of slice. In Algorithms 1 and 2, we summarize our RAT selection strategies at network and UE sides, respectively.

3.8 Numerical Results

In this section, we provide some numerical results to reveal the salient characteristics of the network. We assume a MBS deployment density of $\lambda_M = 5 \text{ km}^{-2}$, and transmit powers $P_S = 30 \text{ dBm}$ and $P_M = 45 \text{ dBm}$. N_0 is assumed to be -174 dBm/Hz and the operating frequencies are 2.3 GHz and 60 GHz for sub-6GHz band and the mm-wave band, respectively, with the corresponding bandwidths being 20 MHz and 1 GHz. The Nakagami parameter is assumed to be $n_0 = 3$, the antenna beamwidth is assumed to be $\theta = 10^\circ$, and the relative height of the SBSs is assumed to be $h_B = 10 \text{ m}$. The path-loss parameters are derived from 3GPP reports [78, 36]. Finally, regarding the vehicles, we assume C-segment medium sized cars, with $h_V = 4.5 \text{ m}$ and $L_V = 1.5 \text{ m}$ [96].

3.8.1 Validation of the mm-Wave Interference and SINR Model

In Fig. 3.4, we compare the SINR coverage probability obtained with our analytical framework (see Theorem 1) with Monte Carlo simulations⁶. We observe that

⁶The final integral of (3.3) does not have a closed form. We simplify the evaluation by expanding the exponential term in the numerator, i.e., $\exp(-2\lambda_S \sqrt{x^2 - r^2})$, with a power series, and evaluating each of the resulting integral terms separately.

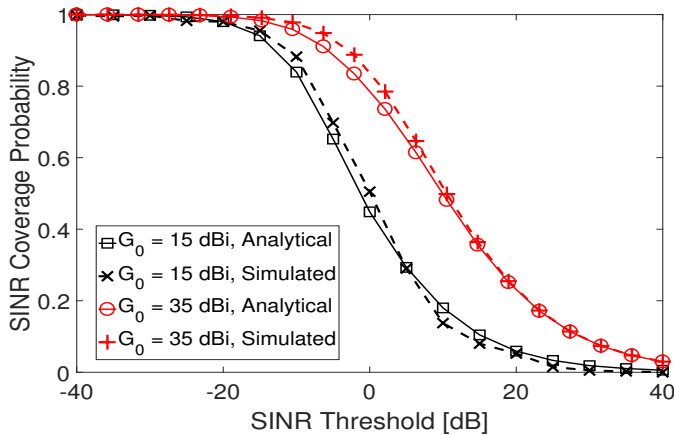
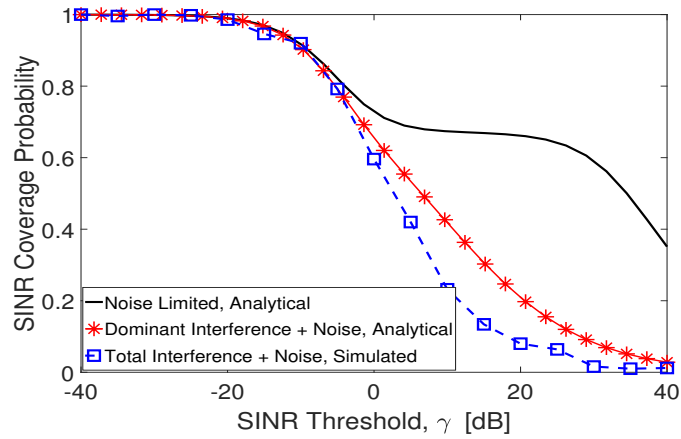


FIGURE 3.4: Validation of the model for users' SINR coverage probability with $\lambda_S = 100 \text{ km}^{-1}$.

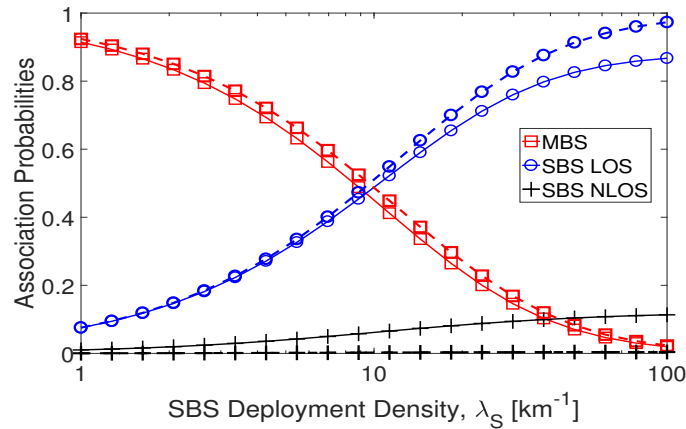
the analytical results agree with the simulations. Specifically, for $G_0 = 35 \text{ dBi}$, we see that the lower bound of Theorem 1 is very tight. In Fig. 3.5a, we use Monte Carlo simulations to compare the SINR coverage with only noise, only the dominant interferer (see Assumption 1), or the whole interference. We see that our dominant interferer model the statement is vague; try to be more precise, talking about low, medium, and high SINR or giving maximum gaps is sufficiently accurate to represent interference in mm-wave and that the noise limited model is unacceptable.

3.8.2 Association and RAT Selection Probabilities

In Fig. 3.5b, we plot the association probabilities for pedestrian users (see Proposition 4). As expected, as λ_S increases for a given λ_R , the LOS SBS association probability increases and the MBS association probability decreases. However, with increasing λ_S , the NLOS SBS association is fairly negligible except for very high road densities (e.g., $\lambda_R = 15 \text{ km}^{-1}$). In Fig. 3.6a, we plot the mm-wave selection probability with the *instantaneous power RAT selection* with respect to Q_R , given that the typical user has selected an LOS SBS (Proposition 5). Increasing either or both Q_R and G_0 facilitates an increase in mm-wave RAT selection. More interestingly, G_0 has a more pronounced effect on mm-wave selection than increasing the deployment density. For example, with $G_0 = 10 \text{ dBi}$ and $Q_R = 24 \text{ dB}$, doubling λ_S from 5 to 10 km^{-1} increases the mm-wave selection from 50% to 70%, whereas, setting $G_0 = 20 \text{ dBi}$ ensures 100% mm-wave RAT selection. Thus, an operator requiring aggressive mm-wave selection may prefer to invest in more efficient antennas rather than



(A)



(B)

FIGURE 3.5: (a) Validation of the model for users' SINR coverage probability with $\lambda_S = 100 \text{ km}^{-1}$, (b) Validation of the dominant interference model, $G_0 = 35 \text{ dBi}$, $\lambda_S = 100 \text{ km}^{-1}$ and (c) Association probabilities of the users with varying SBS density (solid lines correspond to $\lambda_R = 15 \text{ km}^{-1}$, dashed lines correspond to $\lambda_R = 5 \text{ km}^{-1}$).

increasing λ_S . Following Remark 1, we observe that with the *instantaneous power RAT selection*, in the presence of vehicles, \mathcal{P}_m saturates to a value less than 1. On the contrary, the *averaged power RAT selection* (see Lemma 5) has a greater RAT tunability (as shown in Fig. 3.6b), and enables to increase the mm-wave selection probability. However, increased measurement duration may lead to higher access delay, which is a tradeoff we aim to study in future works. In the following, we perform our analysis using the instantaneous power RAT selection.

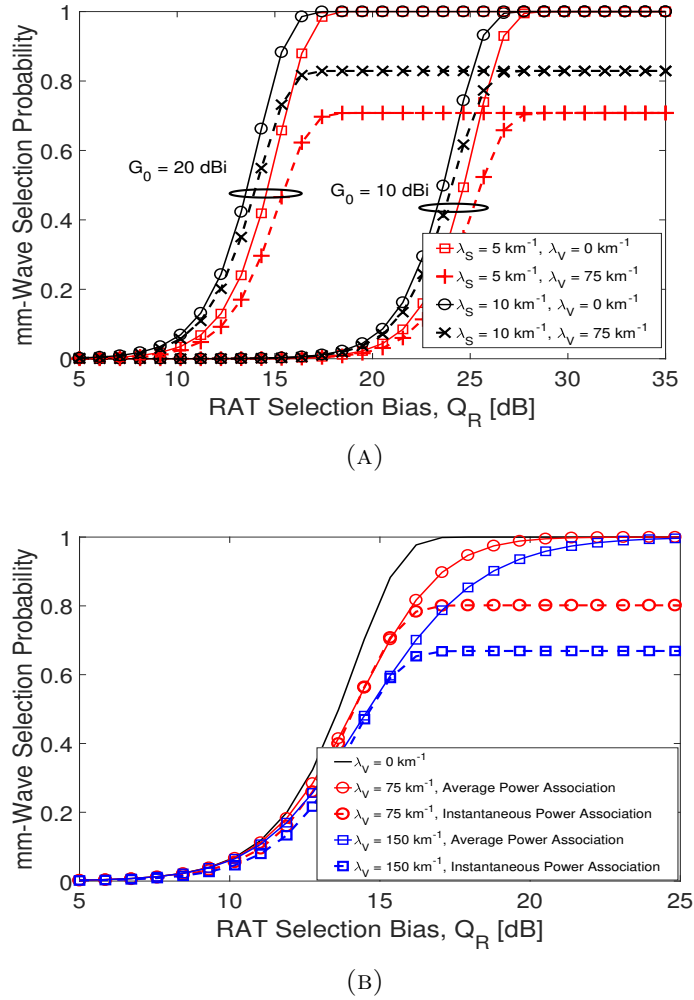


FIGURE 3.6: (a) Conditional mm-wave selection probability with RAT selection bias, (b) Comparison of different schemes of RAT selection, $G_0 = 20$ dBi and $\lambda_S = 10 \text{ km}^{-1}$.

3.8.3 SINR Coverage Probabilities

In Fig. 3.7a, we plot the SINR coverage probability (Theorem 1). With $G_0 = 10$ dBi and $Q_R = 0$ dB, in case of LOS SBS association, the user always selects sub-6GHz RAT, and. Moreover, we observe that increasing λ_R slightly decreases the SINR performance because the sub-6GHz interference increases. In the same way, the SINR enhancement in the sub-6GHz band achieved by increasing λ_S is fairly limited. In Fig. 3.7b, we plot the SINR coverage probability with respect to λ_S with fixed G_0 and Q_R to accurately observe this trend. For users operating only in sub-6GHz band, it may not be possible to maintain a desired SINR coverage in cities with dense roads by simply increasing λ_S . This is because a user perceives higher LOS interference, especially from the SBSs. Thus, it is necessary to offload users to the less interference-prone mm-wave

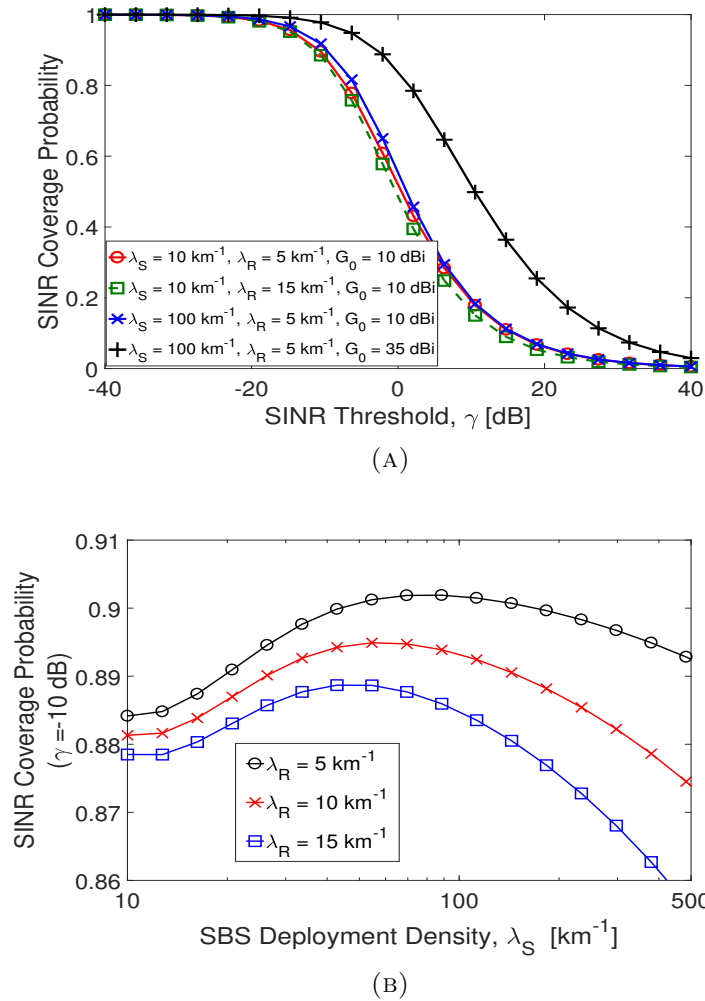
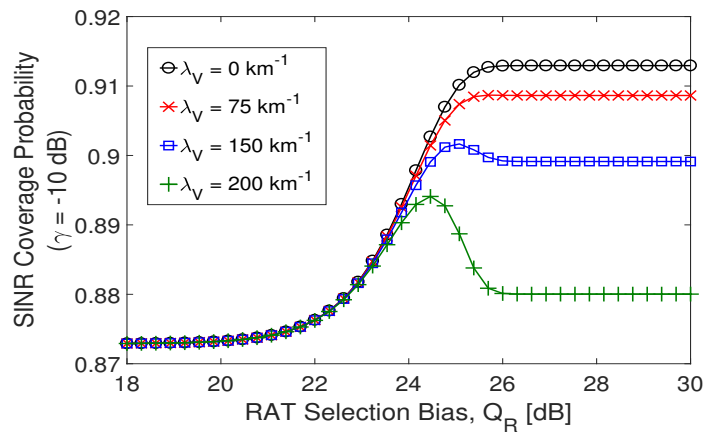


FIGURE 3.7: (a) SINR coverage probability of the users for different SBS deployment densities and road densities, (b) SINR coverage probability for the users at $\gamma = -10 \text{ dB}$ with respect to the SBS deployment density ($G_0 = 10 \text{ dBi}$, $Q_R = 0 \text{ dB}$).

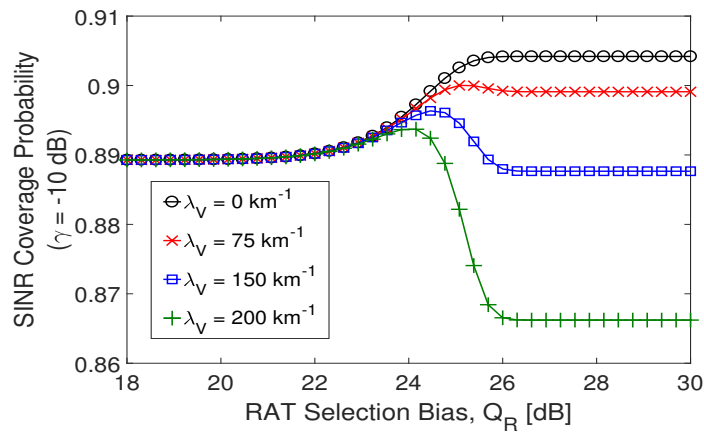
RAT to enhance the SINR in cities with dense roads. Clearly, increasing the mm-wave selection probability (with $G_0 = 30 \text{ dBi}$) enhances the SINR (see Fig. 3.7a). However, in the following section we will see that, in presence of vehicular blockages and for sparse SBS deployments, the SINR in mm-wave band can be worse than the one perceived in the sub-6GHz band.

3.8.4 Slice-Aware RAT Selection

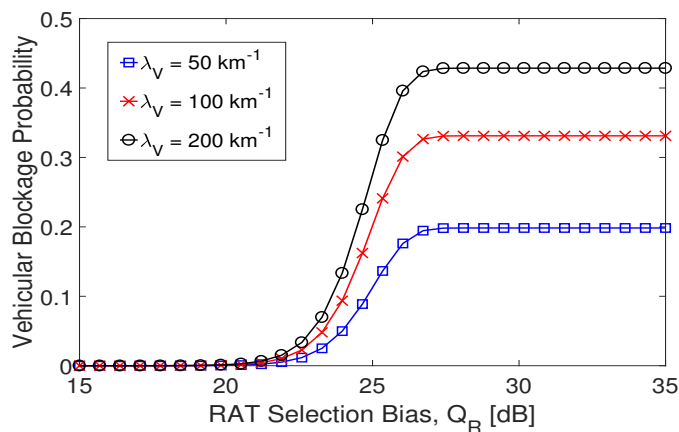
In this section, first, we discuss the effect of Q_R on the network performance, and accordingly, reveal the intuition behind the choice of the slice-aware RAT biasing.



(A)

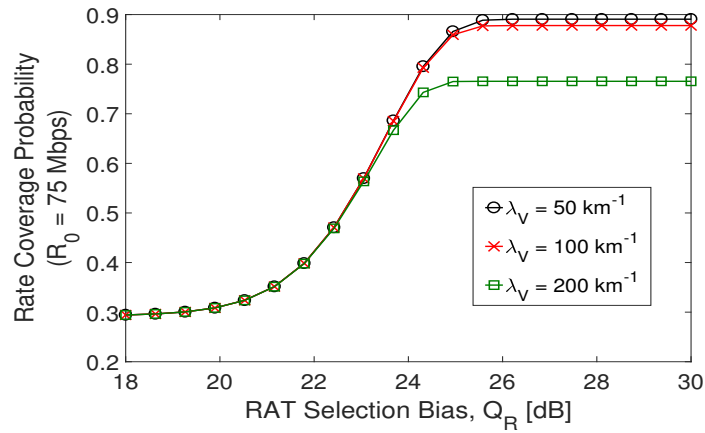


(B)

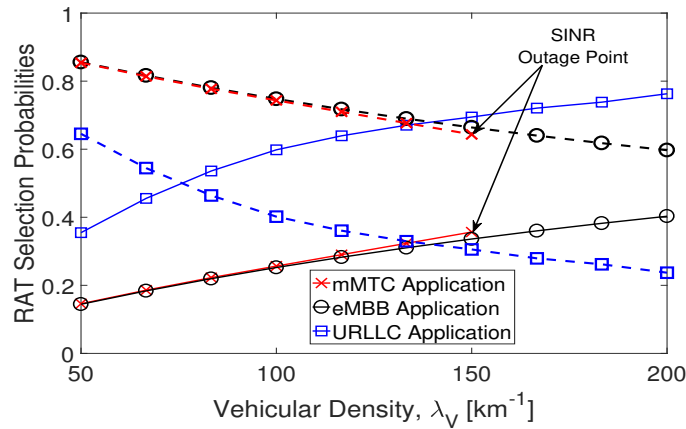


(C)

FIGURE 3.8: SINR coverage probabilities for the users with varying RAT selection bias with $G_0 = 10$ dBi for different vehicular blockage densities, (a) $\lambda_S = 50 \text{ km}^{-1}$ and (b) $\lambda_S = 10 \text{ km}^{-1}$. (c) Vehicular blockage probability with respect to RAT selection bias given that the user is served with mm-wave RAT.



(A)



(B)

FIGURE 3.9: (a) Rate coverage probability for the user for different vehicular blockage densities, $\lambda_S = 10 \text{ km}^{-1}$ and (b) Slice-aware RAT selection probabilities for different use-cases, solid lines denote the sub-6GHz association probabilities and the dotted lines denote the mm-wave association probabilities respectively.

SINR Coverage

In Fig. 3.8, we plot the SINR coverage probability of the users at $\gamma = -10$ dB with varying Q_R for different vehicular blockage densities. We see that in the case where the roads are devoid of vehicles, the SINR coverage probability increases with Q_R for both dense (Fig. 3.8a) and sparse (Fig. 3.8b) deployment of SBSs, precisely due to the combined effects of LOS mm-wave signals and minimal interference in the mm-wave band.

As the λ_V increases (from 75 to 200 km^{-1}), aggressive mm-wave policy deteriorates the SINR coverage. As a result, for a given vehicular density in an urban area, there exists an optimal RAT selection bias that maximizes the

SINR coverage. More interestingly, in Fig. 3.8b, we observe that in case of sparse deployments ($\lambda_S = 10 \text{ km}^{-1}$), with very dense vehicular traffic ($\lambda_V = 200 \text{ km}^{-1}$), higher biases decreases the system coverage. Thus, corresponding to a required threshold \mathcal{P}_C^* , the operator should select the RAT bias value from a range (Q_{C1}, Q_{C2}) .

Vehicular Blockage

In Fig. 3.8c, we plot the vehicular blockage probability with varying Q_R . We observe that as Q_R increases, the blockage increases, due to the increased number of users served in the mm-wave band, which is prone to the vehicular blockage. Thus, users running URLLC applications will necessarily need to operate below a bias threshold (say Q_B) governed by the current λ_V .

Rate Coverage

From Fig. 3.9a, we see that the rate coverage increases with Q_R even in the case of high λ_V (even though the SINR coverage decreases, see Fig. 3.8a). This is due to the large bandwidth in the mm-wave band that compensates for the loss in SINR. However, operating at biases that result in very low SINR would result in service outage. As a result, it is necessary to optimize Q_R with respect to the data rate while satisfying the SINR constraints.

Slice-Aware RAT Selection

To give a better insight to the bias selection scheme, we illustrate our RAT selection protocol with three examples: 1) A slice for a URLLC service with $T^* = (0.001, 0.85, 0)$, 2) A slice for an mMTC service with $T^* = (0.1, 0.9, 0)$, and 3) A slice for an eMBB service with $T^* = (0, 0.85, 0.7)$. We assume a network with $\lambda_S = 10 \text{ km}^{-1}$, $\lambda_R = 15 \text{ km}^{-1}$, and $G_0 = 15 \text{ dBi}$.

For example 1, \mathcal{B}^* is 0.1%, which results in $Q_R^* = 19.7 \text{ dB}$. This leads in a lower mm-wave selection probability (see Fig. 3.9b) as compared to the other applications. As the vehicular density increases, the maximum allowable Q_R to satisfy the vehicular blockage constraint gradually decreases, thereby further decreasing the mm-wave selection probability.

For example 2, the \mathcal{B}^* is less stringent (10%), whereas \mathcal{P}_C^* is tighter (outage constraint equal to 10%). In case of low λ_V (e.g., 50 km^{-1}), the optimized bias is $Q_R^* = 25 \text{ dB}$, which achieves an SINR coverage of more than 91%, with a mm-wave selection of over 80%. This is considerably higher than the URLLC

applications. However, for $\lambda_V \geq 150 \text{ km}^{-1}$, no feasible bias exists to satisfy the outage constraint, and the application cannot be supported with current network dimensioning. The vehicular density value after which the network is not able to sustain outage below 10% is shown in Fig. 3.9b.

Finally, for example 3, the eMBB service does not have any vehicular blockage constraints. Thus, the operating bias for eMBB applications aims to maximize the rate coverage probability while satisfying the outage constraint (here 15%). For $\lambda_V = 50 \text{ km}^{-1}$, the optimized operating bias ($Q_R^* = 26.21 \text{ dB}$) results in a slightly higher mm-wave selection probability than the mMTC application. As the vehicular traffic increases, the optimal bias value decreases (see Fig. 3.9b). However, as the outage constraint is not as stringent as the mMTC application of example 2, the user can be served even under very high vehicular densities (e.g., $\lambda_V = 200 \text{ km}^{-1}$).

3.8.5 System Design Insights

Finally, we outline the system design and dimensioning insights based on our results:

- In case the operator needs to prioritize mm-wave association for high-data rate services so as to free the sub-6GHz RAT for reliability specific applications, it needs to deploy more SBSs per road in a city with more roads. However, excessive deployment of SBSs degrades the SINR performance of the users. Thus, proper care must be taken of this tradeoff while dimensioning the cellular network.
- For aggressively offloading the users to mm-wave, increasing the directivity gain of the antenna is a more efficient mechanism than deploying more SBSs due to the deployment costs. However, in case of presence of vehicles, the mm-wave association saturates. This effect can be reduced by adopting an *averaged power RAT selection* instead of a more *instantaneous power RAT selection* at the cost of an increased access delay.
- Having a network-wide RAT selection bias will not be able to support a diverse plethora of applications. Hence, slice-aware RAT selection becomes necessary. For URLLC services, there exists a threshold of bias beyond which the blockage of the service becomes intolerable. For applications that require high SINR on the contrary, e.g., mMTC, there exist non-trivial biases that maximize the SINR.

- The bias values that maximize the downlink data rate may lead to excessive outage, and hence, we provided optimal bias values for rate coverage under outage constraints. If the operator wants to increase the rate coverage even further, e.g., for eMBB applications, it is important to develop efficient interference management mechanisms as increasing the deployment density simply degrades the SINR performance.

3.9 Chapter Conclusions

In this chapter, we have characterized a multi-tier network operating in multiple radio bands. We have provided realistic characterizations of the mm-wave interference and effect of vehicular blockage on the mm-wave RAT. First, from the perspective of the pedestrian users, we have analyzed the effect of the RAT selection bias on the mm-wave blockage, SINR coverage, and rate coverage probability under different vehicular densities. Accordingly, we have provided a slice-aware RAT selection strategy to jointly support URLLC, mMTC, and eMBB applications in future mm-wave sliced 5G networks. Finally, we have highlighted several key system design insights for an operator that aims to optimally serve a diverse variety of services.

Part II

Joint Communication and Localization Service in mm-Wave Networks

Chapter 4

Positioning Data-Rate Trade-off in mm-wave Small Cells and Service Differentiation for 5G Networks

4.1 Introduction

To address the multi-fold increase in the demand for data rates, exploitation of higher frequency spectrum in the mm-wave range is gaining popularity [23]. However, mm-wave communication is characterized by high path loss and sensitivity to blockages. To solve these problems, beam-forming techniques are utilized with the help of highly directional antennas, which result in new issues in terms of coverage and initial access [41]. Moreover, beam-alignment errors between the BSs and the UEs degrade the communication performance. One solution to this problem consists of enabling UEs to simultaneously receive signals in the mm-wave and in the sub-6GHz band, and to use the latter to support the initial access on the mm-wave band [45]. Another approach exploits positioning algorithms to support the UE cell discovery and access to mm-wave BSs. On the one hand, with fine-tuned positioning, the beam-alignment procedure is quickened, and beamforming and user tracking are improved [97]. On the other hand, improved mm-wave beam-forming can be used for more accurate localization and orientation of nodes [24].

In addition to the high speed data rates, the 5G cellular networks anticipate an explosion of new services, characterized by heterogeneous requirements. We

investigate a mm-wave network deployed for supporting positioning and broadband functionalities simultaneously, e.g., in vehicle-to-infrastructure communication. Specifically, we study the trade-off between positioning efficiency and downlink data rates and accordingly, we prescribe the operator an algorithm to tune the mm-wave BS transmit power so as to meet specific QoS requirements of different services.

4.1.1 Related Work

In the context of sub-6GHz systems, Jeong et al. [98] have studied a distributed antenna system providing both data communication and positioning functionalities. The authors assumed that the UEs know the positions of the BSs and attempt to estimate their own positions based on the received signals. Lemic et al. [99] have shown that localization using mm-wave frequencies is efficient in terms of accuracy, even in the presence of a limited number of anchor nodes. In fact, mm-wave beam-forming allows for accurate localization and orientation of UEs with respect to the BSs [24]. Garcia et al. [97] have studied a location-aided initial access strategy for mm-wave networks, in which the information of UE locations enables to speed up the channel estimation and beam-forming procedures. Destino et al. [24] have studied the trade-off between communication rate and positioning quality in a single user mm-wave link. Similarly Koirala et al. [58] have studied the beamforming optimization and spectral power allocation based on theoretical localization bounds.

The downlink communication performance in random wireless networks is typically characterized by SINR coverage probability and rate coverage probability, using stochastic geometry [69]. For this, the positions of the BSs are modeled using homogeneous PPP [73] or using repulsive point processes [86]. Recently, Ghatak et. al. [100] investigated a more realistic scenario, where mm-wave BSs are deployed along the roads of a city. We use this model in this chapter, and accordingly we study a one dimensional setting where the BSs and the served users are assumed to be on the same street.

Specifically, leveraging on the tools of stochastic geometry, we present an average characterization of the localization and communication performance of this network, by exploiting the a-priori knowledge about the distribution of the distances of the users from the BSs. We analyze the positioning and data communication trade-off, and provide the operator with a power control

scheme designed to satisfy distinct QoS requirements of the positioning and the communication functions.

4.1.2 Contributions and Organization

The main contributions of this chapter are:

- We characterize a noise-limited mm-wave system designed to support positioning and broadband services simultaneously by partitioning the BS transmit power. First, we obtain the CRLB for the estimation of the distance of a typical UE from its serving BS. Subsequently, we obtain the signal to noise ratio (SNR) and rate coverage probability of the typical user, as a function of the power splitting factor.
- Leveraging on the derived CRLB for the estimation of the distance, we obtain an upper bound on the probability of beam-selection error. Based on this, we compute the minimum antenna beamwidth that limits the beam-selection error.
- Finally, we analyze the trade-off between the positioning and the data rate performance of the typical user. Accordingly, we prescribe the operator with a scheme to select the proper power splitting factor to support different QoS requirements. Specifically, we study our mm-wave system under different operating beamwidths, and analyze the distribution of the total transmit power for maximizing either the positioning efficiency or the UE data-rate.

The rest of the chapter is organized as follows. In Section D.2, we introduce our system model and outline the performance objectives. In Section D.3, we derive our main results on the positioning error, the rate coverage, and the beam-selection error. We provide some numerical results in Section 4.4, and accordingly present our power partitioning scheme. Finally, the chapter concludes in Section 4.5.

4.2 System Model

We consider an urban scenario, with multi-storied buildings that result in a dense blocking environment. In this scenario we analyze a mm-wave network consisting of BSs deployed along the streets of the city.

4.2.1 Network Geometry

The positions of the BSs in each street are modeled as points of a one-dimensional Poisson point process (PPP) ϕ , with intensity λ [m^{-1}]. Each BS is assumed to be of known height h_B and equipped with directional antennas with beamwidth θ . Let the corresponding product of the directivity gains of the transmitting and receiving antennas be G_0 . The transmit power of the BSs is assumed to be P . Without loss of generality we perform our analysis from the perspective of a typical user located at origin, which associates with the BS that provides the highest downlink power. Accordingly, the distribution of the distance d of the typical user from the serving BS is given by [52]:

$$f_d(x) = 2\lambda \exp(-2\lambda x) \quad (4.1)$$

Furthermore, we assume that the network is equipped with efficient interference management capabilities (e.g., spatio-temporal frequency reuse), so that the performance of the users is noise-limited¹.

4.2.2 Path-loss

Due to the low local scattering, we consider a Nakagami fading for mm-wave communications [102] with parameter n_0 and variance equal to 1. Furthermore, we assume a path loss model where the power at the origin received from a BS located at a distance d is given by $P_r = K \cdot P \cdot g \cdot G_0 \cdot (d^2 + h_B^2)^{-\frac{\alpha}{2}}$, where K is the path loss coefficient, g represents the fast-fading, and α is the path loss exponent. Thus, the average SNR can be written as $\frac{K \cdot P \cdot G_0 \cdot (d^2 + h_B^2)^{-\frac{\alpha}{2}}}{N_0 \cdot B}$. N_0 and B are the noise power density and the operating bandwidth, respectively.

4.2.3 Transmission Policy

We assume a communication scheme where the transmit power of the BSs is divided into two parts: one associated with positioning and the other allotted for data communication. The power allocated for localization determines the number of control symbols used for this function, whereas the remaining power is utilized for control and data symbols of the communication phase. We acknowledge that it is possible to utilize the native communication signal for

¹Although the assumption of the network being noise-limited simplifies the analysis, Singh et al. [101] have shown the validity of this assumption in outdoor mm-wave mesh networks. In a future work, we will extend the analysis by considering interfering BSs.

positioning services. However, we use dedicated waveforms designed for better localization performance (e.g., see [103] for a discussion on localization specific waveforms). Hence, splitting of the transmit power becomes necessary to characterize and optimize the operating trade-off between communication and localization functionalities. Accordingly, if the total transmit power is P , and β is the fraction of power used for data services, the corresponding transmit power for localization is $P_L = (1 - \beta)P$. Consequently, the transmit power for data service is $P_D = \beta P$. Let the SNR for the distance estimation and the data communications phases be represented by SNR_1 and SNR_2 , respectively.

4.3 Positioning Error, Data Rate Coverage and beam-selection error

In this section, we first characterize the minimum variance of the error in the estimation of the distance of the typical user from the serving BS. Then, we derive the SNR coverage and the rate coverage probabilities.

4.3.1 Distance Estimation Analysis

To simplify our analysis, we only consider the effect of the distance on the power of the received signal (for instance, we consider RSSI based ranging algorithms), and ignore the effect of the distance on the phase [104]. Accordingly, the received signal is:

$$y(t) = \frac{\sqrt{KG_0P_L}}{(h_B^2 + d^2)^{\frac{\alpha}{4}}} x(t) + n(t), \quad (4.2)$$

where $n(t)$ is a zero mean additive white Gaussian noise resulting in estimation errors.

Lemma 19. *The expected value of the Fisher information for the estimation of the distance (d) is calculated as:*

$$J_D = \frac{KG_0P_L2\lambda\bar{f}^2}{\sigma_N^2} \int_1^\infty \frac{e^{-2\lambda x}}{(h_B^2 + x^2)^{\frac{\alpha}{2}}} dx, \quad (4.3)$$

where $\bar{f}^2 = 1.25\pi^2B^2$. Furthermore, the prior information is: $J_p = \log(2\lambda) - 1$.

$$J_D = \frac{KG_0P_L2\lambda\bar{f}^2}{\sigma_N^2} \frac{i(e^{-i2\lambda h_B} Ei(i2\lambda h_B)) - e^{i2\lambda h_B} Ei(-i2\lambda h_B)}{2h} + 2\lambda \log(2\lambda) - 1 \quad (4.6)$$

Proof. The Fisher information for a given d is [63]:

$$J_d = \frac{KG_0P_L}{(h_B^2 + d^2)^{\frac{\alpha}{2}} \sigma_N^2} \bar{f}^2, \quad (4.4)$$

where $\bar{f}^2 = \frac{\int_{-\infty}^{\infty} (2\pi f)^2 |X(f)|^2 df}{\int_{-\infty}^{\infty} |X(f)|^2 df}$ is the effective bandwidth of the signal. In our case, we assume that the signal has a flat spectrum [24], and accordingly, we have $\bar{f}^2 = 1.25\pi^2 B^2$. Now using the distribution of d from (5.1), the expectation of the Fisher information is calculated as:

$$J_D = \mathbb{E}_d [J_d] = \frac{KG_0P_L2\lambda\bar{f}^2}{\sigma_N^2} \int_1^{\infty} \frac{e^{-2\lambda x}}{(h_B^2 + x^2)^{\frac{\alpha}{2}}} dx. \quad (4.5)$$

Finally, the prior information can be calculated as:

$$\begin{aligned} J_p &= \mathbb{E} [\log(f_d(x))] = \int_0^{\infty} \log(f_d(x)) f_d(x) dx \\ &= \int_0^{\infty} \log(2\lambda \exp(-2\lambda x)) 2\lambda \exp(-2\lambda x) dx \\ &= \log(2\lambda) - 1 \end{aligned}$$

This completes the proof. □

Corollary 3. *For the special case of path loss exponent $\alpha = 2$, J_D evaluates to (4.6), where Ei is the EI [105].*

Finally, the Bayesian information can be obtained as $J_B = J_D + J_P$. Consequently, the BCRLB and Jeffrey's prior corresponding to the Bayesian information are calculated as $\frac{1}{J_B}$ and $\sqrt{J_B}$, respectively.

Remark 3. *Intuitively, higher the Jeffrey's prior (or lower the BCRLB) is, better the estimation efficiency will be. From (4.6), we see that a higher Jeffrey's prior is facilitated by a larger value of P_L , i.e., a smaller β .*

$$\mathcal{P}_C(\gamma) = \sum_{n=1}^{n_0} (-1)^{n+1} \binom{n_0}{n} 2\lambda \exp\left(2\lambda - \frac{h_B^2 n \gamma \sigma_N^2}{P_D K G_0}\right) \left[\frac{\sqrt{\pi}}{2} \left(\sqrt{\frac{P_D K G_0}{n \gamma \sigma_N^2}} - \frac{P_D K G_0}{n \gamma \sigma_N^2} \operatorname{erf}\left(\frac{h_B^2 n \gamma \sigma_N^2}{P_D K G_0}\right) \right) \right] \quad (4.7)$$

4.3.2 Coverage and Rate Analysis

Based on the path-loss model of Section II-B, the SNR for the communication phase at a distance d is:

$$\text{SNR}_2 = \frac{P_D K g G_0}{\sigma_N^2} (d^2 + h_B^2)^{-\frac{\alpha}{2}}.$$

Accordingly, let us define the SNR coverage probability of the typical user at a threshold γ , as the probability that the SNR is greater than γ . It represents the fraction of the users under coverage in the network.

Lemma 20. *The SNR coverage probability at a threshold of γ is calculated as (4.7).*

Proof. The SNR coverage probability is computed as follows (where $d := x$):

$$\begin{aligned} \mathbb{P}(\text{SNR}_2 \geq \gamma) &= \mathbb{P}\left(\frac{P_D g K G_0}{\sigma_N^2} (\sqrt{x^2 + h_B^2})^{-\alpha} \geq \gamma\right) \\ &= \mathbb{P}\left(g \geq \frac{\gamma \sigma_N^2}{P_D K G_0 (x^2 + h_B^2)^{-\frac{\alpha}{2}}}\right) \\ &= \sum_{n=1}^{n_0} (-1)^{n+1} \binom{n_0}{n} \mathbb{E}\left[\exp\left(-\frac{n \gamma \sigma_N^2}{P_D K G_0 (x^2 + h_B^2)^{-\frac{\alpha}{2}}}\right)\right] \\ &= \sum_{n=1}^{n_0} (-1)^{n+1} \binom{n_0}{n} 2\lambda \int_0^\infty \exp\left(-\frac{n \gamma \sigma_N^2 (x^2 + h_B^2)^{\frac{\alpha}{2}}}{P_D K G_0}\right) \\ &\quad \exp(-2\lambda x) dx \end{aligned}$$

Evaluating this integral completes the proof. \square

Similar to the SNR coverage probability, the rate coverage probability at a threshold r_0 is defined as the probability that the downlink data rate of the typical user is greater than r_0 .

Corollary 4. *The rate coverage probability can be computed as:*

$$\begin{aligned} \mathcal{P}_R(r_0) &= \mathbb{P}(R \geq r_0) = \mathbb{P}\left(\text{SNR}_2 \geq 2^{\frac{r_0}{B}} - 1\right) \\ &= \mathcal{P}_C\left(2^{\frac{r_0}{B}} - 1\right) \end{aligned} \quad (4.8)$$

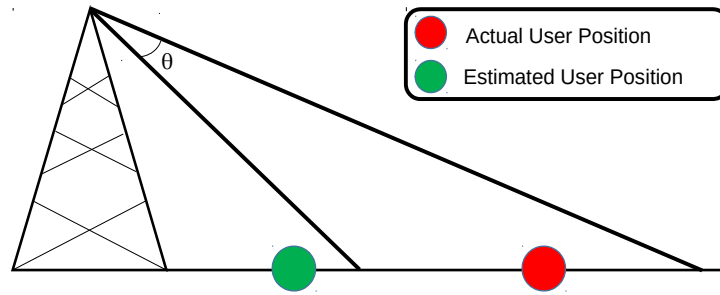


FIGURE 4.1: Illustration of the beam-selection error.

4.3.3 Beam Selection Error

A BS with an antenna beamwidth θ , serving a user located at distance d , covers a region of length D_0 on the ground (see Fig. 1). Using simple trigonometric calculations, we have:

$$D_0 = \frac{2 \tan\left(\frac{\theta}{2}\right) \left[1 + \frac{d^2}{h_B^2}\right]}{1 - \frac{d^2}{h_B^2} \tan^2\left(\frac{\theta}{2}\right)}.$$

Once the localization procedure and the corresponding exchange of user-BS control signals is performed, beam-selection error can occur in the absence of dynamic beam-alignment on both sides of the radio link. Assuming that the user's antenna is always oriented towards the BS, or equivalently in case the user is operating with an omni-directional antenna, beam-selection error will occur in case the distance of the user on the ground is more than $\frac{D_0}{2}$ from the estimated position.

Let us assume that the estimation error for the UE localization is symmetric about its mean. Consequently, we bound the probability of the beam-selection error as follows:

Lemma 21. *The probability of beam-selection error for a user located at a distance d from the serving BS is bounded as $\frac{BCRLB}{D_0}$.*

Proof.

$$\mathcal{P}_{MA}(d) = \mathbb{P}\left(|d - \hat{d}| \geq \frac{D_0}{2}\right) \stackrel{(a)}{\leq} \frac{2\sigma^2}{D_0} \stackrel{(b)}{=} \frac{2 \cdot BCRLB}{D_0}, \quad (4.9)$$

where \hat{d} is the estimated distance of the user. Here (a) follows from Markov's inequality assuming σ^2 as the variance of the positioning error. The step (b) occurs for an minimum-variance unbiased estimator (MVUE). \square

Corollary 5. *The mean beam-selection error is then bounded by taking the expectation over d , i.e., $\bar{\mathcal{P}}_{MA} = \mathbb{E}_d [\mathcal{P}_{MA}(d)] \leq \mathbb{E}_d \left[\frac{2 \cdot BCRLB}{D_0} \right]$.*

In the next section, we prescribe guidelines for an operator to choose an operating beamwidth for limiting this error.

4.4 Numerical Results and Discussion

In this section, we present some numerical results based on the analytical framework presented in this chapter. First, we show how the SNR coverage probability changes with the power splitting factor (β). Subsequently, we study the trade-off between localization and data rate as a function of β . Then, with the help of two examples, we describe our power partitioning scheme. In the following analysis, we assume $G_0 = 10$ dB and $n_0 = 3$.

4.4.1 SINR Coverage Probability

In Fig. 4.2 we plot the SNR coverage probability with respect to β at a threshold of $\gamma = -10$ dB. As β increases, the SINR coverage probability increases due to more power allocated to the data transmission phase. This provides a guideline to select a minimum operating β for a given deployment density, such that the outage is limited. As an example, to limit a service outage below 20%, with a BS deployment of 1 km^{-1} and a power budget of $P = 25$ dBm, the minimum β is 0.15, whereas with a power budget of $P = 20$ dBm, the minimum β is 0.5.

More interestingly, this analysis provides the operator dimensioning rules in terms of the deployment density of the BSs for a given power budget. For example, in order to support services with an outage tolerance of 10%, with a power budget of 20 dBm, a deployment density of 1 km^{-1} does not suffice, and the operator must necessarily deploy more BSs.

4.4.2 Beam-Selection Error

In Fig. 4.3 we plot the mean beam-selection error bound with respect to the beamwidth of the transmit antenna of the BSs. As expected, the larger the beamwidth and the higher the SNR, the lower the beam-selection error. For example, for a tolerable beam-selection error of 0.02% with SNR = -15 dB and $\lambda = 5 \text{ km}^{-1}$, the minimum antenna beamwidth should be 8 degrees.

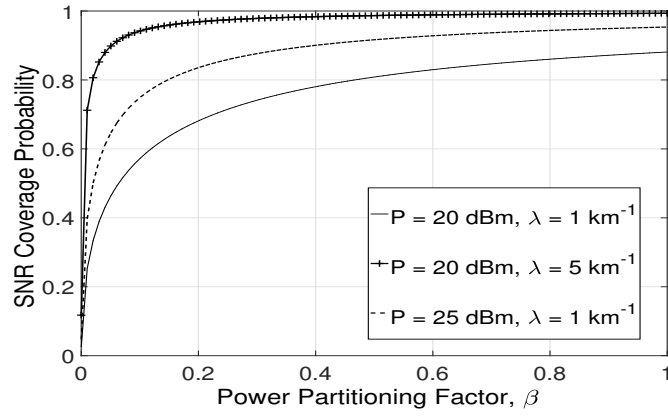


FIGURE 4.2: SNR coverage probabilities for a threshold of $\gamma = -10$ dB vs the fractional power split for different λ .

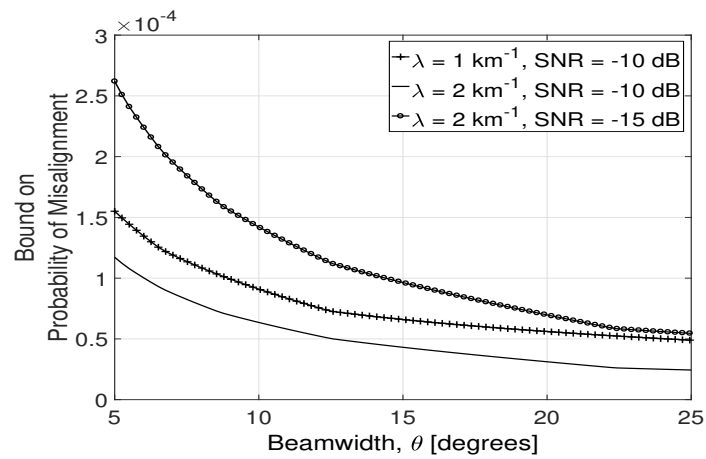


FIGURE 4.3: Beam beam-selection error with respect to beamwidth of the transmit antenna.

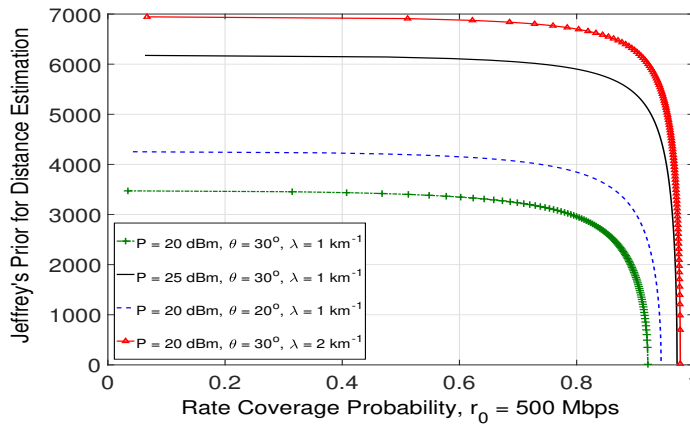


FIGURE 4.4: Distance estimation error vs physical data rate for different power budget.

4.4.3 Distance Estimation-Data Rate Trade-off

In Fig. 4.4 we plot the trade-off between the efficiency of the distance estimation of the user, represented by its Jeffrey's prior² and the rate coverage probability at a rate threshold of 500 Mbps. Each position in the plot for a given deployment parameter corresponds to a particular β . Thus for a given power budget, deployment density, and operating beamwidth, the performance of the system is determined by a particular operating characteristic, i.e., a trade-off between the positioning efficiency and data rate performance. For a particular operating characteristic, as we increase β , we improve the rate coverage probability at the cost of degrading the localization efficiency; whereas, decreasing β has the opposite effect. Accordingly, there exists a trade-off between the distance estimation and the data rate performance of the system. In the next subsection, we propose a scheme for selecting β based on a given operating beamwidth.

4.4.4 QoS Aware Network Parameter Setting

We propose the following scheme for setting the network parameters. First, for a given power budget, deployment density and operating beamwidth, the corresponding operating characteristic (i.e., a trade-off curve from Fig. 4.4) is selected. Next, for the chosen operating characteristic, the minimum β_{min} is chosen to satisfy the required outage constraint. Then, for a given positioning error constraint, the maximum value of β , i.e., β_{max} is selected. Finally, the operating $\beta_{min} \leq \beta \leq \beta_{max}$ is selected to address the specific QoS requirements.

²The estimation error is calculated as the inverse of the Jeffrey's prior.

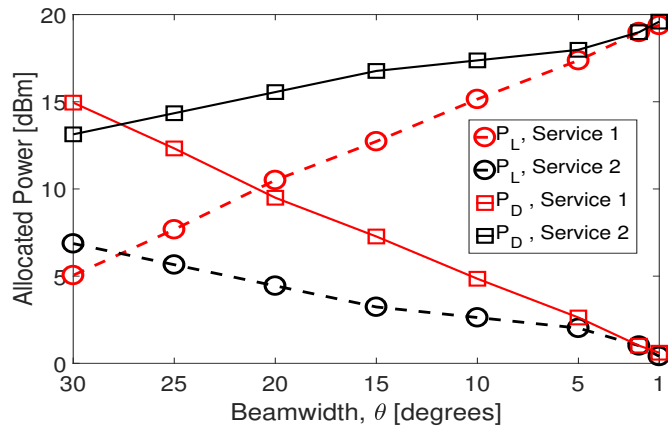


FIGURE 4.5: Power allocation for the two services.

Accordingly, the beam-selection error varies for the chosen β and the operating θ .

In what follows, we explain the total power distribution based on the QoS requirements, for a varying degree of beam-selection error. We assume a network with $\lambda = 2 \text{ km}^{-1}$ and a BS power budget of $P = 20 \text{ dBm}$ providing two services:

- Service 1 requires maximum positioning efficiency and a tolerable outage of 10%.
- Service 2 requires maximum data-rate and a tolerable positioning error of $5\text{e-}4 \text{ m}$.

We study the power partitioning scheme under different operating beamwidths. In practice, the operating beamwidth may be a system requirement for the first generation mm-wave networks. Intuitively, for a less stringent beam-selection error requirement, the operating beamwidth can be smaller. This can either be exploited to improve the positioning or enhance the data-rate, as per the required QoS.

For service 1, the operator should set β equal to the β_{min} corresponding to the θ that satisfies the beam-selection error requirement. Then, if the operating θ can be decreased, more power can be allotted for positioning and the one used for data communication $P\beta_{min}$ is reduced, accordingly. On the other hand, the operator should set β equal to the β_{max} corresponding to the θ that satisfies the beam-selection error requirement. Therefore, a thinner beamwidth facilitates larger power allocation for data communication (P_D increases). The stark difference in the two examples lies in the fact that the advantage of operating with a thinner beamwidth is exploited differently. With decreasing θ ,

for a positioning service, P_L increases and P_D decreases, whereas the opposite is true for the high data-rate services (see Fig. 4.5).

It is worth mentioning that the inter-dependence of β and θ for controlling the positioning performance and the beam-selection error is not trivial. As an example, for a required beam-selection error constraint or for a required positioning error constraint, there exist non-unique (θ, β) pairs. Furthermore, it may happen that for a given θ and P , no feasible β exists that satisfies the positioning and beam-selection error constraints simultaneously, thereby necessitating a higher BS power budget. This interesting trade-off and the associated optimization problem will be treated in a future work.

4.5 Chapter Conclusion

In this chapter we characterized a mm-wave system deployed to support positioning and broadband services simultaneously. Specifically, we introduced a power-partitioning based mechanism that enables the mm-wave BS to satisfy different localization and data-rate requirements. In this context, we derived dimensioning rules in terms of the density of BSs required to limit outage probability. Then, we provided the operator with a beamwidth selection guideline to limit the beam-selection error probability. Finally, we studied the trade-off between the localization efficiency and the downlink data rate, and consequently, presented a scheme for partitioning the transmit power depending on the service requirements.

Chapter 5

Throughput Characterization and Beamwidth Selection for Positioning-Assisted mm-wave Service

5.1 Introduction

To fulfill the ever growing demand for low latency high data rates, the high frequency mm-wave technology has been envisaged to be the backbone for the 5G of wireless communication systems [23]. mm-wave has been touted to supplement the aforementioned demands banking on the possibility of using unlicensed channels at high frequency (30 to 300 GHz) and large available bandwidths. However, operating at such a high frequency, mm-wave is inherently characterized by severe pathloss and higher susceptibility to blockages [106]. To overcome these challenges, beamforming and beam steering, with directional antennas, have been identified and adopted in the literature as a possible solution [107], but beam-alignment issues within the highly directional beamforming context further results into problems regarding coverage and initial access [41], [42].

To solve these issues, it is necessary to efficiently establish a good directional link between the transmitter and the receiver with beamforming and to this, the beamformer would benefit from the knowledge of the propagation channel and the location of the user. Hence, precise localization of the user is not only an add-on feature but a key requirement alongside communication in the context of mm-wave [108]. Most of the works in mm-wave localization domain has been dedicated to characterization of theoretical performance bounds. Typically, the CRLB has been considered regarding estimated channel parameters such as

delay, angle of departure (AoD), AoA and the channel coefficients so far [61], [62], [24]. With the help of these bounds, [109] and [58] have formulated the optimal beamforming problem assuming an a priori known user position.

Likewise, considering downlink communications, the earlier works in mm-wave band focus on the characterization of the SINR coverage probability [69]. With regards to the beam alignment, the authors in [41] investigate the exhaustive beam search method for initial access concluding that the high search overhead adversely affects the throughput performance. In [24], the authors investigate the throughput in mm-wave network based on localization performance bounds based beam alignment.

In this chapter, we consider a one-dimensional scenario with mm-wave BSs and the users deployed along the roads of a city like in [90]. Specifically, in this setting, we investigate the effect of beamwidth on the throughput of the user. Although using a smaller beamwidth with high directivity would provide a high throughput to the user, there is also a higher probability of no coverage at the user. On the contrary, a larger beamwidth would increase the coverage probability at the cost of reduced throughput available at the user. We thus analyze the tradeoff between the energy allocated for localization and communication to provide the selection criteria for the optimal beamwidth.

5.2 System Model

In this chapter, we consider an urban scenario with dense BSs deployed along the streets of a city with tall buildings contributing to a dense blocking environment.

5.2.1 Network Geometry and BS Characteristics

We assume that the distribution of BS positions in each street are modeled as one-dimensional PPP ϕ with intensity λ [m^{-1}]. We assume a LOS ball model similar to [69] for the BS process with a radius d_s . Without loss of generality we perform our analysis from the perspective of a typical user located at origin, which associates with the BS that provides the highest downlink power. We assume that all the BSs have equal antenna gain, such that the nearest BS provides the highest downlink power. Accordingly, the distribution of the distance d of the typical user from the base of the the serving BS is given

by [52]:

$$f_d(x) = 2\lambda \exp(-2\lambda x). \quad (5.1)$$

The typical user is assumed to have AoA ψ and AoD ξ but since we are considering one-dimensional model, we can represent the AoD in terms of d . Hence we represent the AoD as $\xi(d)$. Each BS, with height h_B , and user is equipped with mm-wave uniform linear array (ULA) directional antenna both with M antenna elements with BS antenna array response given as follows:

$$\mathbf{a}_{BS}(d) = \frac{1}{\sqrt{M}} \left[1, e^{j\frac{2\pi\kappa}{\lambda_c} \sin(\xi(d))}, \dots, e^{j(M-1)\frac{2\pi\kappa}{\lambda_c} \sin(\xi(d))} \right], \quad (5.2)$$

where, κ is the inter-element distance in the antennas and λ_c is the wavelength corresponding the center frequency f_c of the system. For the receive antenna response $\mathbf{a}_{UE}(\psi)$ at UE, simply replace $\xi(d)$ with ψ in equation (5.2). Similarly, let $\mathbf{f}, \mathbf{w} \in \mathbb{C}^M$ represent the transmit and receive beamforming vectors respectively.

For tractability, we simplify the above antenna model to a sectorized model [110]. The directivity gain of the transmit (G_{TX}) and receive (G_{RX}) antennas is discretized into the main-lobe directivity gain $G_{\frac{2\pi}{\theta}}$ and the side-lobe directivity gain $g_{\frac{2\pi}{2\pi-\theta}}$ where θ is the beamwidth of the main-lobe. We assume the total base station coverage area of d_a and a beam dictionary of size N where the N beams provide total coverage at all the points in the area. Accordingly, every unique N has a unique θ in order to provide this coverage. The transmit power of the BSs is assumed to be a constant P_t .

5.2.2 Path-loss

We consider a Nakagami fading with parameter n_0 and variance 1 to model the low local scattering for communications [102]. At the receiver located at the origin, the power received from a BS located at a distance d including the pathloss is given by:

$$P_r = \frac{|h|^2 K P_t G_{TX} G_{RX}}{(d^2 + h_B^2)^{\alpha_L/2}}, \quad (5.3)$$

where K is the path loss coefficient, h represents the fast-fading, and α is the path loss exponent.

5.2.3 Received signal model

Let $s(t)$ be the transmitted signal transmitted by the BS. The signal received at the user can be written as:

$$y(t) = \sqrt{P_r}s(t - \tau) + n(t), \quad (5.4)$$

where, $\tau = d/c$ with d being the true distance from BS to the user and c the speed of light and $n(t)$ is the zero mean Gaussian noise with variance σ_{nm}^2 .

We assume the transmit signal $s(t)$ with duration T_s has flat spectrum with $|S(\omega)|^2 = T_s/(2\pi B)$ where B is the bandwidth of the system [24].

5.2.4 Transmission Policy

In our work, we assume a joint localization and communication framework facilitated by time split across the two phases. Of the constant total transmit time T_t , we allocate a fraction β of the time for communication and the rest $(1 - \beta)$ to localization. Hence, time allocated for communications is $T_c = \beta T_t$ and that for localization is $T_L = (1 - \beta)T_t$.

5.3 Localization Phase

In this section, we characterize the CRLB in terms of delay (estimated with respect to the phase difference) and AoA. Consider the estimation variables to be τ , ψ , h_R and h_I where h_R and h_I represent the real and imaginary part of the channel. Similar to [24], since we have considered the symmetric power spectral density of the transmitted signal, the Fisher Information Matrix (FIM) for delay estimation decouples with the rest of the estimation parameters. FIM \mathbf{J} from [61] and [24] for the estimation of the mentioned variables are given below.

$$\mathbf{J} = \begin{bmatrix} J_{\tau,\tau} & 0 & 0 & 0 \\ 0 & J_{\psi,\psi} & J_{h_R,\psi} & J_{h_I,\psi} \\ 0 & J_{\psi,h_R} & J_{h_R,h_R} & 0 \\ 0 & J_{\psi,h_I} & 0 & J_{h_I,h_I} \end{bmatrix}, \quad (5.5)$$

where σ_N^2 is the variance of the estimation error and considering $\alpha_L = 2$

$$J_{\tau,\tau} = \frac{K P_t G_{RX} G_{TX} (1 - \beta) T_t}{(h_B^2 + d^2) \sigma_N^2} |h|^2 \alpha_r \alpha_t \frac{B^2 \pi^2}{3}, \quad (5.6a)$$

$$J_{\psi,\psi} = \frac{K P_t G_{RX} G_{TX} (1 - \beta) T_t \cos^2(\psi)}{(h_B^2 + d^2) \sigma_N^2} |h|^2 \alpha_{r,1} \alpha_t, \quad (5.6b)$$

$$J_{h_R,\psi} = \frac{K P_t G_{RX} G_{TX} (1 - \beta) T_t \cos(\psi)}{(h_B^2 + d^2) \sigma_N^2} \alpha_{r,2} \alpha_t, \quad (5.6c)$$

$$J_{h_I,\psi} = \frac{K P_t G_{RX} G_{TX} (1 - \beta) T_t \cos(\psi)}{(h_B^2 + d^2) \sigma_N^2} \alpha_{r,3} \alpha_t, \quad (5.6d)$$

$$J_{h_R,h_R} = \frac{K P_t G_{RX} G_{TX} (1 - \beta) T_t}{(h_B^2 + d^2) \sigma_N^2} \alpha_r \alpha_t, \quad (5.6e)$$

$$J_{h_I,h_I} = \frac{K P_t G_{RX} G_{TX} (1 - \beta) T_t}{(h_B^2 + d^2) \sigma_N^2} \alpha_r \alpha_t, \quad (5.6f)$$

and,

$$\alpha_t = |\mathbf{a}_{BS}^H(\xi(d)) \mathbf{f}|^2, \quad (5.7a)$$

$$\alpha_r = |\mathbf{a}_{UE}^H(\psi) \mathbf{w}|^2, \quad (5.7b)$$

$$\alpha_{r,1} = \left| -j \frac{2\pi\kappa}{\lambda_c} \mathbf{D}^H \mathbf{a}_{UE}^H(\psi) \mathbf{w} \right|^2, \quad (5.7c)$$

$$\alpha_{r,2} = \Re \left\{ j \frac{2\pi\kappa}{\lambda_c} h \mathbf{a}_{UE}^H(\psi) \mathbf{w} \mathbf{w}^H \mathbf{D} \mathbf{a}_{UE}(\psi) \right\}, \quad (5.7d)$$

$$\alpha_{r,3} = \Im \left\{ j \frac{2\pi\kappa}{\lambda_c} h \mathbf{a}_{UE}^H(\psi) \mathbf{w} \mathbf{w}^H \mathbf{D} \mathbf{a}_{UE}(\psi) \right\}, \quad (5.7e)$$

where $\mathbf{D} = \text{diag}\{0, 1, \dots, M-1\}$.

The CRLB for delay (by inverting the first element in the matrix) and AoA estimation (from Schur's decomposition similar to [97]) can be written as follows.

$$\sigma_\tau^2 = \left(\frac{K P_t G_{RX} G_{TX} T_t |h|^2 (1 - \beta)}{(h_B^2 + d^2) \sigma_N^2} \alpha_r \alpha_t \frac{B^2 \pi^2}{3} \right)^{-1}, \quad (5.8)$$

$$\sigma_\psi^2 = \left(\frac{K P_t G_{RX} G_{TX} T_t |h|^2 (1 - \beta) \cos^2(\psi)}{(h_B^2 + d^2) \sigma_N^2} \alpha_t \left(\alpha_{r,1} - \frac{\alpha_{r,4}}{\alpha_r} \right) \right)^{-1}, \quad (5.9)$$

where $\alpha_{r,4} = \left| j \frac{2\pi\kappa}{\lambda_c} \cos(\psi) \mathbf{a}_{UE}^H(\psi) \mathbf{w} \mathbf{w}^H \mathbf{D} \mathbf{a}_{UE}(\psi) \right|^2$. For the distance $d = \tau c$, $\sigma_d^2 = c^2 \sigma_\tau^2$.

5.4 Beam-Selection Error

In this section, we characterize the beam-selection error as a consequence of the estimation error in positioning.

The number of beams in the dictionary of a BS with coverage area d_a is N . Accordingly, the coverage area of the i -th beam for the beam dictionary size of

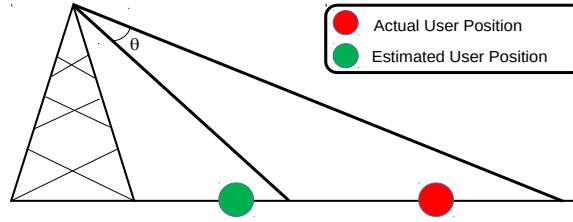


FIGURE 5.1: Beam selection error.

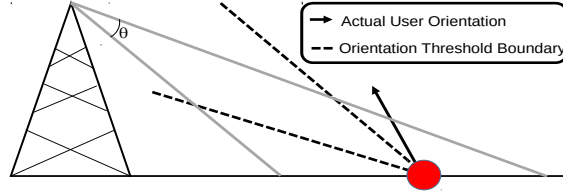


FIGURE 5.2: Beam-misalignment.

N is given by $\mathcal{C}_i = d_{R_i} - d_{L_i}$, where:

$$d_{R_i} = h_B \tan \left(\arctan \left(\frac{d_{L_1}}{h_B} \right) + i\theta \right), \quad i = 1, 2, \dots, N, \quad (5.10)$$

and $d_{L_i} = d_{R_{i-1}}, \forall i = 2, \dots, N^1$, where the number of beams, N is defined as

$$N = \left\lceil \frac{1}{\theta} \arctan \left(\frac{d_a - d_{L_1}}{h_B} \right) \right\rceil. \quad (5.11)$$

Without loss of generality, assume that the typical user is estimated to be located at x , and accordingly, it has been assigned the i -th beam. Due to positioning errors, the actual position of the typical user is given by:

$$\hat{x} = \mathcal{N}(x, \sigma_d^2) \quad (5.12)$$

Beam-selection error occurs for the typical user in case it lies outside \mathcal{C}_i . Averaging out on the possible beams that can be selected, and the relative positions of the typical UE to BS, we have the following result.

Theorem 2. *The average beam-selection error in case of a beam-dictionary of size N is given by:*

$$\bar{\mathcal{P}}_{BS} = \int_0^\infty \left(\sum_{i=1}^{N(y)} \int_{d_{L_i}}^{d_{R_i}} \left(1 - \mathcal{Q} \left(\frac{d_{L_i} - x}{\sigma_d^2(x)} \right) \right) \right) \quad (5.13)$$

¹ d_{L_i} is conventionally assigned to be 0 m.

$$+ \mathcal{Q}\left(\frac{d_{R_i} - x}{\sigma_d^2(x)}\right) f_d(x) dx \Big) f_{d_a}(y) dy.$$

Here, $\mathcal{Q}(\cdot)$ is the Q -function.

Proof. See Appendix C.1. □

An important step in the proof of Theorem 2 is the characterization of the beam-selection error in case the i -th beam is selected. We will use this result in the modeling the effect of beam-selection error on the downlink data rate, and hence we state it formally below:

Corollary 6. *The probability of beam-selection error in case the typical user is estimated to be located at x , is computed as:*

$$\begin{aligned} \mathcal{P}_{BS_i}(x) &= \mathbb{P}(\hat{x} < d_{L_i}) + \mathbb{P}(\hat{x} > d_{R_i}) \\ &= 1 - \mathcal{Q}\left(\frac{d_{L_i} - x}{\sigma_d^2(x)}\right) + \mathcal{Q}\left(\frac{d_{R_i} - x}{\sigma_d^2(x)}\right) \end{aligned} \quad (5.14)$$

Corollary 7. *In case of deterministic deployments, where the BSs are equispaced, (5.14) becomes:*

$$\bar{\mathcal{P}}_{BS} = \sum_{i=1}^N \int_{d_{L_i}}^{d_{R_i}} \left(1 - \mathcal{Q}\left(\frac{d_{L_i} - x}{\sigma_d^2(x)}\right) + \mathcal{Q}\left(\frac{d_{R_i} - x}{\sigma_d^2(x)}\right)\right) f_d(x) dx \quad (5.15)$$

where,

$$N = \left\lceil \frac{1}{\theta} \arctan\left(\frac{\frac{1}{\lambda} - d_{L_1}}{h_B}\right) \right\rceil$$

5.5 Data Service Phase

In this section, first we characterize the SINR coverage probability of the typical UE considering the beam-selection error into account. Based on that, we define the effective downlink data rate of the typical UE.

5.5.1 Characterization of the Rate Coverage Probability

The SINR coverage probability is defined as the probability that the typical UE receives an SINR over a given threshold. From the network perspective, it

represents the fraction of total users that are under coverage. Mathematically, it is characterized in the following theorem.

Theorem 3. *The SINR coverage probability of the typical user is given by:*

$$\begin{aligned} \mathcal{P}_{C,i}(T, N) = \int_{d_{L_i}}^{d_{R_i}} 2\lambda [\mathcal{P}_{BS_i}(x)\mathcal{T}_{BS}(x, T) \\ + (1 - \mathcal{P}_{BS_i}(x))\mathcal{T}_0(x, T)] \exp(-2\lambda x) dx, \end{aligned} \quad (5.16)$$

where,

$$\mathcal{T}_0(x, T) = \exp\left(-\frac{T\sigma_{mm}^2}{P_i K g x^{-\alpha_L}} - \mathcal{A}_{L0}(x, T) - \mathcal{A}_{N0}(x, T)\right), \quad (5.17a)$$

$$\mathcal{T}_{BS}(x, T) = \exp\left(-\frac{T\sigma_{mm}^2}{P_i K G x^{-\alpha_L}} - \mathcal{A}_{LBS}(x, T) - \mathcal{A}_{NBS}(x, T)\right), \quad (5.17b)$$

in which

$$\mathcal{A}_{L0}(x, T) = \int_x^{d_S} \frac{T g^2 y^{-\alpha_L}}{G^2 x^{-\alpha_L} + T g^2 y^{-\alpha_L}} 2\lambda y dy \quad (5.18a)$$

$$\mathcal{A}_{N0}(x, T) = \int_{d_S}^{\infty} \frac{T g^2 y^{-\alpha_N}}{G^2 x^{-\alpha_L} + T g^2 y^{-\alpha_N}} 2\lambda (y - d_S) dy \quad (5.18b)$$

$$\mathcal{A}_{LBS}(x, T) = \int_x^{d_S} \frac{T y^{-\alpha_L}}{x^{-\alpha_L} + T y^{-\alpha_L}} 2\lambda y dy \quad (5.18c)$$

$$\mathcal{A}_{NBS}(x, T) = \int_{d_S}^{\infty} \frac{T y^{-\alpha_N}}{x^{-\alpha_L} + T y^{-\alpha_N}} 2\lambda (y - d_S) dy \quad (5.18d)$$

Proof. See Appendix C.2. □

Here the subscripts $L0$ and $N0$ refer to the case without beam-selection error and the subscripts LBS and NBS refer to the cases with beam selection error.

Corollary 8. *The overall SINR coverage probability is then calculated as*

$$\mathcal{P}_C(T, N) = \sum_{i=1}^N \mathcal{P}_{C,i}(T, N) \quad (5.19)$$

5.5.2 Effective Rate Coverage Probability

Considering that the data service phase consists of β fraction of the total time of the positioning-communication scheme, we can obtain the effective rate coverage probability as below:

Corollary 9. *For a given SINR coverage probability, the effective rate coverage probability is given by:*

$$\mathcal{P}_R(r_0, \beta, N) = \mathbb{P}(\beta B \log_2(1 + \text{SINR}) \geq r_0) \quad (5.20a)$$

$$= \mathbb{P}\left(\text{SINR} \geq 2^{\frac{r_0}{\beta B}} - 1\right) \quad (5.20b)$$

$$= \mathcal{P}_C\left(2^{\frac{r_0}{\beta B}} - 1, N\right) \quad (5.20c)$$

5.6 Optimal Selection of Beam-Dictionary

Finally, given our characterization of the effective rate coverage probability based on the efficiency of estimation of the position and orientation of the UE in terms of the corresponding estimation errors, we present a schematic for selection of optimal beam-dictionary. The schematic is presented in the form of a two-stage optimization problem as shown below:

$$N^* = \underset{N}{\operatorname{argmax}} \left[\begin{array}{l} \max_{\beta} \mathcal{P}_R(r_0, \beta, \theta) \\ \text{subject to } \sqrt{\mathbb{E}_{\psi, d} [\sigma_{\psi}^2(\beta, N, d)]} \leq \epsilon \end{array} \right] \quad (5.21)$$

In the first step, for a given N , we select the value of β that maximizes the effective rate coverage probability subject to a constraint (ϵ) on the error in estimation of the orientation of the UE. In positioning-assisted mm-wave communication schemes, this constraint can be a system parameter which governs the alignment capabilities of the BS-UE pair. In other words, if the orientation of the UE is known up to a confidence of $1 - \epsilon$, the UE can be programmed to realign to the best possible direction.

5.7 Numerical Results and Discussions

In this section, we present the simulation results to evaluate the beamwidth selection strategy for a mm-wave small cell network with $\lambda = 10 \text{ km}^{-1}$ and 50 km^{-1} and $d_s = 100 \text{ m}$ operating at center frequency f_c of 60 GHz with bandwidth B of 1 GHz. Moreover, assume $P_t = 1 \text{ W}$, the transmit and receive main

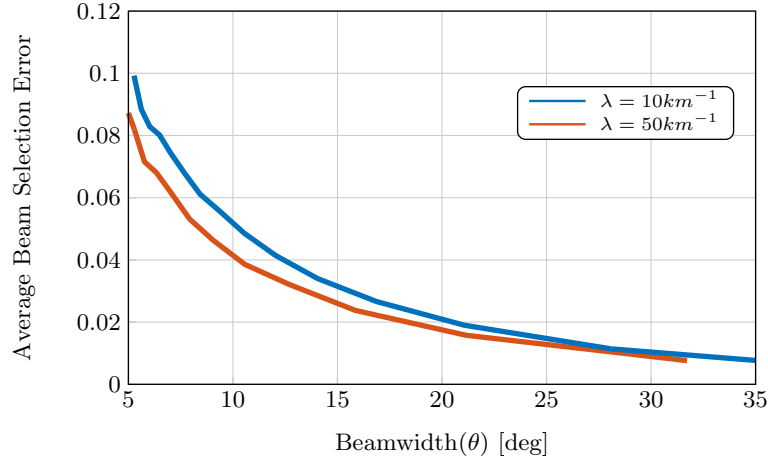


FIGURE 5.3: Average Beam Selection Error $\bar{\mathcal{P}}_{BS}$ varied with the beamwidth for different λ s

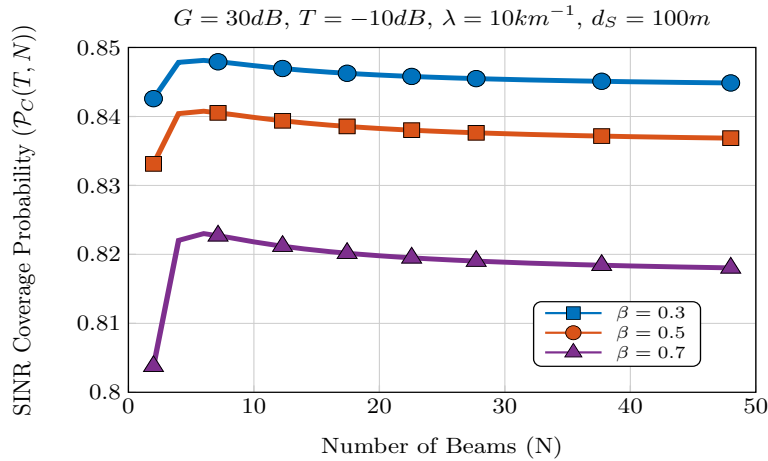


FIGURE 5.4: SINR Coverage Probability $\mathcal{P}_C(T, N)$ varied with N for different β s

and side lobe antenna gains $G = 30$ dB and $g = -10$ dB, $\sigma_{mm}^2 = -174$ dB/Hz. The LOS and NLOS pathloss exponents $\alpha_L = 2$ and $\alpha_N = 4$ respectively. Similarly, the coefficient $K = 7.5 \times 10^{-7}$.

In Fig. 5.3 we present average beam selection error for different number of beams. Wider beamwidth provides more coverage area for localizing the user, hence reduces the error due to the user being within the main lobe of the transmitted beam. Likewise, the figure also shows the effect of increasing the intensity of the PPP. With lower number of BSs due to larger λ , the typical user has more probability of being far from the BS causing σ_d^2 and hence the uncertainty in estimation to increase. Hence for smaller beamwidths, this inaccuracy in the knowledge of user position leads to higher average beam selection error. However, for larger beamwidths, the larger coverage area compensates for this inaccuracy and hence both the plots with $\lambda = 10$ and $50km^{-1}$ converge

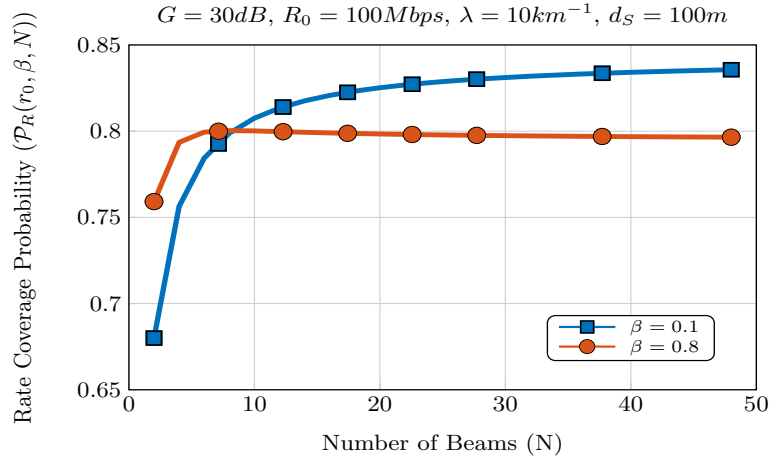


FIGURE 5.5: Rate Coverage Probability $\mathcal{P}_R(r_0, \beta, N)$ varied with N for different β s

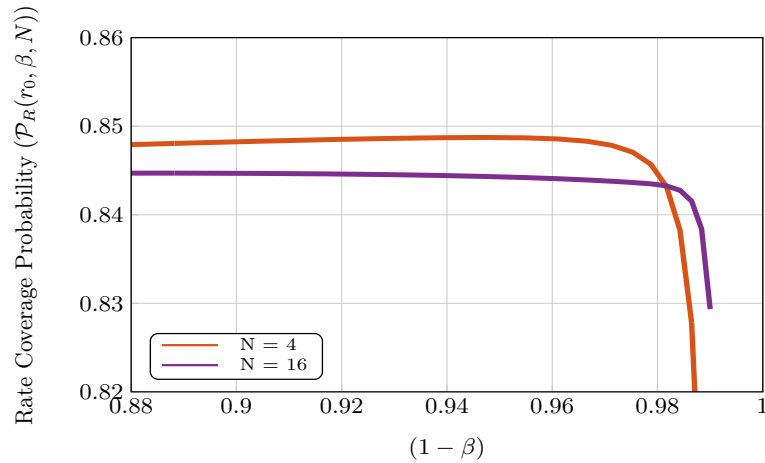


FIGURE 5.6: Rate Coverage Probability $\mathcal{P}_R(r_0, \beta, N)$ varied with $(1 - \beta)$ for different λ s and N

towards each other.

Furthermore, in Fig. 5.4, we plot the SINR coverage probability as a function of the number of beams for different β . It can be noticed that increasing the time allocation for localization for a better localization performance increases the SINR coverage probability as it decreases the probability of having beam selection error. For a certain β , when the number of beam increases and hence the beamwidths get thinner, there is a higher chance of misalignment, in which case, the unwanted power received from interfering BSs decreases the SINR coverage probability.

Likewise, in Fig. 5.5 we can see the rate coverage probability varying with different N s for $\beta = 0.1$ and 0.8 . For lower β , the highly precise localization improves the rate coverage probability even with beams with thinner beamwidths. For larger β , the rate coverage probability increases and then decreases with

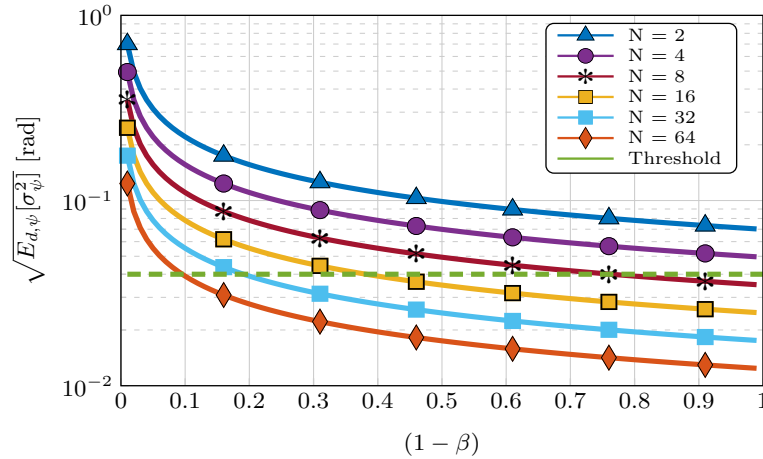


FIGURE 5.7: Average AoA estimation error varied with $(1 - \beta)$ for different N

thinner beamwidth due to worse positioning performance.

Similarly, in Fig. 5.6, we can clearly see the effect of favoring localization over communication. The rate coverage probability increases while increasing T_L except after 96% when the T_C is so low that the rate coverage degrades very rapidly due to outage. Comparing the different number of beams, using 16 beams instead of 4 is beneficial with respect to the rate coverage only after the user has been very accurately localized.

In Fig. 5.7, we can see average AoA estimation error plotted against the fraction of time allocated for localization where we consider the AoA at the user to be distributed uniformly between -30 to 30 degrees. As expected, the error reduces as we decrease the β . However, when we set the maximum error threshold for estimation error, using some N s and β s, we can never achieve the required threshold. In our canonical case, we must use at least 8 beams and that with $\beta \leq 0.2$ to achieve the threshold of 0.04 rad.

From the above figures, we can summarize that for a given λ , increasing N increases the beam selection error and even though it increases the SINR coverage probability initially, too thin beams decreases this probability due to beam selection error and resulting interference from other BSs. Similarly, allocating large portion of time for accurate localization of user is important in achieving high rate and SINR coverage probability. Hence, from these analyses it is essential to optimally allocate the parameters θ and β for improvement of both localization and hence throughput performance at the user.

In selecting the optimal N (or equivalently the optimal beamwidth), from equation (5.21), we first need to create a feasible set of β and N complying

with the AoA error constraint. In our canonical example, for instance, the set of all N and for each N , the corresponding β s which are below the threshold in Fig. 5.7 lie in the feasible set. From these set of N s and β s, we then choose the parameters that maximize the rate coverage probability in as the optimal N and the corresponding β . For instance, in Fig. 5.5, even though the curve with $N = 4$ performs better in terms of rate coverage when $(1 - \beta) \leq 0.98$ since for $N = 4$ the estimation error in AoA cannot fulfill the threshold requirement. Similarly, in Fig. 5.5, for the curve when $\beta = 0.8$, we can only consider the rate coverage probability for $N > 32$ to satisfy the constraint.

5.8 Chapter Conclusions

In this chapter, we have characterized and presented the throughput optimal beamwidth selection criteria depending on the localization and communication trade-off for a mm-wave system. We characterized the variance of estimation through CRLB for localization with parameters delay and AoA. Then after characterization of the uncertainty in position estimation, we formulate the average beam selection error and subsequently the SINR and rate coverage probabilities. Finally, with the help of these formulations, we propose a policy for optimal beamwidth selection for maximizing the rate coverage probability which depends on the time allocation scheme for localization and data rate services also considering the error in estimating the AoA.

Chapter 6

Conclusions and Future Perspectives

6.1 Main Conclusions

In this thesis we modeled and investigated multi-tier multi-RAT networks consisting of mm-wave small cells. First, we studied a homogeneous deployment model of mm-wave multi-RAT SBS overlaid on top of the legacy macro architecture in Chapter 2. We showed that mm-wave communication is not only capable of providing high downlink data-rates, but also that sufficiently dense deployment of mm-wave base stations may result in a significant improvement of the SINR of the users. This is precisely due to the fact that mm-wave signals suffer from lower interference as compared to the sub-6GHz signals.

Then, by using elements of queuing theory, we characterized the load of different tiers in the multi-RAT HetNets by considering dynamic traffic, which paved the way for a more accurate modeling of user throughput. Our study highlights the fundamental trade-offs between outage probability, user throughput, and cell overloading, and, thereby, highlights the necessity of the dual band small cells to maintain outage below a certain threshold, specially in sparse deployments. In our system model, we proposed effective approaches to optimize the user association for enhancing coverage or maximizing throughput.

In the context of dynamic cell load, in Chapter 3, we derived a simple approximation for the CDF of the cell load of the typical cell in a noise-limited network, which is characterized by high SINR and low inter-cell interference. Furthermore, we obtained a single approximation-based expression and a closed-form expression for the average load of the network by using the distribution of the area of the typical cell. Our derivations present a more realistic characterization of the cell load, as compared to the recently introduced mean cell

approach, since we consider the typical cell of the network rather than the zero cell [57]. The analysis provides a tractable and accurate characterization for the cell load, which can be utilized, e.g., for evaluating the user throughput and dimensioning 5G networks. However, accurate characterization of the dynamic network load in case of an interference prone network is not straightforward. This will be addressed in a future work.

Then, in Chapter 4, we considered a more realistic deployment geometry of the mm-wave multi-RAT SBSs in urban environments, by modeling their positions along the roads of a city. We provided realistic characterizations of the mm-wave interference and the effect of vehicular blockage on the mm-wave RAT. First, from the perspective of the pedestrian users, we analyzed the effect of the RAT selection bias on the mm-wave blockage, SINR coverage, and rate coverage probability under different vehicular densities. Accordingly, we have provided a slice-aware RAT selection strategy to jointly support URLLC, mMTC, and eMBB applications in future mm-wave sliced 5G networks. We highlighted several key system design insights for an operator that aims to optimally serve a diverse variety of services. Specifically, in case the operator needs to prioritize mm-wave association for high-data rate services so as to free the sub-6GHz RAT for reliability specific applications, it needs to deploy more SBSs per road in a city with more roads. However, excessive deployment of SBSs degrades the SINR performance of the users. Thus, proper care must be taken of this tradeoff while dimensioning the cellular network. Moreover, having a network-wide RAT selection bias will not be able to support a diverse plethora of applications. Hence, slice-aware RAT selection becomes necessary. For URLLC services, there exists a threshold of bias beyond which the blockage of the service becomes intolerable. For applications that require high SINR coverage on the contrary, e.g., mMTC, there exist non-trivial biases that maximize the SINR. Moreover, the bias values that maximize the downlink data rate may lead to excessive outage, and hence, we provided optimal bias values for rate coverage under outage constraints. If the operator wants to increase the rate coverage even further, e.g., for eMBB applications, it is important to develop efficient interference management mechanisms as increasing the deployment density simply degrades the SINR performance.

In this urban deployment scenario, we characterized a mm-wave system deployed to support positioning and broadband services simultaneously in Chapter 5. Specifically, we introduced a power-partitioning based mechanism that

enables the mm-wave BS to satisfy different localization and data-rate requirements. We characterized the statistical localization performance by deriving the BCRLB of positioning based on the power allotted to the positioning functionality. Then, based on the power allotted to the data-communication functionality, we derived dimensioning rules in terms of the density of BSs required to limit outage probability. Furthermore, we provided the operator with a beamwidth selection guideline for positioning, to limit the misalignment probability between the user and BS beams. Then, we studied the trade-off between the localization efficiency and the downlink data rate, and consequently, presented a scheme for partitioning the transmit power depending on the service requirements.

Finally, we characterized and studied the throughput optimal beamwidth selection criteria in terms of the localization and communication trade-off in Chapter 6. We derived the variance of the estimation error in positioning based on the CRLB for localization and AoA. Then, we formulated the average beam selection error and subsequently the SINR and rate coverage probabilities of the typical user in this system. Based on these formulations, we proposed a policy for optimal beamwidth selection and resource-partitioning scheme for maximizing the rate coverage probability of the users in the network.

Thus, in this thesis, we have provided several guidelines and dimensioning rules to the operator for the urban deployment of first-generation mm-wave SBSs that will form an integral part of the 5G eco-system. We also defined and derived several new performance metrics (e.g., effective throughput, beam-selection error and vehicular blockage probability). This thesis paves the way for several future directions of research, some of which are discussed in the next section.

6.2 Future Work

6.2.1 Realistic Characterization of Performance metrics

In our work we have provided approximate expressions for the typical cell load in a noise-limited network. However, using stochastic geometry, the accurate characterization of the typical cell load in general is still an open challenge. Integration of multiple RATs in the network, specially mm-wave small cells complicates this challenge even further since the cell-boundaries become not well-defined owing to the random LOS-NLOS transitions of signal states.

Furthermore, accurate characterization of mm-wave signal blockages both in outdoor and indoor contexts is also an open direction of research.

6.2.2 Reliable mm-wave Communications

The initial deployment of mm-wave BSs will definitely require the existing cellular networks for reliable functioning. However, it is envisioned that as the network needs, volume of users and use-cases grow, there will be a call for reliable mm-wave communications. In particular, seamless connectivity support for unconstrained device mobility is needed for mission-critical applications. The future internet-of-things devices will also need to offload their more demanding computations to the proximate edge-computing infrastructure, for which high data-rate, low latency, and extremely reliable links are required.

In this regard, an important future research direction of research is that of enhancing mm-wave reliability, which would encompass multi-connectivity, band-agility, and network densification. In particular, one interesting problem involves developing sequential decision algorithms to switch BS connections based on identifying the blockage statistics of several mm-wave links. In this context, integrating efficient artificial intelligence algorithms to facilitate beam-switching is also a possible direction of interest.

6.2.3 Multi Agent and Cooperative localization in 5G

In the future 5G network, localization will play an ever-increasing role, not only for location-based services like autonomous vehicles, but also for location-aware intelligent communication solutions such as proactive radio resource management. It is widely believed that 5G architecture with ultra-densification, large antenna arrays, and wide bandwidths will provide excellent resources for efficient positioning and ranging. A research direction in this regard could be to develop and study different algorithms for highly accurate and energy-efficient positioning, that will be implemented in use-cases providing localization-as-a-service.

6.2.4 Network Slicing and Orchestration

It has gradually become evident that in addition to the radio technology, several disruptive changes in 5G will be in the core architecture. In fact, it is the extreme architecture disruption that has made supporting a plethora of

use-cases plausible. Future wireless networks will contain more service-based architectures with a bigger role of the edge cloud and network slicing algorithms. Generally speaking, network slicing will not only give QoS guarantee on the radio, but will do so on an end-to-end perspective. The vitality of network slicing and orchestration will become more evident with the increasing number of services.

It is interesting to note that efficient allocation resources across network slices has not been well studied in the literature, which we intend to investigate in a systematic manner. One particular research problem in this direction is in the purview of resource elasticity, to make efficient use of the computational resources. Orchestration-driven flexible placement of network functions, and cross-slice resource provisioning mechanisms.

Appendix A

Proofs of Chapter 2

A.1 Tier Selection Probability

The probabilities that at least one LOS MBS and LOS SBS exist are, respectively, $\mathbb{E}[1(t_M L)] = 1 - \exp(-\pi\lambda_M d_M^2)$ and $\mathbb{E}[1(t_S L)] = 1 - \exp(-\pi\lambda_S d_S^2)$. Then, the values of $\mathbb{P}(\tilde{Q}_T P_{tv\mu 1} > \tilde{Q}_T P_{t'v\mu 1})$ are derived as follows:

$$\begin{aligned}
& \mathbb{P}(P_{ML\mu 1} > Q_T \cdot P_{SL\mu 1}) \\
&= \int_0^\infty e^{-\Lambda'_{SL\mu}(0, Q_T r)} e^{-\Lambda'_{ML\mu}(0, r)} \lambda'_{ML\mu}(r) dr \\
&= \int_0^{\frac{d_S^{\alpha_{SL\mu}}}{Q_T \cdot K_{SL\mu} P_S}} e^{-\Lambda'_{SL\mu}(0, Q_T r)} e^{-\Lambda'_{ML\mu}(0, r)} \lambda'_{ML\mu}(r) dr + \\
&\quad \int_{\frac{d_S^{\alpha_{SL\mu}}}{Q_T \cdot K_{ML\mu} P_S}}^{\frac{d_M^{\alpha_{ML\mu}}}{K_{SL\mu} P_M}} e^{-\Lambda'_{SL\mu}\left(0, \frac{d_S^{\alpha_{SL\mu}}}{K_{SL\mu} P_S}\right)} e^{-\Lambda'_{ML\mu}(0, r)} \lambda'_{ML\mu}(r) dr \\
&= \frac{1}{1 + K_1} (1 - e^{-(K_1+1)t_1}) + e^{-\Lambda'_{SL\mu}\left(0, \frac{d_S^{\alpha_{SL\mu}}}{K_{SL\mu} P_S}\right)} \cdot \left[\exp\left(-\Lambda'_{ML\mu}\left(0, \frac{d_S^{\alpha_{SL\mu}}}{Q_T K_{SL\mu} P_S}\right)\right) - \right. \\
&\quad \left. \exp\left(-\Lambda'_{ML\mu}\left(0, \frac{d_M^{\alpha_{ML\mu}}}{K_{ML\mu} P_M}\right)\right) \right],
\end{aligned}$$

where, $K_1 = \pi\lambda_S \left(\frac{K_{SL\mu} P_S Q_T}{P_M}\right)^{\frac{2}{\alpha_{SL\mu}}} (\pi\lambda_M)^{-\frac{\alpha_{ML\mu}}{\alpha_{SL\mu}}}$ and

$$t_1 = \pi\lambda_M (K_{ML\mu} P_M)^{\frac{2}{\alpha_{ML\mu}}} \left(\frac{d_S^{\alpha_{SL\mu}}}{Q_T K_{SL\mu} P_S}\right)^{\frac{2}{\alpha_{ML\mu}}}. \text{ Similarly,}$$

$$\mathbb{P}(P_{MN\mu 1} > Q_T \cdot P_{SN\mu 1}) = \exp\left(-\Lambda'_{SN\mu}\left(0, \frac{d_S^{\alpha_{SN\mu}}}{K_{SN\mu} P_S}\right)\right) \frac{e^{-(K_2+1)t_2}}{1 + K_2},$$

where $K_2 = \pi \lambda_S \left(\frac{K_{SN\mu} P_S Q_T}{K_{MN\mu} P_M} \right)^{\frac{2}{\alpha_{SN\mu}}} (\pi \lambda_M)^{-\frac{\alpha_{MN\mu}}{\alpha_{SN\mu}}}$ and $t_2 = \pi \lambda_M d_M^2 (K_{MN\mu} P_M)^{\frac{2}{\alpha_{MN\mu}} - 1}$. Finally,

$$\begin{aligned} \mathbb{P}(Q_T \cdot P_{SL\mu 1} > P_{ML\mu 1}) &= 1 - \mathbb{P}(P_{ML\mu 1} > Q_T \cdot P_{SL\mu 1}); \\ \mathbb{P}(Q_T \cdot P_{SN\mu 1} > P_{MN\mu 1}) &= 1 - \mathbb{P}(P_{MN\mu 1} > Q_T \cdot P_{SN\mu 1}). \end{aligned}$$

Using these expressions in Eq. (2.3) and Eq. (2.4) completes the proof.

A.2 RAT Selection Probability

The power received from strongest SBS of state v is $P_{Sv\mu 1} = (\xi_{Sv\mu 1})^{-1} = K_{Sv\mu} P_S \|x_{Sv1}\|^{-\alpha_{Sv\mu}}$.

So, the estimate of the mm-wave power is: $P_{Svm1} = G_0 K_{SLm} P_S \|x_{Sv1}\|^{-\alpha_{Svm}}$. Therefore the probability of sub-6GHz service, given that the user is associated with strongest SBS of visibility state v , is calculated as:

$$\begin{aligned} \mathbb{P}_{v\mu} &= \mathbb{P}(P_{Sv\mu 1} > Q_R \times P_{Svm1}) \\ &= \mathbb{P}\left(\|x_{Sv1}\| \geq \left(\frac{K_{Svm} G_0 Q_R}{K_{Sv\mu}}\right)^{\frac{1}{\alpha_{Svm} - \alpha_{Sv\mu}}}\right) \\ &= \exp\left(-\pi \lambda_S \left(\frac{K_{Svm} G_0 Q_R}{K_{Sv\mu}}\right)^{\frac{2}{\alpha_{Svm} - \alpha_{Sv\mu}}}\right) \end{aligned} \quad (\text{A.1})$$

The probability of mm-wave service is given by $\mathbb{P}_{Svm} = 1 - \mathbb{P}_{Sv\mu}$. This completes the proof.

A.3 Proof of Eq. (2.15)

We provide the derivation only for the LOS MBS association case. The other cases follow similarly. When the user is associated with the strongest LOS MBS, it experiences interference from the other LOS MBSs, the NLOS MBSs, and the SBSs. Thus, the instantaneous SINR is:

$$SINR_{ML\mu} = \frac{h_{\xi_{ML\mu 1}} (\xi_{ML\mu 1})^{-1}}{I_{ML\mu} + I_{MN\mu} + I_{SL\mu} + I_{SN\mu} + \sigma_N^2},$$

where $I_{\{\cdot\}}$ denote the interference terms given as

$$\begin{aligned} I_{ML\mu} &= \sum_{\xi_{ML\mu i} \in \phi'_{ML\mu} \setminus \{\xi_{ML\mu 1}\}} h_{\xi_{ML\mu i}} (\xi_{ML\mu i})^{-1}; \\ I_{MN\mu} &= \sum_{\xi_{MN\mu i} \in \phi'_{MN}} h_{\xi_{MN\mu i}} (\xi_{MN\mu i})^{-1}; \\ I_{SL\mu} &= \sum_{\xi_{SL\mu i} \in \phi'_{SL\mu}} h_{\xi_{SL\mu i}} (\xi_{SL\mu i})^{-1}; \\ I_{SN\mu} &= \sum_{\xi_{SN\mu i} \in \phi'_{SN\mu}} h_{\xi_{SN\mu i}} (\xi_{SN\mu i})^{-1}. \end{aligned}$$

Now,

$$\begin{aligned} \mathbb{P}_{CML\mu} &= \mathbb{P}(SINR_{ML\mu} > \gamma) \\ &= \mathbb{P}\left(\frac{h_{\xi_{ML\mu 1}} (\xi_{ML\mu 1})^{-1}}{I_{ML\mu} + I_{MN\mu} + I_{SL\mu} + I_{SN\mu} + \sigma_N^2} > \gamma\right) \\ &= \mathbb{P}\left(h_{\xi_{ML\mu 1}} > \frac{\gamma(I_{ML\mu} + I_{MN\mu} + I_{SL\mu} + I_{SN\mu} + \sigma_N^2)}{(\xi_{ML\mu 1})^{-1}}\right) \\ &\stackrel{(a)}{=} \mathbb{E}_{\xi_{ML\mu 1}} \left\{ \mathbb{E}_{\phi'_{ML\mu}} \left[\exp\left(-\frac{\gamma \cdot I_{ML\mu}}{(\xi_{ML\mu 1})^{-1}}\right) \right] \cdot \mathbb{E}_{\phi'_{MN\mu}} \left[\exp\left(-\frac{\gamma \cdot I_{MN\mu}}{(\xi_{ML\mu 1})^{-1}}\right) \right] \cdot \right. \\ &\quad \left. \mathbb{E}_{\phi'_{SL\mu}} \left[\exp\left(-\frac{\gamma \cdot I_{SL\mu}}{(\xi_{ML\mu 1})^{-1}}\right) \right] \cdot \mathbb{E}_{\phi'_{SN\mu}} \left[\exp\left(-\frac{\gamma \cdot I_{SN\mu}}{(\xi_{ML\mu 1})^{-1}}\right) \right] \left(\exp\left(-\frac{\gamma \cdot \sigma_N^2}{(\xi_{ML\mu 1})^{-1}}\right) \right) \right\}, \end{aligned}$$

where (a) comes from the pdf of $h_{\xi_{ML\mu 1}}$. Now,

$$\begin{aligned} \mathbb{E}_{\phi'_{ML\mu}} \left[\exp\left(-\frac{\gamma \cdot I_{ML\mu}}{(\xi_{ML\mu 1})^{-1}}\right) \right] &= \mathbb{E} \left[\exp\left(-\frac{\gamma \cdot \sum_{\phi'_{ML\mu} \setminus \{\xi_{ML\mu 1}\}} h_y y^{-1}}{(\xi_{ML\mu i})^{-1}}\right) \right] \\ &= \mathbb{E} \left[\prod_{\phi'_{ML\mu} \setminus \{\xi_{ML\mu 1}\}} \mathbb{E}_{h_y} \left[\exp\left(-\frac{\gamma \cdot h_y (y)^{-1}}{(\xi_{ML\mu 1})^{-1}}\right) \right] \right] \\ &= \exp\left(-\int_{\xi_{ML\mu 1}}^{\infty} \left(1 - \mathbb{E}_{h_y} \left[\exp\left(-\frac{\gamma \cdot h_y y^{-1}}{(\xi_{ML\mu 1})^{-1}}\right) \right] \right) \Lambda'_{ML\mu}(dy)\right) \\ &= \exp\left(-\int_{\xi_{ML\mu 1}}^{\infty} \left(\frac{\gamma \xi_{ML\mu 1}}{y + \gamma \xi_{ML\mu 1}} \Lambda'_{ML\mu}(dy)\right)\right). \end{aligned}$$

Similarly,

$$\mathbb{E}_{\phi'_{tv\mu}} \left[\exp \left(-\frac{\gamma \cdot I_{tv\mu}}{(\xi_{ML\mu 1})^{-1}} \right) \right] \exp \left(-\int_{l_{tv}}^{\infty} \left(1 - \frac{y}{y + \gamma \xi_{ML\mu 1}} \Lambda'_{tv\mu}(dy) \right) \right),$$

for $tv = MN, SL$ and SN , respectively, where the lower indexes are: $l_{SL} = l_{SN} = Q_T \cdot \xi_{ML\mu 1}$ and $l_{MN} = \xi_{ML\mu 1}$. Substituting the above results in Eq. (B.1), and taking the expectation with respect to $\xi_{ML\mu 1}$, completes the proof.

A.4 Proof of Proposition 1

Consider two LOS SBS S_1 and S_2 ¹. Let the power received by the typical user from the SBS S_1 in mm-wave and sub-6GHz band be P_{S1m} and $P_{S1\mu}$, respectively. Let the corresponding values for S_2 be P_{S2m} and $P_{S2\mu}$, respectively. Now

$$\begin{aligned} P_{S1\mu} \geq P_{S2\mu} &\iff K_{\mu} P_S d_1^{\alpha_{Sv\mu}} \geq K_{\mu} P_S d_2^{\alpha_{Sv\mu}} \\ &\iff K_m P_S d_1^{\alpha_{Svm}} \geq K_m P_S d_2^{\alpha_{Svm}} \\ &\iff P_{S1m} \geq P_{S2m} \\ &\iff Q_R P_{S1m} \geq Q_R P_{S2m} \end{aligned} \quad (\text{A.2})$$

A.5 Probability of Sub-Optimal Association

Recall that E_1 and E_2 denote the events the biased received power from the strongest SBS (denoted S_1) in sub-6GHz band is less than that received from the strongest MBS (denoted by M_1) and the biased received power from S_1 in mm-wave is higher than the received power from M_1 , respectively. We have:

$$\begin{aligned} \mathbb{P} [E_2 \mid E_1] &= \frac{\mathbb{P} [E_2 \cap E_1]}{\mathbb{P} [E_1]} \\ &= \frac{1}{\mathbb{P} \left[P_M d_{M1}^{-\alpha_{Mv'\mu}} \geq Q_T P_S d_{S1}^{-\alpha_{Sv\mu}} \right]} \cdot \left(\mathbb{P} \left[K_m P_S Q_R Q_T G_0 d_{S1}^{-\alpha_{Svm}} \geq K_{\mu} P_M d_{M1}^{-\alpha_{Mv'\mu}} \cap \right. \right. \\ &\quad \left. \left. P_M d_{M1}^{-\alpha_{Mv'\mu}} \geq Q_T P_S d_{S1}^{-\alpha_{Sv\mu}} \right] \right) \end{aligned}$$

¹The analysis where there are NLOS SBS can be performed with similar reasoning.

$$\begin{aligned}
&= \frac{1}{\mathbb{P} \left[d_{S1} \geq \left(\frac{P_S Q_T}{P_M} d_{M1}^{\alpha_{Mv'\mu}} \right)^{\frac{1}{\alpha_{Sv\mu}}} \right]} \cdot \mathbb{P} \left[d_{S1} < \left(\frac{K_m P_S Q_R Q_T G_0}{K_\mu P_M} d_{M1}^{\alpha_{Mv'\mu}} \right)^{\frac{1}{\alpha_{Svm}}} \cap \right. \\
&\quad \left. d_{S1} \geq \left(\frac{P_S Q_T}{P_M} d_{M1}^{\alpha_{Mv'\mu}} \right)^{\frac{1}{\alpha_{Sv\mu}}} \right] \\
&= \mathbb{E}_{d_{M1}} \left[\frac{1}{\exp \left(-\pi \lambda_S \left(\zeta_1 x^{\alpha_{Mv'\mu}} \right)^{\frac{2}{\alpha_{Sv\mu}}} \right)} \left(\exp \left(-\pi \lambda_S \left(\left(\zeta_2 x^{\alpha_{Mv'\mu}} \right)^{\frac{2}{\alpha_{Svm}}} - \left(\zeta_1 x^{\alpha_{Mv'\mu}} \right)^{\frac{2}{\alpha_{Sv\mu}}} \right) \right) \right) \right] \\
&= 2\pi \lambda_M \cdot \int_0^{d_M} \frac{\exp \left(-\pi \lambda_S \left(\left(\zeta_2 x^{\alpha_{Mv'\mu}} \right)^{\frac{2}{\alpha_{Svm}}} - \left(\zeta_1 x^{\alpha_{Mv'\mu}} \right)^{\frac{2}{\alpha_{Sv\mu}}} \right) \right)}{\exp \left(-\pi \lambda_S \left(\zeta_1 x^{\alpha_{Mv'\mu}} \right)^{\frac{2}{\alpha_{Sv\mu}}} \right)} x \exp(-\pi \lambda_M x^2) dx
\end{aligned}$$

Solving this integral with the approximated values of the path-loss exponents completes the proof.

Appendix B

Proofs of Chapter 4

B.1 Proof of Lemma 13

For the first part of the Lemma, let $\nu(x)$ be a positive measurable, radially symmetric function with bounded support. Let first assume the support to be a disk centered at origin with radius R . Now the function ν in our case is the SINR coverage probability (thus, $0 \leq \nu \leq 1$), and accordingly, the PGF is bounded below by 0 and decreases monotonically with R . The Lemma thus follows from the monotone convergence theorem with $R \rightarrow \infty$. We have:

$$G_{\phi_S}(\nu) = \mathbb{E} \left[\prod_{x \in \phi_S} \nu(x) \right] = \int \prod_{x \in \phi_S} \nu(x) \phi_S(dx),$$

$$\stackrel{a}{=} \sum_{n=0}^{\infty} \frac{\exp(-2\pi R \lambda_R)}{n! R^n} (2\pi R \lambda_R)^n \int_{r_1, r_2, \dots, r_n=0}^R \left(\prod_{i=1}^n \int_{\mathbb{R}} \prod_{x \in \phi_i} \nu(x) \phi_i(dx) \right) dr_1, \dots, dr_n.$$

where (a) is obtained by conditioning on the number of roads (n) and on the distances of the roads (r_1, \dots, r_n)¹. The number of lines crossing a circle with radius R is Poisson distributed with parameter $2\pi R \lambda_R$. Now, for each of the lines, we calculate the PGF as [52]:

$$\int \prod_{x \in \phi_i} \nu(x) \phi_i(dx) = \exp \left(-2\lambda_S \int_0^{\sqrt{R^2 - r^2}} 1 - \nu \left(\sqrt{r_i^2 + t^2} \right) dt \right).$$

As a result, we have:

$$G_{\phi_S}(\nu) = \sum_{n=0}^{\infty} \frac{\exp(-2\pi R \lambda_R) (2\pi \lambda_R)^n}{n!} \left(\int_0^R \exp \left(-2\lambda_S \int_0^{\sqrt{R^2 - r^2}} 1 - \nu \left(\sqrt{r^2 + t^2} \right) dt \right) dr \right)^n.$$

¹By convention, we assume the value inside the inner integral to be 1 when $n = 0$.

$$= \exp \left(-2\pi\lambda_R \int_0^R 1 - \exp \left(-2\lambda_S \int_0^{\sqrt{R^2-r^2}} 1 - \nu \left(\sqrt{r^2+t^2} \right) dt \right) dr \right)$$

Using the series expansion of $\exp(\cdot)$, completes the proof.

For the second part of the lemma, without loss of generality, assume that the line passes through $(d, 0)$. A point on the line at a distance t from $(d, 0)$ is at a distance $r = \sqrt{(d+t\cos\theta)^2 + (t\sin\theta)^2}$ from the origin, where θ is the orientation of the line. Taking the PGF along all such points completes the proof.

B.2 Proof of Lemma 14

Assume that the nearest NLOS SBS is at a distance x from the typical user. Then, the ball $\mathcal{B}(o, x)$ does not contain any NLOS SBS. A randomly orientated line at a distance r from the origin, has a chord length of $2\sqrt{x^2-r^2}$, and a void probability $\exp(-2\lambda_S\sqrt{x^2-r^2})$. As a result, the probability of no points falling in this ball, averaged over the number of lines, is:

$$\begin{aligned} F_{d_{SN1}}(x) &= \sum_{n=0}^{\infty} \frac{(2\pi\lambda_R x)^n \exp(-2\pi\lambda_R x)}{n! (x^n)} \left[\int_{r_1, r_2, \dots, r_n=0}^x \prod_{i=1}^n \exp\left(-2\lambda_S \sqrt{x^2 - r_i^2}\right) dr_i \right] \\ &= \sum_{n=0}^{\infty} \frac{(2\pi\lambda_R x)^n \exp(-2\pi\lambda_R x)}{n! (x^n)} \left[\int_0^x \exp\left(-2\lambda_S \sqrt{x^2 - r^2}\right) dr \right]^n. \end{aligned}$$

This is the CDF of the distance. The PDF is then obtained by differentiating with respect to x .

For the remaining distributions, i.e., for $\{t, v\} \neq \{SN\}$, the expressions for $f_{d_{tv1}}$, can be obtained by differentiating the void probabilities of the corresponding processes [52].

B.3 Proof of Proposition 3

In Fig. 3.2, the user at O at a distance d_1 from its serving SBS AB is in NLOS if a vehicle exists in between the user and AB within a distance d_0 . From the similarity of triangles ABO and $A'B'O$, it follows that $d_0 = \frac{h_V}{h_B} d_1$. The link between O and AB is in LOS if none of the roads crossing $B'O$ is occupied by a vehicle. Now, the number of roads n passing through the region d_0 is Poisson distributed with intensity $\lambda_R d_0$. Since the fraction of the roads occupied by the

vehicles is $\lambda'_V = L_V \lambda_V$, the probability of blockage due to one road is $1 - \lambda'_V$. We have:

$$\mathcal{L}(d_1) = \mathbb{E}_n[(1 - \lambda'_V)^n] = \sum_{n=0}^{\infty} (1 - \lambda'_V)^n \frac{(\lambda_R d_0)^n \exp(-\lambda_R d_0)}{n!} = \exp\left(-\lambda'_V \lambda_R \frac{h_V}{h_B} d_1\right).$$

$\mathcal{B}(Q_R)$ is then calculated as:

$$\begin{aligned} \mathcal{B}(Q_R) &= \mathbb{E}_{d_{SL1}} [(1 - \mathcal{L}(d_{SL1})) \mathbb{1}_m(d_{SL1}, Q_R)] \\ &= \int_0^H \left(1 - \exp\left(-\lambda_R \lambda'_V \frac{h_V}{h_B} x\right)\right) f_{d_{SL1}}(x) dx, \end{aligned}$$

where $\mathbb{1}_m$ represents the indicator function for mm-wave operation.

B.4 Proof of Lemma 16

From the typical SBS, let the distance to its n -th neighbor be given by d_n (see Fig. 3.3a for notations). Thus, the distance of the typical SBS from the center of $(n - 1)$ -th and n -th neighboring SBS is given by $\bar{d}_n = \frac{d_n + d_{n-1}}{2}$. Let the depression angle from the top of the typical SBS to a user located at its boundary be ϕ . Clearly, $\phi = \arctan\left(\frac{d_a}{2h_B}\right) - \frac{\theta}{2}$. Let the distance of the point where the serving beam reaches the ground from the typical SBS be denoted by $x = h_B \tan(\phi + \theta)$. Thus, the probability of the typical SBS causing interference in the n -th neighbor is given by:

$$\begin{aligned} \mathbb{P}(x \geq \bar{d}_n) &= \mathbb{P}\left(h \tan\left(\arctan\left(\frac{d_a}{2h_B}\right) + \frac{\theta}{2}\right) \geq \frac{d_n + d_{n-1}}{2}\right), \\ &= \mathbb{P}\left(d_a \geq 2h_B \left[\tan\left(\arctan\left(\frac{d_n + d_{n-1}}{2h}\right) - \frac{\theta}{2}\right)\right]\right) \\ &= \mathbb{E}_{d_{n-1}, d_n} \left[\exp\left(-2\lambda_S h_B \frac{d_n + d_{n-1} - 2h_B \tan\frac{\theta}{2}}{2h_B + (d_n + d_{n-1}) \tan\frac{\theta}{2}}\right)\right]. \quad (\text{B.1}) \end{aligned}$$

Using the void probability and the expectation with respect to the joint distribution of d_n and d_{n-1} completes the proof. The latter is derived as follows (assuming $d_n = Y$ and $d_{n-1} = X$):

$$f_{Y|X}(y|x) f_X(x) = \frac{d}{dy} [\exp(\lambda_S (y - x))] \frac{\exp(-\lambda_S x) (\lambda_S x)^{n-2}}{(n-2)!} = \frac{\lambda_S^2 \exp(-\lambda_S y)}{(n-2)!} (\lambda_S x)^{n-2}.$$

B.5 Proof of Lemma 17

Let the typical user U_1 be located at a distance d_1 from its serving BS B_1 (the BS on the right in Fig. 3.3b). We are interested in the probability that U_1 experiences interference from the neighboring SBS B_2 serving a user U_2 . We define *spillover* as the region of interference that an SBS creates in a neighboring cell while serving a user. Now, B_2 causes spillover to the coverage area of B_1 if the extremest point of its beam crosses the cell boundary, i.e., if the position of U_2 from B_2 is greater than some value (say d'). The maximum distance of U_2 from B_2 is $\frac{d_a}{2}$. Thus, there is spillover, if the user U_2 lies in the region $d' \leq d_2 \leq \frac{d_a}{2}$. The probability that at least one such user exists is obtained using the void probability of the user PPP and is given by $(1 - \exp(-\lambda_U (\frac{d_a}{2} - d')))$. The extent of spillover (s) to the coverage area of B_1 , from B_2 serving U_2 is:

$$s = GC - \frac{d_a}{2} = h \tan\left(\frac{\theta}{2} + \phi\right) - \frac{d_a}{2} = h \tan\left(\frac{\theta}{2} + \arctan\left(\frac{d_2}{h}\right)\right) - \frac{d_a}{2}, \quad (\text{B.2})$$

where ϕ is the angle of depression from the top of B_2 to U_2 on the ground. Now, d' is then obtained from the condition $s = 0$, i.e., the location of U_2 , beyond which the coverage area of B_1 experiences spillover from B_2 . This results in: $d' = h \tan\left(\arctan\left(\frac{d_a}{2h}\right) - \frac{\theta}{2}\right)$. To keep our analysis tractable, we assume that B_2 does not create a spillover in the coverage region of B_1 , when serving the users on its left. For practical values, this condition always holds. For example, with $h_B = 10$ m, and θ of 10 degrees, we have $d_a \geq 1.75$ m. For the SBS densities considered throughout this chapter ($\lambda_S < 100 \text{ km}^{-1}$), this holds with a high probability (≥ 0.85). Thus we have: $d' \geq 0 \implies d_a \geq 2h \tan\left(\frac{\theta}{2}\right)$. The probability that U_1 is located in the spillover region, given that the spillover is s , is:

$$\mathbb{P}(U_1 \in s) = \begin{cases} \mathbb{P}(d_1 \geq \frac{d_a}{2} - s) = \exp(-\lambda_U (\frac{d_a}{2} - s)); & s \leq \frac{d_a}{2} \\ 1; & s \geq \frac{d_a}{2} \end{cases}, \quad (\text{B.3})$$

Now we substitute s from (B.2) in (B.3), and take the expectation with respect to d_a and d_2 : $f_{d_a, d_2}(x, y) = \lambda_U \lambda_S \exp(-\lambda_U (\frac{x}{2} - y)) \exp(-\lambda_S x)$, $y \leq \frac{x}{2}$.

B.6 Proof of Proposition 4

The user association probabilities with a LOS and NLOS MBS and LOS SBS are:

$$\begin{aligned}\mathcal{P}_{ML} &= \mathcal{T} \mathbb{P}(P_{ML1} \geq P_{SL1}, P_{ML1} \geq P_{SN1}), \\ \mathcal{P}_{MN} &= (1 - \mathcal{T}) \mathbb{P}(P_{MN1} \geq P_{SL1}, P_{MN1} \geq P_{SN1}), \\ \mathcal{P}_{SL} &= \mathcal{T} \mathbb{P}(P_{SL1} \geq P_{ML1}, P_{SL1} \geq P_{SN1}) + (1 - \mathcal{T}) \mathbb{P}(P_{SL1} \geq P_{MN1}, P_{SL1} \geq P_{SN1}),\end{aligned}$$

where $\mathcal{T} = \mathbb{E}[\mathbf{1}(ML)]$ is the probability of the existence of at least one LOS MBS. In our model, a signal from a LOS MBS will be received with higher power than one from any NLOS MBS. In the following, we show how to calculate \mathbb{P}_{ML} . The other probabilities follow similarly.

$$\begin{aligned}\mathcal{P}_{ML} &= \mathbb{E}[\mathbf{1}(ML)] \mathbb{P}(P_{ML1} > P_{SL1}, P_{ML1} > P_{SN1}) \\ &= \mathbb{E}[\mathbf{1}(ML)] (\mathbb{P}(P_{ML1} > P_{SL1}, P_{SL1} > P_{SN1}) + \mathbb{P}(P_{ML1} > P_{SN1}, P_{SN1} > P_{SL1})) \\ &= \mathbb{E}[\mathbf{1}(ML)] \left(\mathbb{P}\left(K_\mu P_M d_{ML1}^{-\alpha_{ML\mu}} > K_\mu P_S d_{SL1}^{-\alpha_{SL\mu}}, K_\mu P_S d_{SL1}^{-\alpha_{SL\mu}} > K_\mu P_S d_{SN1}^{-\alpha_{SN\mu}}\right) + \right. \\ &\quad \left. \mathbb{P}\left(K_\mu P_M d_{ML1}^{-\alpha_{ML\mu}} > K_\mu P_S d_{SN1}^{-\alpha_{SN\mu}}, K_\mu P_S d_{SN1}^{-\alpha_{SN\mu}} > K_\mu P_S d_{SL1}^{-\alpha_{SL\mu}}\right) \right) \\ &= \mathbb{E}[\mathbf{1}(ML)] \left(\mathbb{E}_{d_{ML1}, d_{SN1}} \left[\exp\left(-2\lambda_S \left(d_{SN1}^{\frac{\alpha_{SN\mu}}{\alpha_{SL\mu}}} - \left(\frac{P_S}{P_M} d_{ML1}^{\alpha_{ML\mu}}\right)^{\frac{1}{\alpha_{SL\mu}}}\right)\right) \mathcal{T}_1(d_{ML1}) \right] + \right. \\ &\quad \left. \mathbb{E}_{d_{ML1}, d_{SL1}} \left[\left(F_{d_{SN1}}\left(d_{SL1}^{\frac{\alpha_{SN\mu}}{\alpha_{SL\mu}}}\right) - F_{d_{SN1}}\left(\left(\frac{P_S}{P_M} d_{ML1}^{\alpha_{ML\mu}}\right)^{\frac{1}{\alpha_{SN\mu}}}\right) F_{d_{SN1}}\left(x^{\frac{\alpha_{SL\mu}}{\alpha_{SN\mu}}}\right) \right) \right] \right).\end{aligned}$$

B.7 Proof of Proposition 5

The probability of mm-wave association based on instantaneous power RAT selection is:

$$\begin{aligned}\mathcal{P}_m &= \mathbb{E}[\mathcal{L}(d_{SL1})] \mathbb{P}(r = mm | t = SL) = \mathbb{E}[\mathcal{L}(d_{SL1})] \mathbb{P}\left(d_{SL1} < \left(\frac{K_m G_0 Q_R}{K_\mu}\right)^{\frac{1}{\alpha_{SLm} - \alpha_{SL\mu}}}\right) \\ &= \frac{2h_B \lambda_S}{\lambda'_V h_V \lambda_R + 2h_B \lambda_S} \left[1 - \exp\left(-2\lambda_S \left(\frac{K_m G_0 Q_R}{K_\mu}\right)^{\frac{1}{\alpha_{SLm} - \alpha_{SL\mu}}}\right) \right], \quad (\text{B.4})\end{aligned}$$

where $\mathbb{E}[\mathcal{L}(d_{SL1})]$ refers to the average probability that the user experiences a LOS path from the strongest SBS, which is calculated by taking the expectation of $\mathcal{L}(d_{SL1})$ (see Proposition 3) with respect to the distance d_{SL1} , i.e.,

$$\mathbb{E}[\mathcal{L}(d_{SL1})] = \mathbb{E}_{d_{SL1}} \left[\exp\left(-\lambda'_V \lambda_R \frac{h_V}{h_B} d_{SL1}\right) \right] = \frac{2h_B \lambda_S}{\lambda'_V h_V \lambda_R + 2h_B \lambda_S}.$$

In case of association based on averaged power RAT selection, we have:

$$\begin{aligned}\bar{\mathcal{P}}_m &= \mathbb{P}(Q_R K_m G_0 P_S d_{SL1}^{-\alpha_{SLm}} \mathbb{P}_L(d_{SL1}) > K_\mu P_S d_{SL1}^{-\alpha_{SL\mu}}), \\ &= \mathbb{P}\left(d_{SL1} \leq \frac{h_B(\alpha_{SLm} - \alpha_{SL\mu})}{\lambda'_V \lambda_S h_V} \mathcal{W}\left(\frac{\lambda'_V \lambda_S h_V}{h_B(\alpha_{SLm} - \alpha_{SL\mu})} \left(\frac{K_\mu}{K_m G_0 Q_R}\right)^{\frac{1}{\alpha_{SL\mu} - \alpha_{SLm}}}\right)\right).\end{aligned}$$

B.8 Proof of Theorem 1

A user located at d_{SL1} from its serving SBS experiences mm-wave interference from an interfering SBS located at d_{SL2} from it, when 1) the user lies in the spillover region of the interfering SBS and 2) the interfering link is not blocked by moving vehicles. Accordingly:

$$\begin{aligned}SINR_{SLm} &= \frac{P_S G_0 K_m h_{mSL1} d_{SL1}^{-\alpha_{SLm}}}{\sigma_{mm}^2 + P_S G_0 K_m h_{mSL2} d_{SL2}^{-\alpha_{SLm}}} p_G(d_{SL1}, d_{SL2}) \mathcal{L}(d_{SL1}) \mathcal{L}(d_{SL2}) + \\ &\quad \frac{P_S G_0 K_m h_{SL1} d_{SL1}^{-\alpha_{SLm}}}{\sigma_{mm}^2} \mathcal{L}(d_{SL1}) (1 - p_G(d_{SL1}, d_{SL2}) \mathcal{L}(d_{SL2})),\end{aligned}$$

where $\mathcal{L}(d_{SL1})$ and $\mathcal{L}(d_{SL2})$ are given by Proposition 3, and $p_G(d_{SL1}, d_{SL2})$ is the probability that the typical user experiences mm-wave interference. Although p_G depends on d_{SL1} and d_{SL2} , the SINR coverage probability can be approximated by using the expression of \bar{p}_G from (3.7) as:

$$\begin{aligned}\mathbb{P}(SINR_{SLm} \geq \gamma) &\stackrel{(a)}{\geq} \mathbb{P}\left(\frac{P_S G_0 K_m h_{mSL1} d_{SL1}^{-\alpha_{SLm}} \mathcal{L}(d_{SL1})}{\sigma_{mm}^2 + P_S G_0 K_m h_{mSL2} d_{SL2}^{-\alpha_{SLm}} p_G(d_{SL1}, d_{SL2}) \mathcal{L}(d_{SL2})} \geq \gamma\right) \\ &\stackrel{(b)}{\geq} \mathbb{P}\left(\frac{P_S G_0 K_m h_{mSL1} d_{SL1}^{-\alpha_{SLm}} \mathcal{L}(d_{SL1})}{\sigma_{mm}^2 + P_S G_0 K_m h_{mSL2} d_{SL2}^{-\alpha_{SLm}} \bar{p}_G \mathcal{L}(d_{SL2})} \geq \gamma\right) \\ &= \mathbb{P}\left(h_{mSL1} \geq \frac{\gamma (\sigma_{mm}^2 + P_S G_0 K_m h_{mSL2} d_{SL2}^{-\alpha_{SLm}} \bar{p}_G \mathcal{L}(d_{SL2}))}{P_S G_0 K_m d_{SL1}^{-\alpha_{SLm}} \mathcal{L}(d_{SL1})}\right),\end{aligned}$$

The steps (a) and (b) follow from Jensen's inequality and the final expression follows by taking the PGF with respect to the channel power h_{mSL1} . Subsequently, taking the expectation with respect to the joint distribution of $d_{SL1} = X$ and $d_{SL2} = Y$, we complete the proof:

$$\begin{aligned}f_{X,Y}(x, y) &= f_{Y|X}(y|x) f_X(x) = \frac{-\partial}{\partial y} \mathbb{P}(Y < y | X = x) \frac{-\partial}{\partial x} \mathbb{P}(X < x) \\ &= \frac{-\partial}{\partial y} [\exp(-\lambda_S(x + y - 2x))] \frac{-\partial}{\partial x} [\exp(-2\lambda_S x)] = 2\lambda_S^2 \exp(-\lambda_S(x + y)).\end{aligned}$$

The sub-6GHz association cases follow on similar lines as given in [45].

Appendix C

Proofs of Chapter 6

C.1 Proof of Theorem 2

First note that all the terms d_{R_i} and d_{L_i} can be represented in terms of d_a and d_{L_1} , where d_a is the random variable representing the inter-SBS distance by the equivalence: $d_{R_N} = d_a$ and hence, we have, for a given θ :

$$N = \left\lceil \frac{1}{\theta} \arctan \left(\frac{d_a - d_{L_1}}{h} \right) \right\rceil$$

Beam-selection error occurs for the typical user in case it lies outside \mathcal{C}_i . Thus, the probability of beam-selection error in case the typical user is estimated to be located at x , is computed as:

$$\begin{aligned} \mathcal{P}_{BS_i}(x) &= \mathbb{P}(\hat{x} < d_{L_i}) + \mathbb{P}(\hat{x} > d_{R_i}) \\ &= 1 - \mathcal{Q} \left(\frac{d_{L_i} - x}{\sigma_d^2} \right) + \mathcal{Q} \left(\frac{d_{R_i} - x}{\sigma_d^2} \right) \end{aligned} \quad (\text{C.1})$$

Accordingly, the average beam-selection error of any user for which the i -th beam is selected for service is given by:

$$\bar{\mathcal{P}}_{BS_i} = \int_{d_{L_i}}^{d_{R_i}} \mathcal{P}_{BS_i}(x) f_d(x) dx; \quad \text{with } d_{R_N} = d_a. \quad (\text{C.2})$$

Subsequently, the total beam-selection error for the positioning based beam-selection scheme with a beam-dictionary size of N is calculated as:

$$\bar{\mathcal{P}}_{BS} = \sum_{i=1}^N \bar{\mathcal{P}}_{BS_i} \quad (\text{C.3})$$

C.2 Proof of Theorem 3

The SINR Coverage probability at a threshold T in case of no beam-selection error is calculated as:

$$\begin{aligned}
& \mathbb{P}(SINR \geq T) \\
&= \mathbb{P}\left(\frac{P_t K G d_1^{-\alpha_L} h_1}{\sigma_{mm}^2 + P_t K g \left(\sum_{i \in \phi_L \setminus \{d_1\}} d_i^{-\alpha_L} h_i + \sum_{j \in \phi_N} d_j^{-\alpha_N} h_j\right)} \geq T\right) \\
&= \mathbb{P}\left(h_1 \geq \frac{\gamma \sigma_{mm}^2 + P_t K g \left(\sum_{i \in \phi_L \setminus \{d_1\}} d_i^{-\alpha_L} h_i + \sum_{j \in \phi_N} d_j^{-\alpha_N} h_j\right)}{P_t K G d_1^{-\alpha_L}}\right) \\
&\stackrel{.8}{=} \mathbb{E}_{\phi_L, \phi_N, h_i, h_j} \left[\exp\left(-\frac{T \sigma_{mm}^2}{P_t K G d_1} - \frac{T g \sum_{i \in \phi_L \setminus \{d_1\}} d_i^{-\alpha_L} h_i}{G d_1^{-\alpha_L}}\right. \right. \\
&\quad \left. \left. - .8 \frac{T g \sum_{j \in \phi_N} d_j^{-\alpha_N} h_j}{G d_1^{-\alpha_L}}\right)\right] \\
&= \exp\left(-\frac{T \sigma_{mm}^2}{P_t K G d_1}\right) \mathbb{E}_{h_i, \phi_L \setminus \{d_1\}} \left[\exp\left(-\frac{T g \sum_{i \in \phi_L \setminus \{d_1\}} d_i^{-\alpha_L} h_i}{G d_1^{-\alpha_L}}\right)\right] \\
&\quad \mathbb{E}_{h_j, \phi_N} \left[\exp\left(-\frac{T g \sum_{j \in \phi_N} d_j^{-\alpha_N} h_j}{G d_1^{-\alpha_L}}\right)\right] \tag{C.4}
\end{aligned}$$

Now the terms corresponding to the LOS and the NLOS case can be evaluated separately as:

$$\begin{aligned}
& \mathbb{E}_{h_i, \phi_L \setminus \{d_1\}} \left[\exp\left(-\frac{T g \sum_{i \in \phi_L \setminus \{d_1\}} d_i^{-\alpha_L} h_i}{G d_1^{-\alpha_L}}\right)\right] \\
&= \mathbb{E} \left[\prod_{i \in \phi_L \setminus \{d_1\}} \mathbb{E}_{h_i} \left[\exp\left(-\frac{T g \sum_{i \in \phi_L \setminus \{d_1\}} d_i^{-\alpha_L} h_i}{G d_1^{-\alpha_L}}\right)\right] \right] \tag{C.5a}
\end{aligned}$$

$$= \exp\left(\int_{d_1}^{d_S} 1 - \mathbb{E}_h \left[\exp\left(-\frac{T g x^{-\alpha_L} h}{G d_1^{-\alpha_L}}\right)\right] 2\lambda x dx\right) \tag{C.5b}$$

$$= \exp\left(-\int_{d_1}^{d_S} \frac{T g x^{-\alpha_L}}{G d_1^{-\alpha_L} + T g x^{-\alpha_L}} 2\lambda x dx\right) \tag{C.5c}$$

Similarly,

$$\begin{aligned}
& \mathbb{E}_{h_j, \phi_N} \left[\exp\left(-\frac{T g \sum_{j \in \phi_N} d_j^{-\alpha_N} h_j}{G d_1^{-\alpha_L}}\right)\right] \\
&= \exp\left(-\int_{d_S}^{\infty} \frac{T g x^{-\alpha_N}}{G d_1^{-\alpha_L} + T g x^{-\alpha_N}} 2\lambda x dx\right) \tag{C.6}
\end{aligned}$$

In case of beam selection error, the expressions are modified by replacing G with g . Conditioning on d_1 lying between d_{L_i} and d_{R_i} completes the proof.

Appendix D

Accurate Characterization of Dynamic Cell Load in Noise-Limited Random Cellular Networks

In this Appendix we present some extension on the topic of dynamic cell load discussed in Chapter 2.

D.1 Introduction

Stochastic geometry has emerged as an important tool for modeling and analyzing large scale wireless cellular networks [53], wherein the performance is typically characterized by studying metrics such as SINR coverage probability and user throughput. To effectively model the user throughput and to efficiently dimension a cellular network from the operators' perspective, the characterization of the cell load is necessary. The existing literature in stochastic geometry models the cell load by considering the average number of associated full buffer users, uniformly distributed over the cell area, see e.g., [53, 113]. This is not realistic since it ignores the effect of dynamic traffic on the user distribution: users with low data rate tend to stay longer in the system, and as a result, the user distribution becomes inhomogeneous in space.

However, studying dynamic traffic using elements of queuing theory in the context of stochastic geometry based analyses is still an open problem [53]. In this regard, Blaszczyszyn et al. [57], have introduced the mean cell approach which avoids extensive simulations by approximating the spatial SINR distribution of a cell with the SINR distribution of the typical user. Thus, in essence,

the mean cell approach characterizes the load of the cell containing the typical user, i.e., the *zero cell* [52]. Although this approach enables modeling the cell load, it may lead to intractable expressions consisting of multiple integrals for evaluation of the SINR coverage probability. Moreover, a characterization of the load of the zero cell is not a reliable metric for evaluating the network wide load distribution since the zero cell is statistically larger than a random cell drawn from the population of cells, i.e., a *typical cell*. To understand this intuitively, one can assume a random sample point and select the cell containing the point. By stationarity, the distribution of this cell coincides with that of the zero cell. Since the sample point tends to fall with greater probability into larger cells, the zero cell tends to be larger than the typical cell. In this appendix, for the case of noise-limited networks, we provide approximations for the network load by characterizing the load of the typical cell. This provides a more realistic characterization of the network load. This noise-limited assumption can be applied to a variety of contexts. For example, in millimeter wave (mm-wave) networks that utilize directional antennas and advanced interference management mechanisms, the performance tends to be noise-limited. Singh et.al [101] have shown the validity of the noise-limited network assumption in mm-wave mesh networks. Furthermore, this noise-limited scenario enables us to visualize our results in light of the seminal work of Bonald et al. [74] who derived the cell load expressions for a single cell with dynamic traffic.

The contribution of this Appendix is as follows.

- We obtain a closed-form expression for the CDF of the load of the typical cell in a noise-limited network by considering dynamic traffic. We use it to obtain the fraction of stable cells for a given deployment density of small cells.
- Then, we obtain a single integral-based approximation, and a closed-form expression, for the average load of the typical cell. We show that the first approximation models the cell load from a network perspective more accurately than the mean cell approach. Whereas, the closed-form expression provides a faster and more tractable alternative to calculate the network load, since it does not require evaluation of integrals.

The rest of the Appendix is organized as follows. In Section D.2 we introduce the single tier network and the associated parameters. In Section D.3, we present our main results on the CDF and the average of the load of the typical

cell of the network. In Section D.4, we present the results on the stable fraction of the network and we show the accuracy of our derived approximations with respect to Monte-Carlo simulations. Finally, the Appendix concludes in Section D.5.

D.2 System Model

We consider a single-tier cellular network equipped with advanced interference management algorithms, so that the user performance is noise-limited.

The positions of the BS are modeled as points of a PPP ϕ with intensity λ [m^{-2}]. The BSs operate with a transmit power P_t , and the product of the gains of the antennas at the transmitter and the receiver is G_0 . We consider a fast fading that is Rayleigh distributed with variance equal to one. Furthermore, we assume a path loss model where the power at the origin received from a BS located at a distance r is given by $P_r = K \cdot P_t \cdot h \cdot G_0 \cdot r^{-\alpha}$, where K is the path loss coefficient, h is the exponentially distributed fading power, and α is the path loss exponent. Thus, the average SNR can be written as $\frac{K \cdot P_t \cdot G_0 \cdot r^{-\alpha}}{N_0 \cdot B} = \xi r^{-\alpha}$, where $\xi = \frac{K \cdot P_t \cdot G_0}{N_0 \cdot B}$ is the average SNR at 1 m. N_0 and B are the noise power density and the operating bandwidth, respectively.

In this network, we assume that the users arrive in the system, download a file, and leave the system. Any new download by the same user is considered as a new user. The arrival process of the new users is Poisson distributed with an intensity λ_U [$\text{users} \cdot \text{s}^{-1} \cdot \text{m}^{-2}$] and these new users are uniformly distributed over the network area A . The average file size is σ [bits/user]. When there are n users simultaneously served by a BS, the available resources are equally shared between them in a round robin fashion. Accordingly, we define the traffic density w in the network as $w = \lambda_U \cdot \sigma$ [$\text{bits} \cdot \text{s}^{-1} \cdot \text{m}^{-2}$]. Note that, while the user arrivals are uniform in space, as the space-time process evolves, users farther from the serving BSs, i.e., characterized by lower data rates, stay longer in the system, resulting in an inhomogeneous distribution of active users in the network.

D.3 Characterization of the Network Load

D.3.1 Static vs Dynamic Load

Before proceeding to our main results, it is necessary to discuss the distinction of dynamic cell-load characterization as compared to the approaches that model the cell load as simply the average number of associated users to a BS [70]. For this we compare the downlink user throughput using the two approaches to study the difference. First, in our system model, we calculate the dynamic cell load using the study of Bonald et.al. [74], say $\bar{\rho}$. Then use it to calculate the downlink user throughput R_{dyn} , which is given by [74]:

$$R_{dyn} = w \frac{1 - \bar{\rho}}{\bar{\rho}} \cdot A, \quad (\text{D.1})$$

where, the area of the typical cell A is approximated as $A = \frac{1}{\lambda}$, and the average number of active users in the dynamic traffic model [57] is: $N = \frac{\bar{\rho}}{1 - \bar{\rho}}$. To compare R_{dyn} with that obtained using the analyses in the existing literature [113, 70], we assume that the users are located homogeneously in each cell of the network following a PPP with an average of N users per cell. Using this assumption, we carry out simulations to obtain the downlink user throughput T_{PPP} as:

$$R_{PPP} = \mathbb{E}_n \left[\frac{B}{n} \log_2 (1 + SINR) \right], \quad (\text{D.2})$$

where the expectation is taken with respect to the number of users in each cell (n), which is Poisson distributed with mean N , as well as the SINR of each user in each cell. The difference between R_{dyn} and R_{PPP} is highlighted in Fig. D.1. Even though the average number of users in both cases are same, as the space-time process with dynamic traffic evolves, the user distribution is no longer homogeneous in space which is not taken into account in existing studies.

D.3.2 Preliminaries

In case of single-tier random cellular networks, the cell of a BS is given by the Poisson-Voronoi (PV) partition of the space [52]. In the \mathbb{R}^2 plane, the PV region of a BS located at $x_0 \in \phi$ is: $\mathcal{A} = \{y : \|y - x_0\| < \|y - x_i\|; \forall x_i \in \phi \setminus \{x_0\}\}$.

The mosaic of the cells formed for all such x_0 from a PPP is called a PV network. To investigate the geometry-dependent characteristics of the cells (e.g., the cell load), in a stationary random PV network, it is imperative to

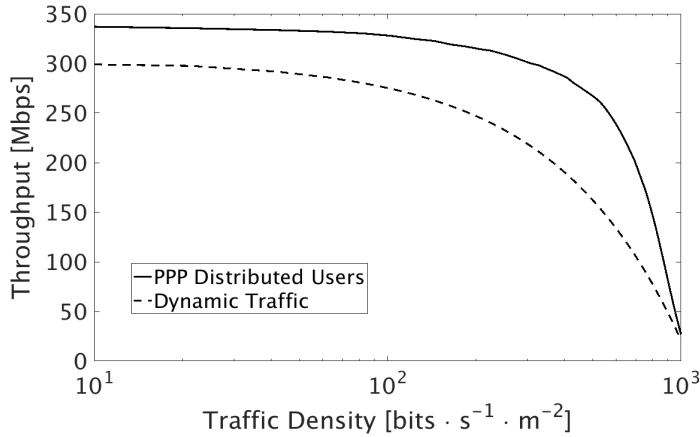


FIGURE D.1: Throughput comparison of mean cell approach with PPP distributed users.

define the notion of the ‘average’ cell. Thus, we recall the following definitions that provide a characterization of the average cell.

Definition 5. *The zero cell or the Crofton cell of the PV network is defined as the cell containing a given fixed point in its interior [52].*

Definition 6. *The typical cell of a PV network is defined as a cell selected at random within a large region of the network with equal chances for each cell to be picked [52]. Thereafter, the network is translated so that the center of the typical cell becomes the origin.*

The zero cell versus typical-cell approaches of modeling the network performance corresponds to the evaluation from the perspectives of the user and the network operator, respectively. Hence, for the case of analyzing the network load, the zero cell perspective is not an accurate way of characterization. In what follows, we first define the load of the typical-cell and then, discuss how the load of the zero cell is generally obtained. Then we present our analysis to characterize the load of the typical cell and hence the average network load.

Average Load of the Typical Cell

The load of the typical cell in the network can be calculated as:

$$\rho = \int_{\mathcal{A}} \frac{w}{C(s)} ds, \quad (\text{D.3})$$

where $C(s)$ is the rate that a user located at s receives in the typical cell \mathcal{A} , calculated using the Shannon formula. The random variable ρ characterizes the load of the cell centered at x_0 , and depends on the shape and size of \mathcal{A} .

The average load of the typical cell is then calculated by taking the expected values of loads for different realizations of the PPP itself: $\bar{\rho} = \mathbb{E}[\rho]$,

Mean Cell Approximation

In case of PV cells, the average load of the typical cell is generally difficult to evaluate because the shape and size of the typical cells is random. However, by using the ergodicity of the PPP, the area of the typical cell can be approximated as $\frac{1}{\lambda}$ [70]. Then, by assuming the network to be noise-limited, the average load can be approximated using the mean cell approach [57], as:

$$\bar{\rho}_{MC} = \int_T \frac{w}{B\lambda \log_2(1+T)} p(T) dT, \quad (\text{D.4})$$

where the expectation is taken with respect to the SNR (T) variations averaged over the fast fading, and $p(T) = \frac{-d\mathbb{P}_C(T)}{dT}$ is the PDF of the SNR of the typical user obtained by differentiating the SNR coverage probability, $\mathbb{P}_C(T)$. Thus, the cell load can be calculated numerically, given the SNR distribution.

However in the mean cell approach, as the expectation is taken with respect to the SNR variations of the typical user, it calculates the expected load of the zero cell which is statistically larger than the typical cell [52]. Thus, the mean cell approach, always overestimates the load of the typical cell. In the next sections, we propose a new approximation, which is both more accurate and more tractable. First, we derive the CDF of the cell load of the typical cell using the distribution of its area. Then, we obtain a single-integral-based and a closed-form approximation for the average load of the typical cell.

D.3.3 Distribution of the Area of the Typical Cell

The reduced area of a PV cell is defined as [52] :

$$s = A/\mathbb{E}[A], \quad (\text{D.5})$$

where A is the area of the typical cell, and $\mathbb{E}[\cdot]$ is the expectation operator. The PDF of the reduced area of the typical PV cell in two dimensions is given by [114]:

$$f_s(x) = \frac{343}{15} \sqrt{\frac{7}{2\pi}} x^{5/2} \exp\left(-\frac{7}{2}x\right). \quad (\text{D.6})$$

Using this, we can obtain the CDF of the area as given below.

Lemma 22. *The CDF of the area of the typical PV cell for a PPP with intensity λ is given by:*

$$F_A(x) = \frac{343}{15} \sqrt{\frac{7}{2\pi}} \left(\frac{2}{7}\right)^{7/2} \gamma_{inc}\left(\frac{7\lambda x}{2}, \frac{7}{2}\right), \quad (\text{D.7})$$

where $\gamma_{inc}(\cdot)$ is the lower incomplete gamma function given by: $\gamma_{inc}(x, a) = \int_0^x t^{a-1} \exp(-t) dt$.

Proof. The CDF can be easily derived using the relation (D.5) and integrating (D.6). \square

D.3.4 Distribution of the Load of the Typical Cell

For obtaining the CDF of the load of the typical cell, we assume that the shape of PV cells is circular. Although in a real PV network, almost surely no circular cells occur, our results show that the circular assumption does not greatly deteriorate the derived approximation. Accordingly, the load of a typical cell (D.3) with area A is approximated as [74]:

$$\rho_{TC}(A) \approx \rho_{AP}(A) = \int_0^{2\pi} \int_0^{\sqrt{\frac{A}{\pi}}} \frac{wr}{B\lambda \log_2(1 + \xi r^{-2})} dr d\theta.$$

Theorem 4. *The distribution of the load of the typical cell, ρ is given by:*

$$F_\rho(l) = F_A \left(\pi \left(\frac{1}{\xi} \exp \left(-\frac{\alpha}{2} Ei^{-1} \left(-\frac{l}{K'} \right) \right) \right) \right)^{\frac{-2}{\alpha}} \quad (\text{D.8})$$

where $K' = \frac{4w\pi \ln(2)\xi}{\alpha^2 B\lambda} \xi^{\frac{2}{\alpha}}$ and the symbol $Ei^{-1}(x)$ is the inverse of the exponential integral. For the special case of $\alpha = 2$, it is approximated as:

$$F_\rho(l) \approx F_A \left(\frac{\xi\pi \left(1 + \exp \left(-\frac{l}{K_1} \right) \right)}{\exp \left(-\frac{l}{K_1} \right)} \right), \quad (\text{D.9})$$

where $K_1 = \frac{w\pi \ln(2)\xi}{B\lambda}$.

Proof. According to our assumption of high SNR for dense networks, we can approximate $1 + \xi r^{-\alpha}$ as $\xi r^{-\alpha}$. Substituting $\ln(\xi r^{-\alpha}) = y$, we have:

$$\rho_{AP}(A) = K' \int_{\ln(\xi(\pi/A)^{\frac{\alpha}{2}})}^{\infty} \frac{\exp(-y)}{y} dy$$

$$= K' E_1 \left(\frac{2}{\alpha} \ln \left(\xi \left(\frac{\pi}{A} \right)^{\frac{\alpha}{2}} \right) \right), \quad (\text{D.10})$$

where, $K' = \frac{4w\pi \ln(2)\xi}{\alpha^2 B \lambda} \xi^{\frac{2}{\alpha}}$ and $E_1(\cdot)$ is the exponential integral function [115]. The CDF is then simply obtained by some algebraic manipulations of the expression $\mathbb{P}(\rho_{AP}(A) \leq l)$. For the special case of $\alpha = 2$, the CDF of the approximated load of the typical cell $\rho_{AP}(A)$ is derived as:

$$\mathbb{P}(\rho_{AP}(A) \leq l) = \mathbb{P} \left(-\ln(\xi \pi A^{-1}) \leq \text{Ei}^{-1} \left(-\frac{l}{K_1} \right) \right),$$

where, the symbol $\text{Ei}^{-1}(x)$ is given by $\text{Ei}(x) = -E_1(-x)$. Although an explicit expression for $\text{Ei}^{-1}(\cdot)$ does not exist, Pecina [116] provided piece-wise functions to approximate $\text{Ei}^{-1}(x)$ for different ranges of x . The asymptotic approximation for $\frac{-1}{K_1} \rightarrow 0$ is [116]:

$$\text{Ei}^{-1} \left(-\frac{l}{K_1} \right) \approx \frac{\exp \left(-\frac{l}{K_1} \right)}{1 + \exp \left(-\frac{l}{K_1} \right)}.$$

$$\bar{\rho}'_{AP} = \int_0^\infty \lambda \frac{2\pi \ln(2)\xi}{B} F_1(A) \frac{343}{15} \sqrt{\frac{7}{2\pi}} (A\lambda)^{5/2} \exp \left(-\frac{7}{2} A\lambda \right) dA \quad (12)$$

$$\text{where, } F_1(A) = \begin{cases} \frac{\exp(-\ln(\frac{\xi\pi}{A})) \ln \left(\frac{G_0}{\ln(\frac{\xi\pi}{A})} + G_0 + (1-G_0)\beta(\ln(\frac{\xi\pi}{A})) \right)}{G_0 + (1-G_0) \exp \left(\frac{-\ln(\frac{\xi\pi}{A})}{1-G_0} \right)}; & A \leq \frac{\pi\xi}{\exp(1)} \\ -\gamma - \ln \left(-\ln \left(\frac{\xi\pi}{A} \right) \right) + \left(-\ln \left(\frac{\xi\pi}{A} \right) \right) - \frac{(-\ln(\frac{\xi\pi}{A}))^2}{8}; & A > \frac{\pi\xi}{\exp(1)} \end{cases}$$

In our analysis, we assume $P_t = 30$ dBm, a noise density of -174 dBm/Hz, and $B = 1$ GHz. The path loss coefficient K is derived from the Umi model for data transmission [36]. As the load l varies from $0 \leq l \leq 1$, for $G_0 = 20$ dB, and $\lambda = 1e - 5 \text{ m}^{-2}$, we have $0 \leq \frac{l}{K_1} \leq 1e - 8$. Thus, our asymptotic approximation is valid. Using this approximation completes the proof. \square

D.3.5 Proposed Approximations for the Average Load of the Typical Cell

Using the distribution of (D.7) and (D.10) we obtain the following approximation of the average load:

$$\bar{\rho}_{AP} = \int_0^\infty K' E_1 \left(\frac{2}{\alpha} \ln \left(\xi \left(\frac{\pi}{A} \right)^{\frac{\alpha}{2}} \right) \right) f_A(A) dA, \quad (\text{D.11})$$

where $f_A(x) = \frac{dF_A(x)}{dx}$. Since solving (D.11) is tedious, we provide two results to approximate the average load of the typical cell for the special case of $\alpha = 2^1$. In Section D.4, we will highlight the advantage of each approximation.

EI based Approximation

Theorem 5. *The average load of the typical cell can be approximated as (12).*

Proof. We rely on an approximation of the exponential integral provided by Barry et. al. [115]:

$$E_1(x) = \frac{\exp(-x) \ln \left(\frac{K_2}{x} + K_2 + (1 - K_2)\beta(x) \right)}{K_2 + (1 - K_2) \exp \left(\frac{-x}{1 - K_2} \right)}, \quad (\text{D.13})$$

where, $K_2 = \exp(-\gamma) = 0.56$, $\beta(x) = 1 - \frac{1}{(h(x)+bx)^2}$,

$$h(x) = \frac{1}{1 + x\sqrt{x}} + \frac{0.46x\sqrt{\frac{31}{26}}}{1 + 0.43x\sqrt{\frac{31}{26}}}, b \approx 1.04207,$$

and γ is the Euler's constant. This interpolated version of the exponential integral provides a good approximation for $1 \leq x \leq 50$. This corresponds to the range

$$\frac{\pi\xi}{\exp(50)} \leq A \leq \frac{\pi\xi}{\exp(1)}. \quad (\text{D.14})$$

For the region of A greater than this range, we use the asymptotic expansion of $E_1(x)$ as:

$$E_1(x) = -\gamma - \ln(x) + x - \frac{x^2}{8} + \dots \quad (\text{D.15})$$

¹For dense deployments, the serving BS is generally in LOS which has a path-loss exponent close to 2 for sub-6GHz [78] and mm-wave [36] transmissions.

For practical ranges of cell sizes, the lower bound in (D.14) always holds (e.g., with $G_0 = 0$ dB, the lower bound on the area is $A \geq 2e - 8$). Now, substituting (D.10) in (D.11) and using (D.13) and (D.15) to evaluate the integral, completes the proof. \square

CF Approximation

Substituting $\ln\left(\frac{\xi\pi}{A}\right) = t$, the approximated average load of the typical cell (D.11) becomes:

$$\bar{\rho}_{AP} = \chi_2 \int_{-\infty}^{\infty} E_1(t) \exp\left(-\frac{7}{2}t\right) F_2(t) dt, \quad (\text{D.16})$$

where $\chi_2 = \frac{w\pi \ln(2)\xi}{\lambda B} (\xi\pi\lambda)^{3.5}$ and $F_2(t) = \exp\left(-\frac{7\lambda\xi\pi}{2} \exp(-t)\right)$.

Now, a closed-form solution to this integral does not exist. However, in what follows, we derive an approximate closed-form solution for the average load of the typical cell, which we show to be very accurate in Section D.4.

Theorem 6. *The average load of the typical cell is approximated by the closed-form expression:*

$$\bar{\rho}_{AP}'' = \chi_2 (I_1(t_2) - I_1(t_1) + (y_1 - 1)I_2(t_2) - y_1 I_2(t_1))$$

where,

$$\begin{aligned} I_1(x) &= \left(\frac{2}{7}\right)^2 (E_1(4.5x) - (1 + 3.5x)e^{-3.5x}E_1(x) + \left(\frac{7}{9}\right) \exp(-4.5x)) \\ I_2(x) &= \frac{2}{7} [E_1(4.5x) - e^{-3.5x}E_1(x)], \text{ and, } t_1 = -\ln\left(-\frac{2}{7\lambda\xi\pi} \ln(0.1)\right), \\ t_2 &= -\ln\left(-\frac{2}{7\lambda\xi\pi} \ln(0.9)\right) \text{ and, } y_1 = \frac{0.9t_1 - 0.1t_2}{t_1 - t_2}. \end{aligned}$$

Proof. We can approximate $F_2(t)$, with a piece-wise defined ramp and step function as follows:

$$\tilde{F}_2(t) = \begin{cases} 0; & t \leq t_1, \\ \frac{0.8t}{t_2 - t_1} + y_1; & t_1 < t \leq t_2, \\ 1; & t > t_2 \end{cases} \quad (\text{D.17})$$

where t_1 and t_2 are the points corresponding to 10 and 90 percentile values of $F_2(t)$, and y_1 is the intercept. In the next section, we will show that this approximation provides accurate results for the average cell load. With the

approximation of (D.17) in (D.16), we have:

$$\bar{\rho}_{AP} = \chi_2 \left(\int_{t_1}^{t_2} E_1(x) e^{3.5x} \left(\frac{0.8}{t_2 - t_1} x + y_1 \right) dx + \int_{t_2}^{\infty} E_1(x) e^{-3.5x} dx \right)$$

Geller and Ng [117] provided closed-form expressions for both of the above integral types, which we employ to obtain the closed-form for the average cell load. \square

D.4 Simulation Results

D.4.1 CDF of the Load and Stable Fraction of the Network

To validate the approximation of the CDF of the cell load, we compute the stable fraction of the network, which is defined as the fraction of non-overloaded cells. Mathematically, this is the probability that the load of the typical cell is less than 1. In Fig. D.2 we compare the stable fraction of the network for a file size of $\sigma = 100$ Mb, and a user arrival rate of $\lambda_U = 100 \text{ km}^{-2}$, obtained with the approximation of the CDF derived in Theorem 4 and the one computed from Monte-Carlo simulations of the PPP. This provides dimensioning rules for the operator in terms of the minimum deployment density of BSs required to achieve a given stable fraction. For example, with a directive antenna gain of $G_0 = 20$ dB and for a load target of 0.5, the operator must deploy at least 50 BSs km^{-2} . We also observe that the closed-form CDF provides a good approximation of the numerical values, specially for a larger antenna gain ($G_0 = 20$ dB). Accordingly, the circular assumption of the cell shape is not detrimental for evaluating the performance of the network.

D.4.2 Accuracy of the EI Approximation of the Network Load

In Fig. D.3, we compare the average load of the typical cell, computed with the EI approximation (Theorem 5), the CF expression (Theorem 6), and that obtained using the mean cell approach with the network load calculated using Monte-Carlo simulations. For the Monte-Carlo simulations, we find the average

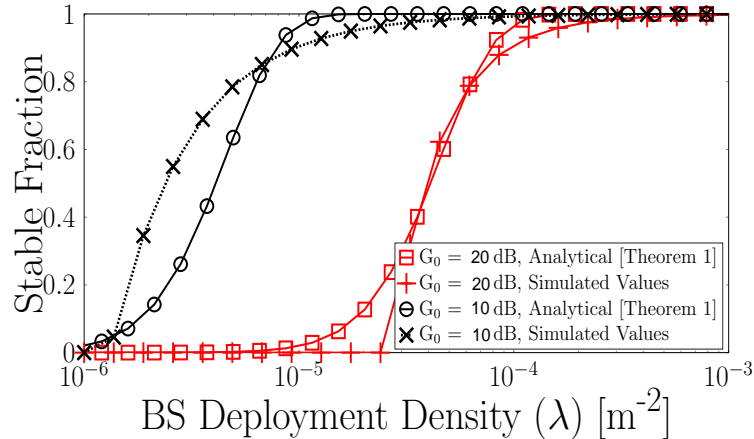


FIGURE D.2: Stable fraction of the network.

cell load in one realization of the PPP ϕ , for a given λ , λ_U , and σ and then we perform the same calculations and average over 1000 PPP realizations. As seen in the figure, the EI approximation provides a more accurate characterization of the network load than the mean cell approach. The mean cell approach always overestimates the actual load, because, the zero cell is, on average, larger than the typical cell, resulting in higher load. Therefore, from the perspective of an operator, we provide a more realistic, and hence reliable method to characterize the network load and to dimension the network. As an example, for $\sigma = 100$ Mb, and $\lambda_U = 0.01$ users per second, the EI approximation accurately estimates that the operator must deploy 10 BS less (120 as compared to 130) than that prescribed by the mean cell approach.

D.4.3 Advantages of the CF Approximation of the Network Load

As we see in Fig. D.3, the CF approximation provides the loosest approximation to the network load; however, it does not require numerical evaluation of integrals. Moreover, we see that for higher file sizes ($\sigma = 100$ Mb) and denser deployment of small cells ($\lambda \geq 1e-4$ m^{-2}), even the CF approximation provides an excellent approximation of the network load.

From a practical perspective, it provides a fast method of accurately estimating the network load without the need of running extensive simulations, which can become infeasible. Particularly, recall that BS locations are Poisson distributed. For every realization of BS locations, SNR distribution should be computed by drawing all required random variables. Moreover, a dynamic

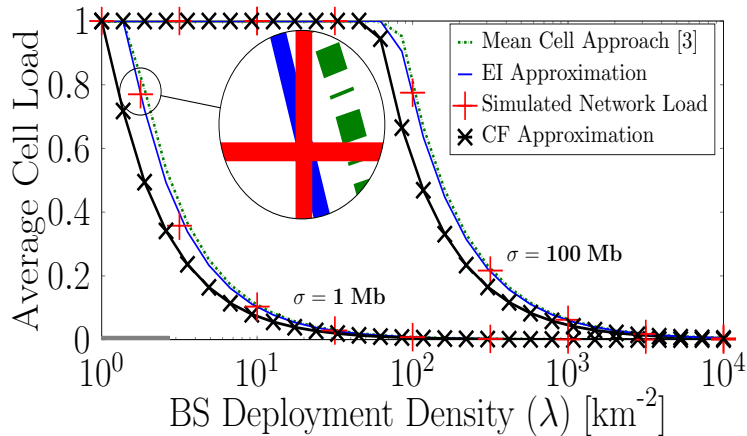


FIGURE D.3: Analytical approximation accuracy, $G_0 = 36$ dB.

traffic of users arriving in the system, downloading a file, and leaving should be simulated for a sufficient duration to reach the mixing time of the Markov process. This procedure should be repeated for every set of possible parameters if we want to characterize the network load. At last cell overloading may be undetectable as any simulation has a finite duration. For all these reasons, the analytical model presented in this analysis is necessary to provide very quick results and interesting insights to the system.

D.5 Appendix Conclusion

The realistic assessment of the mobile network performance need to take dynamic traffic into account in order to characterize the network load, which is still an open problem. Towards this end, we have derived a simple approximation for the CDF of the cell load of the typical cell in a noise-limited network, which is characterized by high SINR and low inter-cell interference. Furthermore, we have obtained a single approximation-based expression and a closed-form expression for the average load of the network by using the distribution of the area of the typical cell. Our derivations present a more realistic characterization of the cell load, as compared to the recently introduced mean cell approach, since we consider the typical cell of the network rather than the zero cell. The analysis provides a tractable and accurate characterization for the cell load that can be utilized, e.g., for evaluating the user throughput and dimensioning 5G networks. However, accurate characterization of the dynamic network load in case of an interference prone network is not straightforward. This will be addressed in a future work.

Bibliography

- [1] Cisco Visual Networking Index. “Global mobile data traffic forecast update 2014–2019 white paper, feb 2015”. In: (2015). URL: [See:http://www.cisco.com/c/en/us/solutions/collateral/service-provider/visual-networking-index-vni/white%5C_paper%5C_c11-520862.%20html](http://www.cisco.com/c/en/us/solutions/collateral/service-provider/visual-networking-index-vni/white%5C_paper%5C_c11-520862.%20html).
- [2] Jeffrey G Andrews et al. “What Will 5G Be?” In: *IEEE J. Sel. Areas Commun.* 32.6 (2014), pp. 1065–1082.
- [3] M Scott Corson et al. “Toward proximity-aware internetworking”. In: *IEEE Wireless Communications* 17.6 (2010).
- [4] Shilpa Talwar et al. “Enabling technologies and architectures for 5G wireless”. In: *Microwave Symposium (IMS), 2014 IEEE MTT-S International*. IEEE. 2014, pp. 1–4.
- [5] Erik Dahlman, Stefan Parkvall, and Johan Skold. *4G: LTE/LTE-advanced for mobile broadband*. Academic press, 2013.
- [6] Bill Krenik. “4G wireless technology: When will it happen? What does it offer?” In: *Solid-State Circuits Conference, 2008. A-SSCC’08. IEEE Asian*. IEEE. 2008, pp. 141–144.
- [7] Imtiaz Parvez et al. “A survey on low latency towards 5G: RAN, core network and caching solutions”. In: *IEEE Communications Surveys & Tutorials* (2018).
- [8] Petar Popovski. “Ultra-reliable communication in 5G wireless systems”. In: *5G for Ubiquitous Connectivity (5GU), 2014 1st International Conference on*. IEEE. 2014, pp. 146–151.
- [9] Robin R Murphy et al. “Search and rescue robotics”. In: *Springer handbook of robotics*. Springer, 2008, pp. 1151–1173.
- [10] Meryem Simsek et al. “5G-enabled tactile internet”. In: *IEEE Journal on Selected Areas in Communications* 34.3 (2016), pp. 460–473.

-
- [11] Osman NC Yilmaz et al. “Analysis of ultra-reliable and low-latency 5G communication for a factory automation use case”. In: *Communication Workshop (ICCW), 2015 IEEE International Conference on*. IEEE. 2015, pp. 1190–1195.
- [12] Wanlu Sun et al. “D2D-based V2V communications with latency and reliability constraints”. In: *2014 IEEE Globecom Workshops (GC Wkshps)*. IEEE. 2014, pp. 1414–1419.
- [13] Rapeepat Ratasuk et al. “Recent advancements in M2M communications in 4G networks and evolution towards 5G”. In: *Intelligence in Next Generation Networks (ICIN), 2015 18th International Conference on*. IEEE. 2015, pp. 52–57.
- [14] Cheng-Xiang Wang et al. “Cellular architecture and key technologies for 5G wireless communication networks”. In: *IEEE Communications Magazine* 52.2 (2014), pp. 122–130.
- [15] Panagiotis Demestichas et al. “5G on the horizon: Key challenges for the radio-access network”. In: *IEEE vehicular technology magazine* 8.3 (2013), pp. 47–53.
- [16] Xiaohu Ge et al. “5G wireless backhaul networks: challenges and research advances”. In: *IEEE Network* 28.6 (2014), pp. 6–11.
- [17] Erik G Larsson et al. “Massive MIMO for next generation wireless systems”. In: *IEEE communications magazine* 52.2 (2014), pp. 186–195.
- [18] Marco Di Renzo and Harald Haas. “On Transmit Diversity for Spatial Modulation MIMO: Impact of Spatial Constellation Diagram and Shaping Filters at the Transmitter.” In: *IEEE Trans. Vehicular Technology* 62.6 (2013), pp. 2507–2531.
- [19] Wonil Roh et al. “Millimeter-wave beamforming as an enabling technology for 5G cellular communications: Theoretical feasibility and prototype results”. In: *IEEE communications magazine* 52.2 (2014), pp. 106–113.
- [20] Xiaohu Ge et al. “5G ultra-dense cellular networks”. In: *IEEE Wireless Communications* 23.1 (2016), pp. 72–79.
- [21] Mahmoud Kamel, Walaa Hamouda, and Amr Youssef. “Ultra-dense networks: A survey”. In: *IEEE Communications Surveys & Tutorials* 18.4 (2016), pp. 2522–2545.

- [22] Marco Giordani et al. “Multi-connectivity in 5G mmWave cellular networks”. In: *Ad Hoc Networking Workshop (Med-Hoc-Net), 2016 Mediterranean*. IEEE. 2016, pp. 1–7.
- [23] Theodore S Rappaport et al. “Millimeter Wave Mobile Communications for 5G Cellular: It Will Work!” In: *IEEE Access* 1 (2013), pp. 335–349.
- [24] G. Destino and H. Wymeersch. “On the trade-off between positioning and data rate for mm-wave communication”. In: *2017 IEEE International Conference on Communications Workshops (ICC Workshops)*. May 2017, pp. 797–802. DOI: [10.1109/ICCW.2017.7962756](https://doi.org/10.1109/ICCW.2017.7962756).
- [25] Haijun Zhang et al. “Network slicing based 5G and future mobile networks: mobility, resource management, and challenges”. In: *IEEE Communications Magazine* 55.8 (2017), pp. 138–145.
- [26] E Pateromichelakis et al. “Interference Management for 5G”. In: ().
- [27] Yuya Saito et al. “Non-orthogonal multiple access (NOMA) for cellular future radio access”. In: *Vehicular Technology Conference (VTC Spring), 2013 IEEE 77th*. IEEE. 2013, pp. 1–5.
- [28] Jung Il Choi et al. “Achieving single channel, full duplex wireless communication”. In: *Proceedings of the sixteenth annual international conference on Mobile computing and networking*. ACM. 2010, pp. 1–12.
- [29] Rasha Alkhansa, Hassan Artail, and David M Gutierrez-Estevez. “LTE-WiFi carrier aggregation for future 5G systems: A feasibility study and research challenges”. In: *Procedia Computer Science* 34 (2014), pp. 133–140.
- [30] Yaniv Azar et al. “28 GHz propagation measurements for outdoor cellular communications using steerable beam antennas in New York City”. In: *Communications (ICC), 2013 IEEE International Conference on*. IEEE. 2013, pp. 5143–5147.
- [31] Ahmed Iyanda Sulyman et al. “Radio propagation path loss models for 5G cellular networks in the 28 GHz and 38 GHz millimeter-wave bands”. In: *IEEE Communications Magazine* 52.9 (2014), pp. 78–86.
- [32] Harkirat Singh et al. “A 60 GHz wireless network for enabling uncompressed video communication”. In: *IEEE Communications Magazine* 46.12 (2008).

- [33] Zhouyue Pi and Farooq Khan. “An introduction to millimeter-wave mobile broadband systems”. In: *IEEE communications magazine* 49.6 (2011).
- [34] Tuncer Baykas et al. “IEEE 802.15. 3c: the first IEEE wireless standard for data rates over 1 Gb/s”. In: *IEEE Communications Magazine* 49.7 (2011).
- [35] Eldad Perahia et al. “IEEE 802.11 ad: Defining the next generation multi-Gbps Wi-Fi”. In: *Consumer Communications and Networking Conference (CCNC), 2010 7th IEEE*. IEEE. 2010, pp. 1–5.
- [36] 3GPP TSG RAN. “TR 38.900, Study on channel model for frequency spectrum above 6 GHz”. In: *v14.1.0* (Sept. 2016).
- [37] White Paper. “5G Channel Model for bands up to 100 GHz”. In: (Dec. 2015).
- [38] Sumit Singh et al. “Blockage and directivity in 60 GHz wireless personal area networks: From cross-layer model to multihop MAC design”. In: *IEEE Journal on Selected Areas in Communications* 27.8 (2009).
- [39] A Lee Swindlehurst et al. “Millimeter-wave massive MIMO: The next wireless revolution?” In: *IEEE Communications Magazine* 52.9 (2014), pp. 56–62.
- [40] Amitava Ghosh et al. “Millimeter-Wave Enhanced Local Area Systems: A High-Data-Rate Approach for Future Wireless Networks”. In: *IEEE J. Sel. Areas Commun.* 32.6 (2014), pp. 1152–1163.
- [41] Yingzhe Li et al. “On the initial access design in millimeter wave cellular networks”. In: *IEEE GLOBECOM Wkshps.* 2016, pp. 1–6.
- [42] M. Giordani, M. Mezzavilla, and M. Zorzi. “Initial Access in 5G mmWave Cellular Networks”. In: *IEEE Communications Magazine* 54.11 (Nov. 2016), pp. 40–47.
- [43] H2020-ICT-671650 mmMAGIC. “D3.1: Initial concepts on 5G architecture and integration”. In: *Available Online at <https://5g-mmmagic.eu/>* (Mar. 2016.).
- [44] Ari Kangas and Torbjorn Wigren. “Angle of arrival localization in LTE using MIMO pre-coder index feedback”. In: *IEEE Commun. Lett.* 17.8 (2013), pp. 1584–1587.

- [45] Gourab Ghatak, Antonio De Domenico, and Marceau Coupechoux. “Coverage Analysis and Load Balancing in HetNets with mmWave Multi-RAT Small Cells”. In: *IEEE Trans. Wireless Commun.* PP.99 (2018), pp. 1–1. ISSN: 1536-1276. DOI: [10.1109/TWC.2018.2807426](https://doi.org/10.1109/TWC.2018.2807426).
- [46] Seizo Onoe. “Evolution of 5G mobile technology toward 2020 and beyond”. In: *IEEE ISSCC*. 2016, pp. 23–28.
- [47] Z. Pi and F. Khan. “An introduction to millimeter-wave mobile broadband systems”. In: *IEEE Commun. Mag.* 49.6 (June 2011), pp. 101–107. ISSN: 0163-6804. DOI: [10.1109/MCOM.2011.5783993](https://doi.org/10.1109/MCOM.2011.5783993).
- [48] Boyd Bangerter et al. “Networks and devices for the 5G era”. In: *IEEE Communications Magazine* 52.2 (2014), pp. 90–96.
- [49] Dantong Liu et al. “User association in 5G networks: A survey and an outlook”. In: *IEEE Communications Surveys & Tutorials* 18.2 (2016), pp. 1018–1044.
- [50] Jeffrey G Andrews et al. “An overview of load balancing in HetNets: Old myths and open problems”. In: *arXiv preprint arXiv:1307.7779* (2013).
- [51] Toni Janevski. “5G mobile phone concept”. In: *Consumer Communications and Networking Conference, 2009. CCNC 2009. 6th IEEE*. IEEE. 2009, pp. 1–2.
- [52] Sung Nok Chiu et al. *Stochastic geometry and its applications*. John Wiley & Sons, 2013.
- [53] H. ElSawy, E. Hossain, and M. Haenggi. “Stochastic geometry for modeling, analysis, and design of multi-tier and cognitive cellular wireless networks: A survey”. In: *IEEE Communications Surveys & Tutorials* 15.3 (2013), pp. 996–1019.
- [54] François Baccelli, Bartłomiej Błaszczyszyn, et al. “Stochastic geometry and wireless networks: Volume II Applications”. In: *Foundations and Trends® in Networking* 4.1–2 (2010), pp. 1–312.
- [55] Martin Haenggi et al. “Stochastic geometry and random graphs for the analysis and design of wireless networks”. In: *IEEE Journal on Selected Areas in Communications* 27.7 (2009).
- [56] Jeffrey G Andrews, Abhishek K Gupta, and Harpreet S Dhillon. “A primer on cellular network analysis using stochastic geometry”. In: *arXiv preprint arXiv:1604.03183* (2016).

- [57] Bartłomiej Błaszczyszyn, Miodrag Jovanovicy, and Mohamed Kadhem Karray. “How user throughput depends on the traffic demand in large cellular networks”. In: *IEEE WiOpt*. 2014, pp. 611–619.
- [58] R. Koirala et al. “Localization bound based beamforming optimization for multicarrier mmWave MIMO”. In: *2017 14th Workshop on Positioning, Navigation and Communications (WPNC)*. Oct. 2017, pp. 1–6. DOI: [10.1109/WPNC.2017.8250057](https://doi.org/10.1109/WPNC.2017.8250057).
- [59] Kaishun Wu et al. “CSI-based indoor localization”. In: *IEEE Transactions on Parallel and Distributed Systems* 24.7 (2013), pp. 1300–1309.
- [60] Manikanta Kotaru et al. “Spotfi: Decimeter level localization using wifi”. In: *ACM SIGCOMM Computer Communication Review*. Vol. 45. 4. ACM. 2015, pp. 269–282.
- [61] A. Shahmansoori et al. “5G Position and Orientation Estimation through Millimeter Wave MIMO”. In: *2015 IEEE Globecom Workshops (GC Wkshps)*. Dec. 2015.
- [62] A. Shahmansoori et al. “Position and Orientation Estimation Through Millimeter-Wave MIMO in 5G Systems”. In: *IEEE Transactions on Wireless Communications* 17.3 (Mar. 2018), pp. 1822–1835.
- [63] Harry L Van Trees. *Detection, estimation, and modulation theory*. John Wiley & Sons, 2004.
- [64] EO Christopher, Harpreet S Dhillon, and R Michael Buehrer. “A Statistical Characterization of Localization Performance in Wireless Networks”. In: *IEEE Transactions on Wireless Communications* 17.9 (2018), pp. 5841–5856.
- [65] D. López-Pérez et al. “Towards 1 Gbps/UE in cellular systems: understanding ultra-Dense small cell deployments”. In: *IEEE Communications Surveys & Tutorials* 17.4 (2015), pp. 2078–2101.
- [66] Kenta Okino et al. “Pico Cell Range Expansion with Interference Mitigation toward LTE-Advanced Heterogeneous Networks”. In: *IEEE ICC Workshops*. 2011, pp. 1–5.
- [67] Miguel Eguizabal and Angela Hernandez. “Interference management and cell range expansion analysis for LTE picocell deployments”. In: *IEEE PIMRC*. 2013, pp. 1592–1597.

-
- [68] Mohd Shabbir Ali, Pierre Coucheney, and Marceau Coupechoux. “Load balancing in heterogeneous networks based on distributed learning in potential games”. In: *IEEE WiOpt*. 2015, pp. 371–378.
- [69] T. Bai and R. W. Heath. “Coverage and rate analysis for millimeter-wave cellular networks”. In: *IEEE Transactions on Wireless Communications*, 14.2 (2015), pp. 1100–1114.
- [70] Sarabjot Singh and Jeffrey G Andrews. “Joint Resource Partitioning and Offloading in Heterogeneous Cellular Networks”. In: *IEEE Trans. Wireless Commun.* 13.2 (2014), pp. 888–901.
- [71] Marco Di Renzo. “Stochastic Geometry Modeling and Analysis of Multi-Tier Millimeter Wave Cellular Networks”. In: *IEEE Trans. Wireless Commun.* 14.9 (2015), pp. 5038–5057.
- [72] Guangzhong Yao et al. “Coverage and rate analysis for non-uniform millimeter-wave heterogeneous cellular network”. In: *Wireless Communications & Signal Processing (WCSP), 2016 8th International Conference on*. IEEE. 2016, pp. 1–6.
- [73] Hisham Elshaer et al. “Downlink and Uplink Cell Association with Traditional Macrocells and Millimeter Wave Small Cells”. In: *arXiv preprint arXiv:1601.05281* (2016).
- [74] Thomas Bonald and Alexandre Proutière. “Wireless Downlink Data Channels: User Performance and Cell Dimensioning”. In: *ACM MobiCom*. 2003, pp. 339–352.
- [75] Sarabjot Singh, Harpreet S Dhillon, and Jeffrey G Andrews. “Offloading in heterogeneous networks: Modeling, analysis, and design insights”. In: *IEEE Trans. Wireless Commun.* 12.5 (2013), pp. 2484–2497.
- [76] Tianyang Bai, Rahul Vaze, and Robert W Heath. “Analysis of Blockage Effects on Urban Cellular Networks”. In: *IEEE Trans. Wireless Commun.* 13.9 (2014), pp. 5070–5083.
- [77] 3GPP. “TR 36.873, Study on 3D channel model for LTE”. In: *Release 12* (Mar. 2010).
- [78] 3GPP TSG RAN. “TR 36.814, E-UTRA; Further advancements for E-UTRA physical layer aspects”. In: *v9.0.0* (Mar. 2010).

- [79] X. Zhang and M. Haenggi. “A stochastic geometry analysis of inter-cell interference coordination and intra-cell diversity”. In: *IEEE Transactions on Wireless Communications*, 13.12 (2014), pp. 6655–6669.
- [80] Hossein Shokri-Ghadikolaie et al. “Millimeter Wave Cellular Networks: A MAC Layer Perspective”. In: *IEEE Trans. Commun.* 63.10 (2015), pp. 3437–3458.
- [81] Gourab Ghatak, Antonio De Domenico, and Marceau Coupechoux. “Performance Analysis of Two-tier Networks with Closed Access Small-cells”. In: *IEEE WiOpt.* 2016, pp. 1–8.
- [82] Alberto Leon-Garcia. *Probability, statistics, and random processes for electrical engineering*. Pearson/Prentice Hall, 3rd ed., 2008.
- [83] S. M. Hasan, M. A. Hayat, and M. F. Hossain. “On the downlink SINR and outage probability of stochastic geometry based LTE cellular networks with multi-class services”. In: *18th ICCIT*. Dec. 2015, pp. 65–69. DOI: [10.1109/ICCITech.2015.7488044](https://doi.org/10.1109/ICCITech.2015.7488044).
- [84] Xenofon Foukas et al. “Network Slicing in 5G: Survey and Challenges”. In: *IEEE Commun. Mag.* 55 (2017).
- [85] Jeffrey G Andrews, Francois Baccelli, and Radha Krishna Ganti. “A tractable approach to coverage and rate in cellular networks”. In: *IEEE Trans. Commun.* 59.11 (2011), pp. 3122–3134.
- [86] Young Jin Chun, Mazen O Hasna, and Ali Ghayeb. “Modeling heterogeneous cellular networks interference using poisson cluster processes”. In: *IEEE J. Sel. Areas Commun* 33.10 (2015), pp. 2182–2195.
- [87] C Gloaguen et al. “Analysis of shortest paths and subscriber line lengths in telecommunication access networks”. In: *Networks and Spatial Economics* 10.1 (2010), pp. 15–47.
- [88] F. Morlot. “A population model based on a Poisson line tessellation”. In: *IEEE WiOpt.* May 2012, pp. 337–342.
- [89] Chang-Sik Choi and François Baccelli. “An Analytical Framework for Coverage in Cellular Networks Leveraging Vehicles”. In: *arXiv preprint arXiv:1711.09453* (2017).
- [90] G. Ghatak, A. De Domenico, and M. Coupechoux. “Modeling and Analysis of HetNets with mm-Wave Multi-RAT Small Cells Deployed along Roads”. In: *IEEE GLOBECOM 2017* (Dec. 2017), pp. 1–7.

- [91] A. Tassi et al. “Modeling and Design of Millimeter-Wave Networks for Highway Vehicular Communication”. In: *IEEE Trans. Veh. Technol.* PP.99 (2017), pp. 1–1. ISSN: 0018-9545. DOI: [10.1109/TVT.2017.2734684](https://doi.org/10.1109/TVT.2017.2734684).
- [92] “Mobilizing 5G NR Millimeter Wave: Network Coverage Simulation Studies for Global Cities”. In: (Oct. 2017). URL: <https://www.qualcomm.com/media/documents/files/white-paper-5g-nr-millimeter-wave-network-coverage-simulation.pdf>.
- [93] Hossein Shokri-Ghadikolaei, Lazaros Gkatzikis, and Carlo Fischione. “Beamsearching and transmission scheduling in millimeter wave communications”. In: *IEEE ICC, 2015*, pp. 1292–1297.
- [94] 3GPP. “TR 38.913, Study on Scenarios and Requirements for Next Generation Access Technologies”. In: *v14.3.0* (2016).
- [95] Jeffrey G Andrews et al. “Modeling and analyzing millimeter wave cellular systems”. In: *IEEE Trans. Commun.* 65.1 (2017), pp. 403–430.
- [96] EU-Commission et al. “Regulation (EEC) No 4064/89 Merger Procedure”. In: *Case No COMP/JV* (2000).
- [97] Nil Garcia et al. “Location-aided mm-wave channel estimation for vehicular communication”. In: *2016 IEEE 17th International Workshop on Signal Processing Advances in Wireless Communications (SPAWC)*. 2016, pp. 1–5.
- [98] Seongah Jeong et al. “Beamforming design for joint localization and data transmission in distributed antenna system”. In: *IEEE Transactions on Vehicular Technology* 64.1 (2015), pp. 62–76.
- [99] Filip Lemic et al. “Localization as a Feature of mmWave Communication”. In: *2016 IEEE International Wireless Communications and Mobile Computing Conference (IWCMC)*, 2016, pp. 1033–1038.
- [100] G. Ghatak, A. De Domenico, and M. Coupechoux. “Modeling and Analysis of HetNets with mm-Wave Multi-RAT Small Cells Deployed along Roads”. In: *IEEE GLOBECOM 2017*. Dec. 2017, pp. 1–7. DOI: [10.1109/GLOCOM.2017.8254855](https://doi.org/10.1109/GLOCOM.2017.8254855).

- [101] S. Singh, R. Mudumbai, and U. Madhow. “Interference Analysis for Highly Directional 60-GHz Mesh Networks: The Case for Rethinking Medium Access Control”. In: *IEEE/ACM Transactions on Networking* 19.5 (Oct. 2011), pp. 1513–1527. ISSN: 1063-6692. DOI: [10.1109/TNET.2011.2122343](https://doi.org/10.1109/TNET.2011.2122343).
- [102] J. G. Andrews et al. “Modeling and Analyzing Millimeter Wave Cellular Systems”. In: *IEEE Transactions on Communications* 65.1 (Jan. 2017), pp. 403–430. ISSN: 0090-6778. DOI: [10.1109/TCOMM.2016.2618794](https://doi.org/10.1109/TCOMM.2016.2618794).
- [103] A. Dammann et al. “Optimizing waveforms for positioning in 5G”. In: *2016 IEEE 17th International Workshop on Signal Processing Advances in Wireless Communications (SPAWC)*. July 2016, pp. 1–5. DOI: [10.1109/SPAWC.2016.7536783](https://doi.org/10.1109/SPAWC.2016.7536783).
- [104] Kaishun Wu et al. “Fila: Fine-grained indoor localization”. In: *IEEE INFOCOM Proceedings*. 2012, pp. 2210–2218.
- [105] Vera Ignatevna Pagurova. *Tables of the exponential integral*. Vol. 8. Pergamon Press, 1961.
- [106] S. Rangan, T. S. Rappaport, and E. Erkip. “Millimeter-Wave Cellular Wireless Networks: Potentials and Challenges”. In: *Proceedings of the IEEE* 102.3 (Mar. 2014), pp. 366–385.
- [107] S. Kutty and D. Sen. “Beamforming for Millimeter Wave Communications: An Inclusive Survey”. In: *IEEE Communications Surveys Tutorials* 18.2 (Secondquarter 2016), pp. 949–973.
- [108] F. Lemic et al. “Localization as a feature of mmWave communication”. In: *2016 International Wireless Communications and Mobile Computing Conference (IWCMC)*. Sept. 2016, pp. 1033–1038.
- [109] Nil Garcia, Henk Wymeersch, and Dirk T. M. Slock. “Optimal Robust Precoders for Tracking the AoD and AoA of a mm-Wave Path”. In: (2017). URL: <http://arxiv.org/abs/1703.10978>.
- [110] Andrew M Hunter, Jeffrey G Andrews, and Steven Weber. “Transmission capacity of ad hoc networks with spatial diversity”. In: *IEEE Trans. Wireless Commun.* 7.12 (2008), pp. 5058–5071.
- [111] Junse Lee and François Baccelli. “On the effect of shadowing correlation on wireless network performance”. In: *IEEE INFOCOM 2018-IEEE Conference on Computer Communications*. IEEE. 2018, pp. 1601–1609.

-
- [112] Abishek Sankararaman, Jeong-woo Cho, and François Baccelli. “Performance-oriented association in large cellular networks with technology diversity”. In: *arXiv preprint arXiv:1603.06928* (2016).
- [113] H. Elshaer et al. “Downlink and Uplink Cell Association With Traditional Macrocells and Millimeter Wave Small Cells”. In: *IEEE Trans. Wireless Commun.* 15.9 (Sept. 2016), pp. 6244–6258. ISSN: 1536-1276. DOI: [10.1109/TWC.2016.2582152](https://doi.org/10.1109/TWC.2016.2582152).
- [114] Masaharu Tanemura. “Statistical distributions of Poisson Voronoi cells in two and three dimensions”. In: *FORMA-TOKYO-* 18.4 (2003).
- [115] DA Barry, J-Y Parlange, and L Li. “Approximation for the exponential integral (Theis well function)”. In: *Journal of Hydrology* 227.1 (2000), pp. 287–291.
- [116] P Pecina. “On the function inverse to the exponential integral function”. In: *BAICz* 37 (1986), pp. 8–12.
- [117] Murray Geller and Edward W Ng. “A table of integrals of the exponential integral”. In: *J. Res. Natl. Bur. Stand.* 71 (1969), pp. 1–20.